A Measurement of the Λ_b^0 Lifetime at the DØ Experiment

Marcus Philip Lewin *MPhys(Hons)*
Lancaster University

A thesis submitted for the degree of Doctor of Philosophy

July, 2007

A Measurement of the Λ_b^0 Lifetime at the DØ Experiment

Marcus Philip Lewin *MPhys(Hons)*

Lancaster University

A thesis submitted for the degree of Doctor of Philosophy

July, 2007

Abstract

This thesis describes a measurement of the lifetime of the Λ_b^0 baryon, performed using data from proton-antiproton collisions at a centre of mass energy of 1.96 TeV. The decay $\Lambda_b^0 \to \Lambda_c^+ \mu^- \bar{\nu}_\mu X$ was reconstructed in approximately 1.3 fb^{-1} of data recorded by the DØ detector in 2002-2006 during Run II of the Fermilab Tevatron collider. A signal of 4437 $\pm$ 329 $\Lambda_c^+ \mu^-$ pairs was obtained, and the Λ_b^0 lifetime was measured using a binned χ^2 fit, which gives a value $\tau(\Lambda_b^0) = 1.290^{+0.119}_{-0.110}(\text{stat})^{+0.085}_{-0.091}(\text{syst})$ ps. This result is consistent with the world average and is one of the most precise measurements of this quantity.

Acknowledgements

This work was made possible by the efforts of a large number of people at DØ, who are too numerous to mention here, but deserve many thanks anyway. The following people in particular deserve special mentions for their contributions.

First and foremost I would like to thank my supervisor, Guennadi Borissov, who has been an excellent supervisor throughout. I feel lucky to have had a supervisor who was so dedicated in this role, while also being a very active physicist in the collaboration. His major contributions to the DØ tracking and the analysis framework used throughout the B physics group were also essential in making this analysis possible.

I would also like to thank Iain Bertram who helped me with many things involving Monte Carlo, and been a useful source of advice over the years. Alberto Sanchez-Hernandez and Ralf Bernhard also deserve thanks for assistance in producing the Monte Carlo for the analysis. Thanks to Wendy Taylor, Andy White and the rest of the editorial board for their assistance in getting the results ready for showing to the outside world. Thanks for this also go to Rick van Kooten, who has provided many useful comments and suggestions throughout, the B physics conveners and the members of the group.

I would like to thank the group at Lancaster for providing me with this opportunity, and PPARC for providing the funding.

Finally, many thanks go to my family and friends for their support throughout.

Contents

List of Figures

List of Tables

Chapter 1

Introduction

This thesis presents work I performed within the DØ collaboration to make a measurement of the lifetime of the Λ_b^0 baryon. The b-hadrons such as the Λ_b^0 are currently the subject of much research in both the theoretical and experimental particle physics communities. Measurements of the production and decays of b-hadrons can improve understanding of the electroweak and strong interactions described by the Standard Model of particle physics, as well as providing opportunities to search for physics beyond the Standard Model. The bottom quark is the heaviest to form bound states. A heavy quark within a bound state gives a simplified system for studying the strong interaction, since the heavy quark may be treated as a static source of colour. Measurements of b-hadron lifetimes provide information on parameters of the electroweak interaction and test predictions of the complicated effects due to QCD which occur within quark bound states.

The DØ collaboration is based at Fermilab in Batavia, Illinois, USA. Fermilab is the home of the Tevatron, currently the highest energy particle accelerator in the world. Protons are collided with antiprotons inside the DØ and CDF detectors, at a centre of mass energy of approximately 2 TeV. A vast range of processes may occur when the particles collide, hence the two collaborations are active in searches for exotic particles predicted by theories such as supersymmetry, as well

as measurements to increase the precision of the Standard Model properties. In this environment a large number of b-hadrons are produced, allowing the Tevatron to be an important instrument in the study of their physics. The production of all b-flavoured hadrons allows the DØ and CDF collaborations to investigate the full spectrum of b-hadron properties, including the properties of B_s^0 mesons and b-baryons which currently cannot be observed at any other experiments.

The following sections in this chapter provide a brief outline of the current state of research in elementary particle physics. The theoretical framework known as the Standard Model is briefly described, before the current experimental situation is reviewed.

In Chapter 2 the theory relevant to the measurement made in this thesis is described, while the techniques used to perform similar measurements at previous experiments are outlined in Chapter 3. Chapter 4 gives a description of the experimental apparatus used, and Chapter 5 describes the methods used by the collaboration to reconstruct physics objects from the signals recorded by the detector. Chapters 6 and 7 deal with the work I did to perform the measurement, the former dealing with the techniques used to select the decays of interest, the latter describing the method of measuring the Λ_b^0 lifetime. The final chapter summarises the results and examines their implications.

1.1 The Standard Model

The Standard Model (SM) is the mathematical framework in which the known elementary particles and their interactions are described. Three of the four fundamental forces - those of electromagnetism, the weak force and the strong force - are described within the SM as a collection of gauge theories. Although the SM has been very successful at predicting many measurable quantities, it is far from a complete theory. It contains several free parameters, such as the fermion masses,

that cannot be predicted, and an important member of the SM, the Higgs Boson, so far has not been observed. Another failure of the SM is its inability to include gravity and thereby describe all of the four forces. In the remainder of this section a brief introduction to the elements of the SM is given.

1.1.1 The Elementary Particles

The SM includes the 12 fundamental fermions from which matter is constructed, along with 4 force mediating gauge bosons and a Higgs boson. The basic fermions are the quarks and leptons, all of which have spin $\frac{1}{2}$. For each of these there is a corresponding antiparticle with quantum numbers of opposite sign. The quarks and leptons are each arranged into three generations, as shown in Table 1.1. The leptons consist of the electron, muon and tau and their associated neutrinos. The electron, muon and tau have mass and participate in both the electromagnetic and weak interactions. The neutrinos were assumed to be massless, until recent evidence suggested that they carry small masses [1]. The six quarks participate in the electromagnetic, weak and strong interactions. The quark generations each contain an 'up-type' quark with charge $\frac{2}{3}e$ and a 'down-type' quark with charge $-\frac{1}{3}e$. Due to the properties of the strong interaction, quarks are not observed as free particles, but are instead always found within bound states known as *hadrons*, apart from the top quark which decays before forming bound states. This makes determination of their properties, such as masses, more problematic. However, estimates reveal that the quarks have widely varying masses, as indicated in Table 1.2.

The gauge bosons include the massless, electrically neutral photon and gluon, which are the mediators of the electromagnetic force and the strong force respectively, and the massive $W^{\pm}$ and Z^0 bosons which mediate the weak force. All of these have spin 1. The Higgs boson is predicted to exist in order for the $W^{\pm}$ and

Generation	1	2	3	charge(e)
quarks	u(up)	c(charm)	t(top)	$\frac{2}{3}$
	d(down)	s(strange)	b(bottom)	$-\frac{1}{3}$
leptons	e(electron)	μ(muon)	τ(tau)	-1
	ν_e(e neutrino)	ν_μ(μ neutrino)	ν_τ(τ neutrino)	0

Table 1.1: The generations of fermions in the Standard Model.

Quark	Mass (MeV/c^2)
u	1.5-3.0
d	3-7
c	1250 ± 90
s	95 ± 25
t	$(172.5 \pm 2.7) \times 10^3$
b	$(4.20 \pm 0.07) \times 10^3$

Table 1.2: Estimates of the quark masses, as listed in [2]. The top quark mass is determined from direct observation, whereas the remaining masses are estimated in QCD using the $\overline{\text{MS}}$ renormalisation scheme.

Z^0 bosons and the fermions to acquire mass, however it has not yet been observed.

1.1.2 The Fundamental Forces

The interactions in the SM are described in quantum field theory by a collection of gauge theories. All gauge theories are derived from the idea that a Lagrangian representing a quantum field must be invariant under *local* gauge transformations, i.e. transformations that are space-time dependant. The electromagnetic interaction was the first to be formulated as a gauge theory, the formulation of the weak interactions and the strong interaction as gauge theories later followed.

The Electromagnetic Interaction

The electromagnetic interaction acts between particles carrying electric charge, which interact via the exchange of photons. The photon is massless and hence the interaction acts over a long range. In quantum field theory it is described by the theory of Quantum Electrodynamics(QED). In the case of QED, the local gauge

transformations are local phase transformations belonging to the group of unitary 1×1 matrices known as $U(1)$. Requiring invariance of the Dirac Lagrangian under such transformations means that an extra field must be added to the Lagrangian. This *gauge field* is seen to represent the photon, since the Lagrangian of QED, which can be derived from Maxwell's equations, is reproduced by the gauge theory. In order to preserve the local gauge invariance, the photon is required to be massless. The properties of QED allow precise predictions of observable properties to be made using perturbation theory, and the theory is seen to agree well with experimental data.

The Strong Interaction

The strong interaction is mediated by the gluon, and acts between particles carrying *colour*. It has been described by the theory of Quantum Chromodynamics (QCD). This theory is analogous to QED, in that the Lagrangian is required to be invariant under local gauge transformations, which gives rise to the mediators of the force. The difference between QED and QCD is that whereas in QED there is a single type of electric charge, in QCD the quarks may carry one of three different colours. Hence the corresponding gauge transformation is represented by a 3×3 matrix of the group known as $SU(3)$. Unlike the members of the $U(1)$ group, the members of $SU(3)$ do not commute with each other, and this fact manifests itself in the observable differences between QED and QCD. The gluons themselves carry colour and hence can interact with each other, unlike the photons in QED. This gives rise to a coupling of the strong interaction that increases with separation, and this is the reason that free quarks are not observed. Quarks in hadrons experience a very weak coupling due to their small separation, so they behave as if they are essentially free, this property being known as *asymptotic freedom*. When quarks are produced in high energy collisions, their separation increases until their energy is sufficiently high to produce more quark-antiquark

pairs. These then form together into hadrons, creating the jets of particles that are observed. The additional complications arising in QCD make theoretical predictions and experimental measurements much more difficult than those in QED.

The Weak Interactions and Electroweak Unification

Both quarks and leptons participate in the weak interaction, which is mediated by the $W^{\pm}$ and Z^0 bosons. Unlike the electromagnetic and strong interactions, the charged weak interaction, mediated by the $W^{\pm}$ boson, can change the *flavour* of particles. In the lepton sector, the $W^{\pm}$ couples between an electron, muon or tau and its corresponding neutrino, with no mixing between the generations. For the quarks, the couplings are predominantly between quarks of the same generation, although some cross-generational couplings do occur.

The weak interaction differs from the electromagnetic and strong interactions in that it acts over a very short range, since the $W^{\pm}$ and Z^0 bosons have large masses of $80.403 \pm 0.029\ \mathrm{GeV}/c^2$ and $91.1876 \pm 0.0021\ \mathrm{GeV}/c^2$ respectively [2]. As mentioned previously, a gauge field with a mass will generally break the symmetry of local gauge invariance. The electroweak theory, in which the electromagnetic interaction is unified with the weak interaction, uses the mechanism of spontaneous symmetry breaking to achieve a theory with massive gauge bosons and local gauge invariance. In this case the ground state of the Lagrangian is degenerate and not invariant under gauge transformations. With a degenerate ground state, selection of a particular ground state as the vacuum state leads to massless bosons in the theory, which are unphysical. By working in a particular gauge the massless bosons can be made to vanish and be replaced by a massive field representing the Higgs Boson. In this process the gauge bosons acquire a mass.

The weak interaction also differs in that it violates the symmetry of parity, which changes the sign of spatial coordinates. In the electromagnetic and strong interactions parity is conserved, however in the weak interactions it is maximally

violated, since neutrinos are only observed with left-handed helicity, and anti-neutrinos with right-handed helicity. It was thought that the combination of charge conjugation, which changes particles to antiparticles, and parity may be a symmetry of the weak interactions, however a small violation of this CP symmetry was observed in the decays of the neutral kaons [3], and this has also been observed in the neutral B meson system. CP violation may occur in the decays or in the particle-antiparticle oscillations, known as mixing, that occur in the neutral kaon and B meson systems. CP violation is expected to be responsible for the excess of matter over antimatter in the universe, however its origin in the Standard Model is not understood and is the subject of current research.

The electroweak theory unifies the $U(1)$ theory of electromagnetism with the weak interaction by the group $SU(2) \times U(1)_Y$. The $U(1)_Y$ group represents the interactions which conserve a quantity known as hypercharge (Y), whereas the $SU(2)$ group conserves weak isospin. The $SU(2)$ group gives rise to three gauge bosons, one positively charged, one negative and one neutral, whereas the $U(1)_Y$ gives rise to one neutral gauge boson, similarly to the photon in QED. A superposition of these two neutral gauge bosons gives rise to the observed Z^0 boson and the photon.

1.2 Particle Physics Experiments

As mentioned previously, the Tevatron at Fermilab is currently the highest energy particle accelerator in the world, colliding protons and antiprotons at approximately 2 TeV centre of mass energy. Since the proton is a composite particle, the collisions result in interactions between the constituent partons, which have varying energies. Hence the energy of the interaction is not known, and the resulting products may carry significant momentum in the direction of one of the beams. An enormous variety of processes may occur in a collision, allowing many types

of particles to be produced.

In addition to hadron colliders such as the Tevatron, there also exist electron-positron colliders. The advantage of these is that the energy of the collision is determined by the energy of the beams, and can be controlled. This allows large samples of specific particles of interest to be produced and studied. However, the main drawback of electron-positron machines is the synchrotron radiation that is emitted when the particles are accelerated, limiting the attainable energy in circular synchrotron machines.

The push to increase collision energies allows heavier particles to be produced, and smaller distance scales to be probed. Since some processes are very rare, the potential for new discoveries at such machines also depends on the rate of collisions produced per unit area, which is known as the *luminosity*. The amount of data used for an analysis is typically quoted in terms of the *integrated* luminosity obtained over the period of data taking.

1.2.1 Recent, Current and Future Experiments

In addition to the Tevatron, two electron-positron colliders which focus on the study of B mesons are currently running. These are the KEK accelerator and the associated Belle detector in Japan, and the PEPII B-factory at Stanford Linear Accelerator Center in California, which is used by the BaBar collaboration. Both of these experiments began running in 1999. The accelerators both use asymmetric beams with energies of approximately 9 GeV and 3 GeV to produce a moving $\Upsilon(4s)$, a $b\bar{b}$ resonant state that subsequently decays predominantly to a $B^0\bar{B}^0$ meson pair. These allow the particle-antiparticle mixing and CP violation in this system to be studied.

Prior to the current experiments, the most important facility for b-hadron studies was the Large Electron-Positron (LEP) collider at CERN, in Geneva, Switzer-

land, which ran from 1989 until 2000. Four experiments, known as ALEPH, DELPHI, OPAL and L3, were located around the LEP accelerator ring. The collider operated in two separate data-taking periods. In the first, the electron and positron beams were accelerated to around 45 GeV in order to produce Z bosons and study their properties. b-hadrons were produced in some of the hadronic decays of the Z^0 bosons, and a variety of measurements were performed. In the second running period the accelerator was upgraded to provide beams of $80 - 104$ GeV, in order to allow production of W^+W^- pairs.

Since the finish of collisions at the LEP accelerator, CERN has been building a new accelerator in its place. The Large Hadron Collider (LHC) is expected to commence collisions in 2008, and at design energy will collide two 7 TeV proton beams, taking over from the Tevatron as the world's most powerful accelerator. The luminosity will be approximately two orders of magnitude above that of the Tevatron, so data will be accumulated very rapidly in comparison. There are two general purpose detectors, ATLAS and CMS, that are broadly similar to DØ and CDF, and a dedicated b-physics experiment, known as LHCb. The latter will have powerful particle identification capabilities, which should allow high precision b-hadron studies to be performed.

Chapter 2

Theoretical Background

The lifetimes of the Λ_b^0 baryon and the other b-flavoured hadrons have been the subject of both theoretical and experimental studies for over a decade. This chapter first describes the mechanisms involved in b-hadron decays, and the effects which lead to differences between the lifetimes of these particles. A systematic method of accounting for these effects, known as the heavy quark expansion, has been developed and is used to provide predictions of the lifetimes. A brief description of this method and its recent predictions is given. The chapter concludes with a review of the production of b-hadrons at the Fermilab Tevatron.

2.1 b-hadron Decays and Lifetimes

The decays of b-hadrons proceed via the flavour changing weak interaction. Therefore the most important factors influencing their decay rates are the couplings of the W boson. *Spectator effects* involving the light quarks in a b-hadron give small contributions which lead to lifetime differences of a few per cent. Providing theoretical predictions for these differences is challenging, since there are many effects to be accounted for, including the non-perturbative nature of QCD for the low energy interactions within bound states. The heavy quark expansion systemati-

cally accounts for all such effects, providing a framework for prediction of b-hadron lifetimes.

2.1.1 The CKM Matrix

The charged weak interaction changes the flavour of quarks, with the W boson coupling an up-type quark to a down-type quark. This coupling does not only occur within a quark generation, but within the doublets $\begin{pmatrix} u \\ d' \end{pmatrix}, \begin{pmatrix} c \\ s' \end{pmatrix}, \begin{pmatrix} t \\ b' \end{pmatrix}$, where the d', s' and b' are linear combinations of the d, s and b quarks[1]. These combinations are given by the Cabibbo-Kobayashi-Maskawa (CKM) quark mixing matrix,

$$\begin{pmatrix} d' \\ s' \\ b' \end{pmatrix} = V_{CKM} \begin{pmatrix} d \\ s \\ b \end{pmatrix} = \begin{pmatrix} V_{ud} & V_{us} & V_{ub} \\ V_{cd} & V_{cs} & V_{cb} \\ V_{td} & V_{ts} & V_{tb} \end{pmatrix} \begin{pmatrix} d \\ s \\ b \end{pmatrix}. \tag{2.1}$$

The elements of the CKM matrix are complex quantities. The matrix represents a rotation in flavour space, and so is by definition required to be a unitary matrix ($V_{CKM}V_{CKM}^{\dagger} = 1$). The unitarity requirement leads to nine constraints which reduce the possible 18 real parameters of a 3×3 complex matrix to nine for the CKM matrix. Of these, five relative phases may be absorbed into the quark states, leaving a total of four independent parameters in the matrix. These may be expressed as three real mixing angles, which describe rotations in flavour space, and a complex phase. The existence of this phase allows CP violation in the Standard Model [4]. The small number of parameters allows the matrix to be expressed using a number of parametrisation schemes. A popular parametrisation is the Wolfenstein parametrisation [5], which expands the elements in powers of

[1]It is convention that the lower quarks in the generations are rotated.

$\lambda = |V_{us}|$:

$$V_{CKM} \approx \begin{pmatrix} 1 - \frac{1}{2}\lambda^2 & \lambda & \lambda^3 A(\rho - i\eta) \\ -\lambda & 1 - \frac{1}{2}\lambda^2 & \lambda^2 A \\ \lambda^3 A(1 - \rho - i\eta) & -\lambda^2 A & 1 \end{pmatrix}. \tag{2.2}$$

The parameters λ, ρ and A represent the real mixing angles, while $i\eta$ introduces the complex phase. The increasing powers of λ in the off-diagonal elements show a suppression of these transitions. This suppression is mirrored in the averages of the measured magnitudes [2], that are shown below[2]:

$$\begin{pmatrix} 0.97377 \pm 0.00027 & 0.2257 \pm 0.0021 & (4.31 \pm 0.30) \times 10^{-3} \\ 0.230 \pm 0.011 & 0.957 \pm 0.095 & (41.6 \pm 0.6) \times 10^{-3} \\ (7.4 \pm 0.8) \times 10^{-3} & (40.6 \pm 2.7) \times 10^{-3} & > 0.78 \end{pmatrix}. \tag{2.3}$$

Since the diagonal elements have magnitudes close to unity, and the off diagonal elements are smaller, coupling occurs predominantly within the quark generations. Transitions between the first and third generations experience the highest suppression, followed by those between the second and third generations.

2.1.2 Decays of b-hadrons

The quark mixing specified by the CKM matrix allows the b quark to couple to the c and u quarks as well as to the top quark. Due to the larger mass, decays to a top quark are not kinematically allowed, and hence the b quark must decay by either of the routes represented by V_{cb} and V_{ub}. The small magnitudes of these couplings lead to low decay rates and hence relatively long lifetimes for the b-hadrons. Due

[2]The measurement of $|V_{tb}|$ represents a 95% confidence limit.

to V_{cb} being approximately an order of magnitude larger than V_{ub}, the probability for a b quark to couple to a u quark is of the order of 1%. Hence the decays are heavily dominated by processes such as that shown in Figure 2.1. In this example the light quarks are assumed to be simply spectators to the decay. Modelling the decay using this spectator approximation gives an identical prediction for all b-hadron lifetimes, from which the measured values deviate by up to roughly 15%[3]. The deviations from the spectator model are much larger for the charm hadrons, which have lifetimes varying by factors up to around 5 [2]. The spectator effects of W scattering, weak annihilation and Pauli Interference were first studied to explain the lifetime differences between the charmed mesons [6, 7]. Figure 2.2 shows the processes of decay by W scattering for a Λ_b^0 baryon and a B^0 meson, and the decay of B^+ by weak annihilation. These decay paths are strongly suppressed due to the separation of quarks within a hadron, although they also receive an enhancement due to the phase space for such $2 \to 2$ body processes being larger than that of the spectator process by a factor of $16\pi^2$. Another effect of spectator quarks is Pauli Interference, which affects non-leptonic decays. An example of a decay that will experience this effect is shown in Figure 2.3. The interference between identical quarks in the final state may either inhibit or enhance the rate of these decays. The different spectator effects for the various hadrons contribute to the differences between their lifetimes. The study of these effects in charm hadrons correctly predicted the qualitative hierarchy of their lifetimes, but could not provide accurate quantitative predictions in either the charm or b-hadron systems. The modern approach described below allows all such effects to be systematically included to give precise predictions for the b-hadron lifetimes.

[3]The B_c^+ is excluded from these discussions. It has a much shorter lifetime since either the b or the c quark may decay.

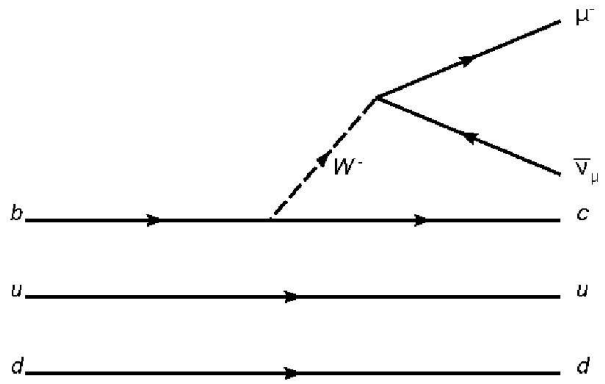

Figure 2.1: Feynman diagram for the semileptonic decay of a Λ_b^0 baryon via the spectator process.

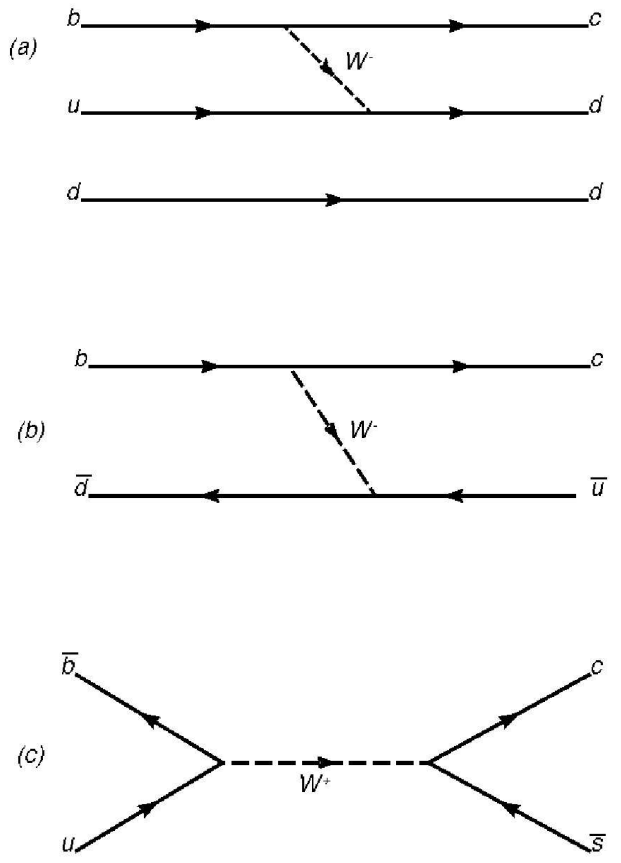

Figure 2.2: Examples of b-hadron decays in which a light quark from the initial state is involved in the interaction. (a) Decay of Λ_b^0 by W scattering. (b) Decay of $\bar{B}^0$ by W scattering. (c) Decay of B^+ by weak annihilation.

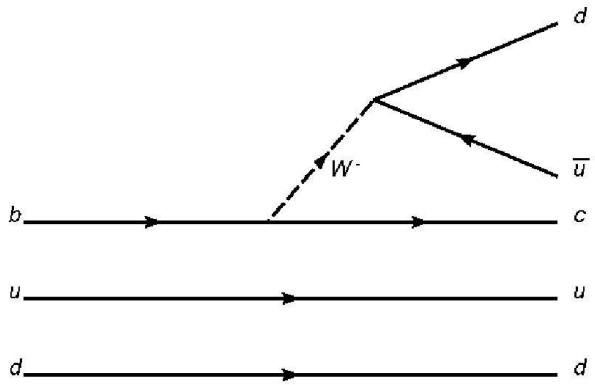

Figure 2.3: Feynman diagram for a decay of the Λ_b^0 baryon which experiences Pauli Interference due to two identical d quarks in the final state.

2.1.3 The Heavy Quark Expansion

Due to the running coupling constant and quark confinement, many QCD interactions cannot be treated perturbatively. At small distances, which correspond to high energy interactions, the coupling constant is small and accurate predictions can be obtained using perturbation theory. At large distances the coupling constant is large and the physics is non-perturbative. The energy scale $\Lambda_{QCD} \approx 200$ MeV separates regions of large and small coupling constant. In the non-perturbative region the physics is complicated and simplifications must be made to enable computation of quantities. A bound state containing a heavy quark is an example of a system in which simplifications can be made, due to the large mass of the heavy quark. A heavy quark interacts with lighter constituents through the exchange of soft gluons, which have energy of the order of Λ_{QCD}. Heavy quarks are defined as those with mass $m_Q >> \Lambda_{QCD}$, hence the charm, bottom and top quarks are classified as heavy quarks[4]. In hadrons containing a heavy quark, the momentum fluctuations of that quark are small, and they vanish as m_Q tends to infinity. Integrating out these fluctuations leads to the heavy-quark effective theory (HQET), a theory which matches QCD for low mo-

[4]The top quark is of no relevance to these discussions, however, since it decays without forming bound states.

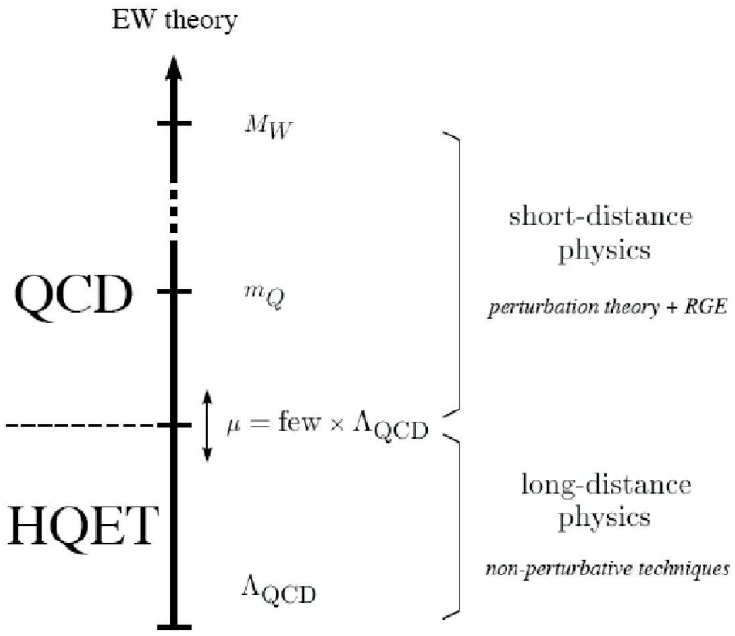

Figure 2.4: Illustration of the energy regime in which the heavy-quark effective theory (HQET) provides a simplified description of QCD in hadrons containing a heavy quark.

mentum processes, as illustrated in Figure 2.4. HQET provides important inputs to the predictions of b-hadron lifetimes, which are performed using an expansion in inverse powers of the b quark mass, m_b. When computing decay rates, the large mass of a heavy quark enables the decay rate to be expressed as an infinite sum of operators, with coefficients of increasing powers of $1/m_Q$, as described in [8]. Using this method, the decay rate for a heavy flavour hadron H_Q to an inclusive final state f is given by [9]

$$\Gamma_{H_Q \to f} = |CKM|^2 \sum_n c_n^{(f)} \left(\frac{\Lambda_{QCD}}{m_Q} \right)^n \langle H_Q | O_n | H_Q \rangle. \tag{2.4}$$

$|CKM|^2$ is a combination of the relevant CKM matrix elements for the decay. The coefficients $c_n^{(f)}$ can be calculated using perturbative methods and are known as the Operator Product Expansion. The expectation values $\langle H_Q | O_n | H_Q \rangle$ contain

all of the non-perturbative physics that is due to interactions with the cloud of light quarks and gluons, and are usually estimated using the HQET. The leading term in the expansion is the decay rate of a free quark,

$$\Gamma_0 = \frac{G_F^2 m_Q^5}{192\pi^3}|V_{cb} + V_{ub}|^2, \tag{2.5}$$

where G_F is the Fermi constant. The differences between the lifetimes are given by the terms that contain at least two powers of $1/m_Q$. In fact, the $1/m_Q^2$ term provides only a difference between the meson and baryon lifetimes. The differences between meson lifetimes arise in the $1/m_Q^3$ and higher terms. The effects of W scattering, weak annihilation and Pauli Interference arise as contributions to these terms. As $m_Q \to \infty$ the expansion becomes increasingly dominated by the leading term, Γ_0, and the lifetime differences between Q flavoured hadrons decrease to zero. Hence the lifetime differences between charm hadrons are correctly predicted to be larger than those for the b-hadrons. However, the predictions for charm hadrons are only semi-quantitative and are seen to approximately agree with the measurements, whereas for b-hadrons the predictions have a level of precision similar to the experimental measurements. The theoretical uncertainties on the expectation values $\langle H_Q|O_n|H_Q\rangle$ allow the uncertainties on the lifetime predictions to be estimated. Predictions of the ratios of lifetimes are preferred, since some theoretical uncertainties cancel. The theoretical predictions and experimental averages at the end of 2005 for the ratios of b-hadron lifetimes are shown in Table 2.1. The value of $\tau(\Lambda_b^0)/\tau(B^0)$ currently appears to be in reasonable agreement with the predictions, although previously this was not the case. Earlier predictions were for a value of $\tau(\Lambda_b^0)/\tau(B^0)$ greater than 0.9 [10], which differed from the experimental average by around 2 standard errors. A recent extension to include the calculation of $1/m_b^4$ terms [11], combined with new experimental

Lifetime ratio	Measured Value	Predicted Range
$\tau(B^+)/\tau(B^0)$	1.076 ± 0.008	$1.04 - 1.08$
$\bar{\tau}(B_s^0)/\tau(B^0)$	0.914 ± 0.030	$0.99 - 1.01$
$\tau(\Lambda_b^0)/\tau(B^0)$	0.844 ± 0.043	$0.86 - 0.95$
$\tau(b-\text{baryon})/\tau(B^0)$	0.813 ± 0.030	$0.86 - 0.95$

Table 2.1: Experimental averages [9] and theoretical predictions [11, 12, 13] of the b-hadron lifetime ratios at the end of 2005.

results has substantially reduced the discrepancy, and the most significant disagreement with the theory is currently the average B_s^0 lifetime. However, the errors for $\tau(\Lambda_b^0)/\tau(B^0)$ are still relatively large and more measurements are required to give a rigorous test of the prediction.

2.2 b-hadron Production at the Tevatron

At the Tevatron collider at Fermilab, bunches of protons and antiprotons are collided at a centre of mass energy of 1.96 TeV, as described in Chapter 4. At this energy the cross section for production of b quarks is high compared to other interesting processes, as shown in Figure 2.5 [14], although it is only about 1.5 parts per 1000 of the total interaction cross section, which includes all elastic and inelastic scattering processes. The cross section for charm production is approximately a factor of 10 larger than the value for b quark production [15], and these events cause a significant physics background to many of the processes reconstructed in the study of b-hadrons.

The dominant processes of b production are those of flavour creation, which produce a back-to-back $b\bar{b}$ pair. This occurs by gluon-gluon fusion or quark-antiquark annihilation, for which the leading order Feynman diagrams are shown in Figure 2.6. b quarks may also be produced individually by flavour excitation, in which a virtual b quark present in the initial proton or antiproton is scattered into the final state by a gluon or light quark, as is illustrated in the final diagram

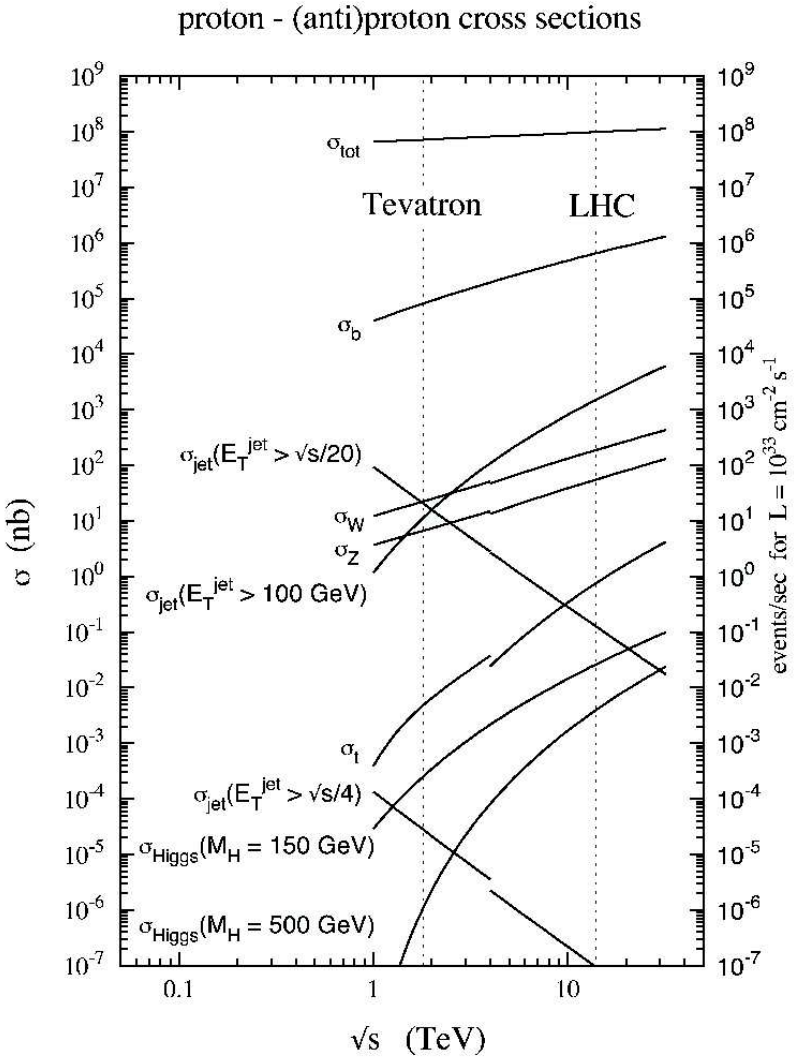

Figure 2.5: Next to leading order QCD predictions of various production cross sections versus centre-of-mass energy in $p\bar{p}$ and pp interactions. The curves for lower energy ranges are for $p\bar{p}$ interactions,while those for higher energies are for pp interactions such as at the LHC.

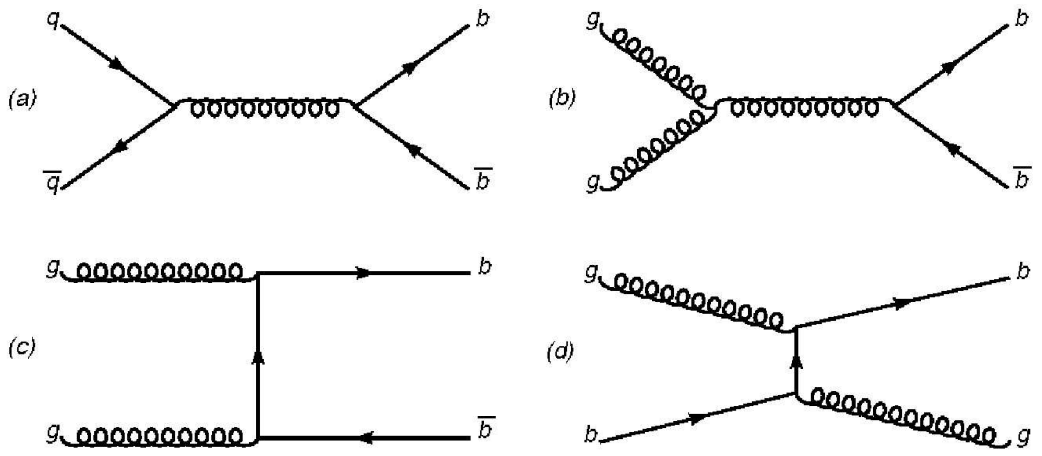

Figure 2.6: Production mechanisms for b quarks in $p\bar{p}$ collisions. (a) shows flavour creation by quark-antiquark annihilation, (b) and (c) are flavour creation by gluon-gluon fusion, and (d) is flavour excitation of a b quark in the proton or antiproton.

b-hadron	Fraction(%)
B^+, B^0	40.2 ± 0.9
B_s	10.4 ± 0.9
b-baryons	9.1 ± 1.5

Table 2.2: Production fractions for different b-hadron species, obtained from measurements at LEP and the Tevatron.

of Figure 2.6. $b\bar{b}$ pairs may also be produced in the showering and hadronisation processes that follow the hard scatter. The expected contributions from all of these processes [16] give agreement with the b production cross sections measured by DØ [17] and CDF [18, 19].

The hadronisation process is not well understood, but measurements of the fractions of B^+, B^0, B_s^0 and b-baryons have been performed at both LEPI and at the Tevatron, and have been averaged to give the fractions shown in Table 2.2 [20]. The b-baryon fraction is close to 10%, and is expected to be dominated by Λ_b^0 production. At the energy of the Tevatron the b-hadrons are given a boost that results in them typically travelling several millimetres before decaying, giving a favourable environment for the study of their lifetimes.

Chapter 3

Experimental Background

Several measurements of each b-hadron lifetime have previously been performed. The B factories of BaBar and Belle have produced large samples of B^0 and B^+ mesons, and have provided some of the most precise lifetime measurements for these particles. However, the majority of measurements of these and the other b-hadron lifetimes were performed by the collaborations using the LEP accelerator, since this collider allowed the study of all b-hadrons. Currently the Tevatron is the only place where this is possible. This chapter discusses measurements of b-hadron lifetimes at high energy colliders such as LEP and the Tevatron. The main classes of measurements are first described, before the previous measurements of the Λ_b^0 lifetime are outlined. The chapter concludes by examining the potential for a semileptonic Λ_b^0 lifetime measurement at DØ.

3.1 b-hadron Lifetime Measurements

Lifetime measurements relating to specific species of b-hadrons may be placed into a number of categories. There are distinct differences between analyses that use semileptonic decays for reconstruction and those that use hadronic channels. Analyses may also differ in terms of the quantities measured. In the majority of

cases the absolute lifetime of one or more specific b-hadrons is measured. If the measurement of two lifetimes in the same analysis is possible, then a measurement of the lifetime ratio may also be provided. A much rarer type of measurement extracts the lifetime ratio of two species directly, without measuring their individual lifetimes. The features of the various types of measurement are described in more detail below.

3.1.1 Reconstruction of b-hadrons

When measuring the lifetime of a particular b-hadron species, the hadron of interest may be identified by reconstruction of either semileptonic or hadronic decays. The practical details of performing a measurement are different for the two types of decays. In semileptonic decays the momentum of the b-hadron cannot be fully reconstructed, since a neutrino from the decay goes undetected. However, knowledge of the momentum is required in order to convert a measured flight distance into a proper decay time. Hence the semileptonic measurements rely on simulation to provide a statistical distribution for the fraction of the momentum that is taken by the visible constituents, which is then included in the lifetime fitting procedure. The b-hadron is identified by associating a reconstructed charm hadron with a lepton, so measurements using these decays suffer from significant backgrounds due to a charm hadron produced at the primary vertex being wrongly associated with a lepton produced from the decay of another particle. These factors add significant measurement uncertainties, but these are often counteracted by a large advantage due to the favourable statistics obtained, and the simplicity of triggering on these events. The semileptonic branching fractions of b-hadrons are around 10% per lepton species, approximately two orders of magnitude larger than those of the hadronic decays that may be used. Each b-hadron has a large number of hadronic decays, although the difficulty in identifying the decay prod-

ucts will give large combinatorial backgrounds in most cases. However, decays involving a J/ψ meson have been used extensively. The J/ψ decays mainly to hadrons, but decays to $\mu^+\mu^-$ and e^+e^- both occur with fractions of around 6%. Since muons and electrons are relatively simple to identify, these decays are easily triggered on and suffer less from combinatorial background than other channels. Since the b-hadron is fully reconstructed the uncertainties due to estimation of momentum and sample composition that exist in semileptonic decays are not a problem for these analyses, and despite the reduced statistics the precision of lifetime measurements using these decays is generally comparable to that of the semileptonic measurements.

3.1.2 Lifetime and Lifetime Ratio Measurements

The majority of lifetime related analyses have directly measured the absolute lifetime of a specific b-hadron species. Some analyses have exploited similar decay topologies to measure two lifetimes using the same selection, such as measuring the B^0 lifetime using $B^0 \to J/\psi K^0_S$ and measuring the Λ^0_b lifetime using $\Lambda^0_b \to J/\psi\Lambda^0$ [21, 22]. Measuring the precisely known B^0 lifetime provides a check of the calibration of the method used to measure the less well known Λ^0_b lifetime, and also allows a measurement of the lifetime ratio $\tau(\Lambda^0_b)/\tau(B^0)$ to be performed. By measuring both lifetimes in the same analysis the computation of systematic uncertainties in the ratio measurement is simplified, and some systematic uncertainties may cancel. Direct measurements of the lifetime ratio, without measuring the individual lifetimes, are also possible. The analysis procedures employed for the two types of measurements are described briefly below.

Absolute Lifetime Measurements

In these measurements a sample containing the reconstructed decays of the

hadron of interest is selected, and the distribution of proper decay times is generally fitted using an unbinned maximum likelihood method. The sample of decays will also contain background, so in order to fit the signal lifetime the background lifetime distribution must be fitted simultaneously. A background lifetime function depending on several parameters is included, and a second background-only sample is used in addition to provide constraints on the parameters. The distribution of proper decay length and results of such a lifetime fit for a sample of $\Lambda_b^0 \to J/\psi\Lambda^0$ decays obtained by DØ are shown in Figure 3.1 [21]. This fitting procedure relies heavily on the lifetime distribution in the background-only sample matching that of the background in the signal sample. To provide an unbiased measurement, it is also necessary to ensure that the lifetime distribution of the signal sample is not biased by any of the selection criteria. Therefore any quantities correlated with the lifetime may not be used as discriminating variables.

Direct Lifetime Ratio Measurement

A direct measurement of the ratio of B^+ and B^0 lifetimes has been performed by DØ [23], giving one of the most precise results for this quantity. Events were selected by reconstructing the semileptonic decays $B^+ \to \mu^+\nu_\mu\bar{D}^0X$ and $B^0 \to \mu^+\nu_\mu D^{*-}X$, where D^{*-} decays to $\bar{D}^0\pi^-$. The only difference between the topologies of these decays is the existence of a pion from the D^{*-} decay. The existence or otherwise of this pion allowed the events to be classified into two samples, one dominated by B^0 decays and the other by B^+ decays. These samples were then divided into bins according to the measured proper decay length of the partially reconstructed B meson. In each bin the number of signal events from each sample was calculated and the ratio was computed. The change in this ratio across the bins was due to the lifetime difference between the two mesons, which was determined by a χ^2 fit to the bins, as shown in Figure 3.2. Since this analysis did not measure absolute lifetimes, any bias in the lifetime distributions

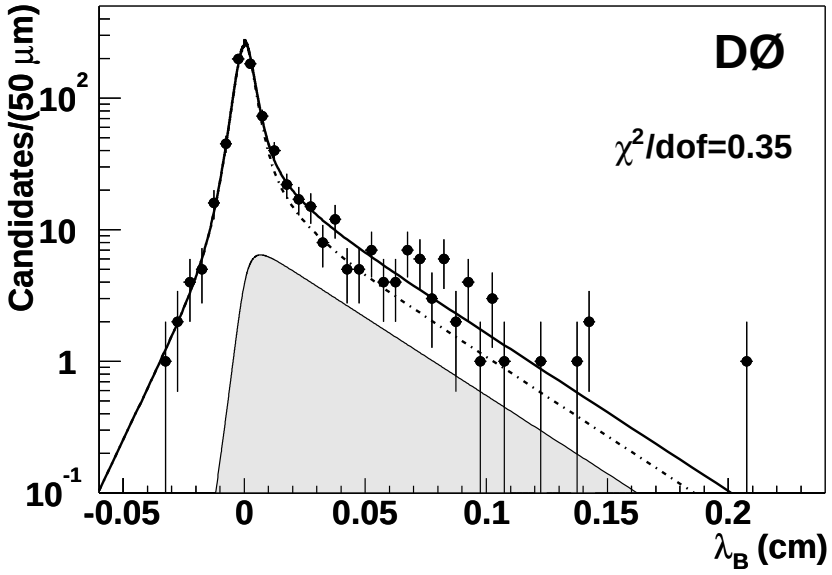

Figure 3.1: Proper decay length distribution for a sample of $\Lambda_b^0 \to J/\psi\Lambda^0$ candidates obtained by DØ, showing the results of the lifetime fit. The fit to the data is indicated by the solid line. The fit contains contributions from signal and background components, which are indicated by the shaded area and the dashed line respectively.

did not affect the result, provided that the ratio of reconstruction efficiencies for the samples was independent of the lifetime. This allowed additional lifetime biasing cuts to be used in this case, giving a substantial reduction of the background. Measurements of this type could be performed for many other pairs of similar decays. However, in most cases the lifetime characteristics of the two sets of decay products will be different and the use of lifetime biasing selections will give a lifetime dependant ratio of efficiencies.

3.2 Λ_b^0 Lifetime Measurements

Prior to the current run of the Fermilab Tevatron, measurements of the Λ_b^0 lifetime were performed in the first run of the LEP accelerator [24, 25, 26] and by CDF in Run I of the Tevatron [27]. During the initial run of LEP, analyses by

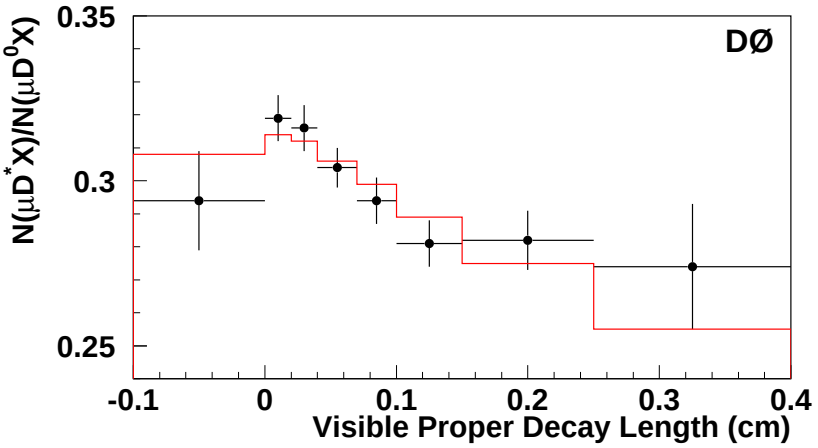

Figure 3.2: The ratio of $B^0 \to \mu^+ \nu D^{*-} X$ to $B^+ \to \mu^+ \nu \bar{D}^0 X$ decays reconstructed by DØ as a function of the proper decay length of the partially reconstructed B meson. The solid line shows the result of the lifetime ratio fit.

the ALEPH, DELPHI and OPAL collaborations reconstructed Λ_b^0 baryons in the hadronic decays of the Z^0 bosons produced in the e^+e^- collisions. These three detectors each recorded around 4 million hadronic decays, from which samples of around 200 semileptonic Λ_b^0 decays were reconstructed. With the luminosity provided by LEP, only semileptonic decays would allow sufficient samples of Λ_b^0 decays to be obtained. In the same period a similar measurement was carried out by the CDF collaboration in proton-antiproton collisions at 1.8 TeV centre of mass energy. From an integrated luminosity of around 110 pb^{-1} a sample similar in size to those of the LEP experiments was obtained. It is only with the higher luminosity of Run II of the Tevatron that the fully reconstructible decays with lower branching fractions have been utilised, with CDF and DØ both providing measurements using the decay $\Lambda_b^0 \to J/\psi \Lambda^0$ [21, 22]. These analyses also measured the lifetime of B^0 using $B^0 \to J/\psi K_S^0$ and could therefore also provide a measurement of the lifetime ratio $\tau(\Lambda_b^0)/\tau(B^0)$. These measurements were competitive with the previous semileptonic measurements after only a small part of

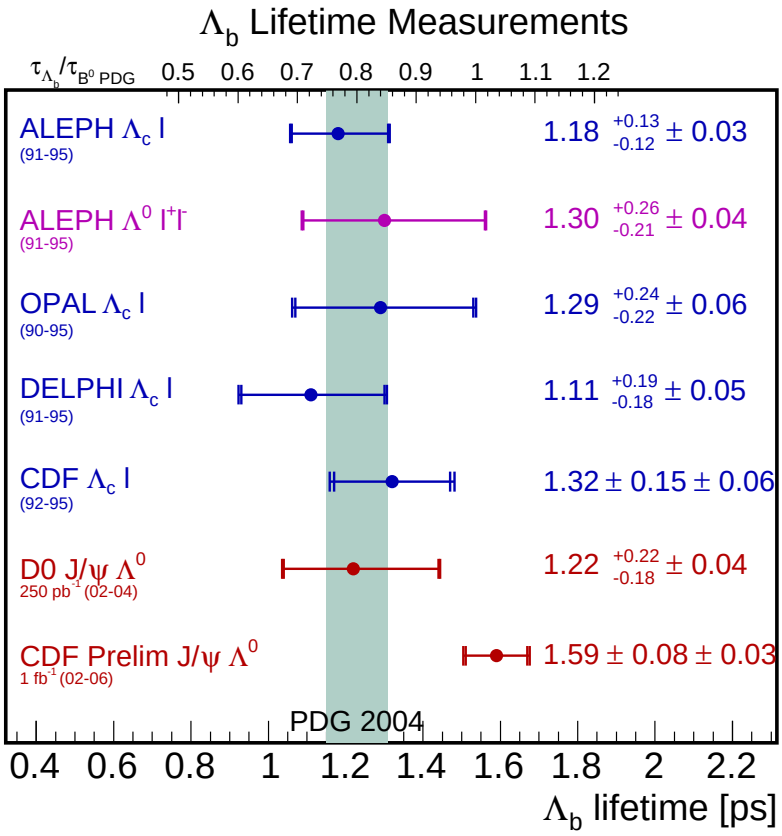

Figure 3.3: Published and preliminary measurements of the Λ_b^0 lifetime in mid 2006. The shaded area indicates the experimental uncertainty of the 2004 world average value.

Run II. No semileptonic measurement has previously been performed in Run II, although they may produce competitive results. The results of the published and preliminary measurements as of mid 2006 are shown in Figure 3.3. The latest update of the CDF $\Lambda_b^0 \to J/\psi\Lambda^0$ analysis has yielded a result with higher precision than the previous results, but which lies around 3 standard errors above the previous world average.

All of the previous measurements fitted the Λ_b^0 lifetime using conventional maximum likelihood methods. It may be possible to apply the technique of direct lifetime ratio measurement to the $\Lambda_b^0 \to J/\psi\Lambda^0$ and $B^0 \to J/\psi K_S^0$ pair of decays used in the CDF and DØ measurements, and this possibility may also exist for

semileptonic decays. The decay chains $\Lambda_b^0 \to \Lambda_c^+ \mu^- \bar{\nu}_\mu (\Lambda_c^+ \to K_S^0 p)$ and $B^0 \to D^+ \mu^- \bar{\nu}_\mu (D^+ \to K_S^0 \pi^+)$ have similar final states, which will be reconstructed by the same selection. However, in both of these cases the use of lifetime biasing cuts to enhance the selection may not be possible due to differences in lifetimes of the decay products.

3.2.1 Potential For Semileptonic Measurements at DØ

The increased luminosity during Run II of the Fermilab Tevatron should allow significantly larger semileptonic samples to be obtained than in previous measurements. As described in detail in Chapter 4, the DØ detector has a set of muon detectors with large coverage, providing a clean signal and efficient triggering. Hence it should be possible to reconstruct a large sample of $\Lambda_b^0 \to \Lambda_c^+ \mu^- \bar{\nu}_\mu X$ decays. However, all of the detectors that provided previous semileptonic measurements were equipped with systems for particle identification over a wide momentum range. DØ has capabilities for particle identification using energy loss information from the inner tracking detectors, however this is only useful for tracks with momentum below 1 GeV/c [28]. This will mean higher backgrounds in the reconstruction of Λ_c^+ baryons, and make some channels unfeasible. The Λ_c^+ has a large number of possible decay channels, and a few of these were used in the previous measurements. The most popular channel was $\Lambda_c^+ \to pK^-\pi^+$, since this has the highest branching fraction. The branching fractions for this and other selected decays are shown in Table 3.1. Figure 3.4 shows the mass plot for the $pK^-\pi^+$ channel from CDF in Run I, which contains 197 ± 25 signal events. The combinatorial background is likely to be significantly higher without particle identification, and hence a search for this channel at DØ may not produce useful results. The ALEPH, DELPHI and OPAL measurements also used other channels in addition. The ALEPH analysis used the most different decays, combining

Decay	Branching fraction
$pK^-\pi^+$	$(5.0 \pm 1.3)\%$
$p\bar{K}^0$	$(2.3 \pm 0.6)\%$
$p\bar{K}^0\pi^+\pi^-$	$(2.6 \pm 0.7)\%$
$\Lambda\pi^+$	$(1.01 \pm 0.28)\%$
$\Lambda\pi^+\pi^+\pi^-$	$(2.6 \pm 0.7)\%$
$\Lambda l^+\nu_l$	$(2.0 \pm 0.6)\%$

Table 3.1: Branching fractions for the decays of Λ_c^+ reconstructed in previous semileptonic Λ_b^0 lifetime measurements.

four different hadronic channels and the semileptonic decay $\Lambda_c^+ \to \Lambda^0 l^+ \bar{\nu}_l$. The DELPHI and OPAL measurements also used the semileptonic decays in addition to hadronic decays. As shown in Table 3.1, the semileptonic decays have relatively high branching fractions, but due to the Λ_c^+ not being fully reconstructed they will suffer from additional backgrounds and uncertainties. The signals obtained by ALEPH for each hadronic channel separately are shown in Figure 3.5. The only additional hadronic channel used in any measurement was the decay to $p\bar{K}^0\pi^+\pi^-$ used by DELPHI, which gave a relatively low signal yield. Without particle identification, the most recognisable decay products are the K_S^0 and Λ^0, since these undergo the decays $K_S^0 \to \pi^+\pi^-$ and $\Lambda^0 \to p\pi^+$ at large distances from the interaction. Thus these particles may be identified by finding this decay vertex and computing the invariant mass. Therefore the decays $\Lambda_c^+ \to pK_S^0$ and $\Lambda_c^+ \to \Lambda^0\pi^+$ will be the hadronic channels with the lowest backgrounds at DØ.

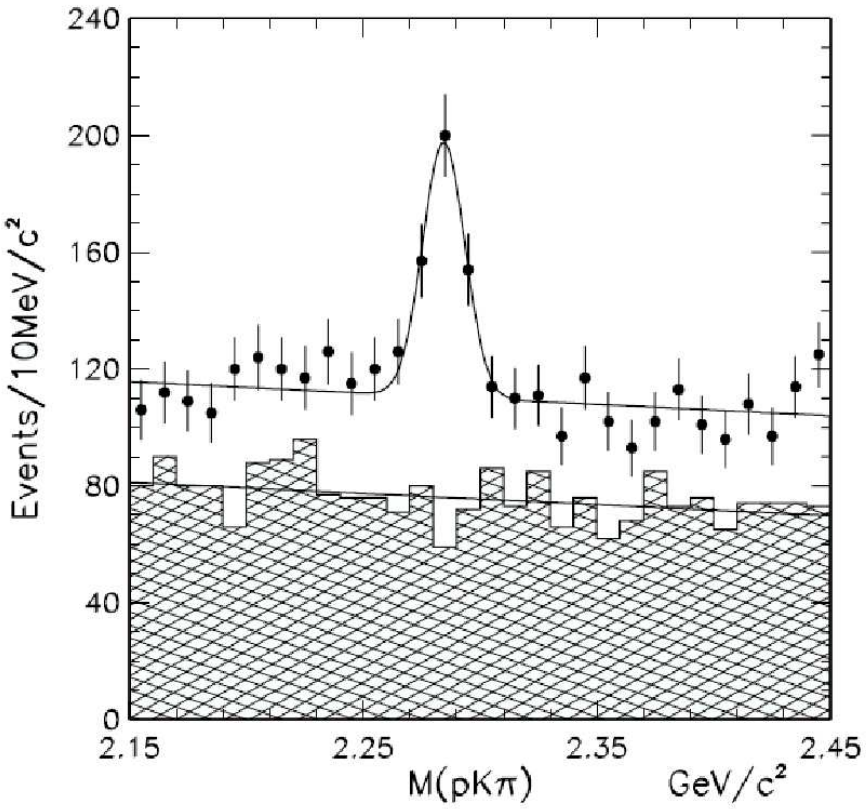

Figure 3.4: The $pK^-\pi^+$ invariant mass spectrum for $\Lambda_b^0 \to \Lambda_c^+ l^- \bar{\nu}_l X(\Lambda_c^+ \to pK^-\pi^+)$ candidates, obtained in 110 pb^{-1} of $p\bar{p}$ interactions by CDF in Run I. The shaded area shows the level of wrong-sign $\Lambda_c^+ l^+$ events.

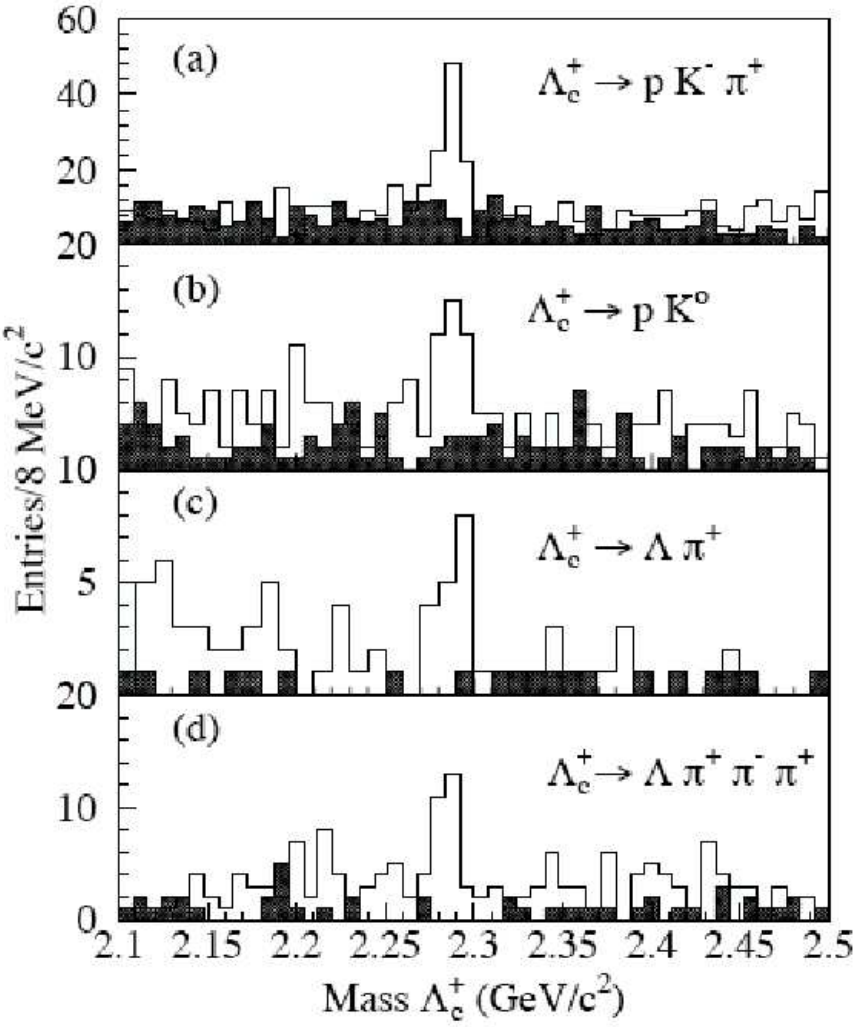

Figure 3.5: Invariant mass of Λ_c^+ candidates in $\Lambda_c^+ l^-$ combinations reconstructed by ALEPH, shown separately for four different hadronic Λ_c^+ decay channels. The shaded areas show the wrong-sign $\Lambda_c^+ l^+$ combinations.

Chapter 4

The Tevatron and the DØ Detector

The DØ detector is one of two multi-purpose physics detectors located on the Tevatron accelerator at Fermilab, Batavia, IL, USA. The experiments are currently operating in a second data taking period. The first period, known as Run I, took place between 1992 and 1995. During Run I the centre of mass energy was 1.8 TeV, similar to the Run II energy of 1.96 TeV, however the luminosity of the collider was significantly lower, so the data sample obtained was small. Also the capabilities of the DØ detector were limited compared to the current detector. DØ provided some significant results in Run I, such as an observation of the top quark [29], but the limited tracking did not allow the study of b-hadrons and during this run the only measurements in this area were made at CDF. The Tevatron and the DØ detector received substantial upgrades after the finish of Run I, and Run II began in 2002 with a much improved detector, and increased luminosities provided by the Tevatron. The large data samples provided by the higher rate of collisions in the detector, and the improved tracking and muon systems on the detector, have allowed DØ to begin producing competitive b-physics measurements in Run II. In the following sections the Tevatron is briefly introduced, and the

features of the DØ detector are described.

4.1 The Tevatron in Run II

The Tevatron is currently the highest energy particle accelerator operating. Beams of protons and antiprotons are accelerated to an energy of almost 1 TeV by a chain of accelerators, before being collided in the centre of the CDF and DØ detectors. A schematic diagram of the accelerator chain is shown in Figure 4.1. This section describes the main features and processes of the accelerator chain.

4.1.1 Proton and Antiproton Production

The initial stage in the production of protons and antiprotons is a Cockcroft-Walton pre-accelerator. Here hydrogen atoms are ionised to make H^- ions, which are then accelerated through the initial stages of the accelerator complex. The Cockcroft-Walton machine accelerates the ions to an energy of about 750 keV, before feeding them into a linear accelerator where they are accelerated to 400 MeV. After this stage the electrons are removed from the ions to leave protons, by passing the beam of ions through a carbon foil. The protons then enter a synchrotron accelerator, known as the Booster, and are accelerated to around 8 GeV before entering the Main Injector, a synchrotron with 3km circumference. The Main Injector sends protons into the Tevatron at an energy of 150 GeV, or to the Antiproton Source, at 120 GeV. To produce antiprotons, the protons at 120 GeV are collided with a nickel target. These collisions produce antiprotons as well as other particles, so the antiprotons are separated using bending magnets as a charge-mass spectrometer. Antiprotons are stored in the accumulator ring until they can be sent to the Main Injector, from which they are injected into the Tevatron.

4.1.2 The Tevatron

The Tevatron provides the final acceleration stage before collisions. It is a superconducting synchrotron with a circumference of six kilometres, and is currently the highest energy accelerator in the world. The protons and antiprotons are accelerated from 150 GeV to their collision energy of 980 GeV. Once collision energy is reached, the beams are focused for collisions in the two detectors. The protons and antiprotons circle in bunches, with bunch crossings occurring every 396 ns in the centre of the detectors. The beams continue to circle and collisions are recorded for several hours, during a period known as a *store*. Collisions and loss of particles from the beams reduce the luminosity, and several hours after collisions are initiated the beams are dumped and a new store is started. The main parameters of the Tevatron for Run I and the current Run IIa are shown in Table 4.1 [30].

4.1.3 Accelerator Performance

Figure 4.2 shows the weekly integrated luminosity throughout Run II, and Figure 4.3 shows the peak luminosity for each store. At the start of Run II the luminosity was far below the design luminosity, but the luminosity gradually increased and reached the design luminosity toward the end of Run IIa, which finished in March 2006. At this stage the integrated luminosity delivered by the accelerator had reached approximately 1.6 fb^{-1}, of which almost 85% was recorded by DØ [31]. This period constitutes the data sample used in the analysis described later in this thesis. After some upgrades to both the Tevatron and the DØ detector, Run IIb commenced in June 2006, with the luminosity continuing to rise. Current projections of the luminosity predict that the between 4 fb^{-1} and 8 fb^{-1} will have been delivered by the end of Run II in 2009 [32].

	Run I(1993-1995)	Run IIa(2002-2006)
Energy(GeV)	900	980
Proton bunches	6	36
Antiproton bunches	6	36
Protons/bunch	2.3×10^{11}	2.7×10^{11}
Antiprotons/bunch	5.5×10^{10}	3.0×10^{10}
Bunch length(m)	0.60	0.37
Bunch spacing (ns)	≈ 3500	396
Interactions/crossing	2.5	2.3
Peak luminosity ($cm^{-2}s^{-1}$)	0.16×10^{31}	0.86×10^{32}
Integrated luminosity(pb^{-1}/week)	3.2	17.3

Table 4.1: Tevatron parameters for Run I and Run IIa.

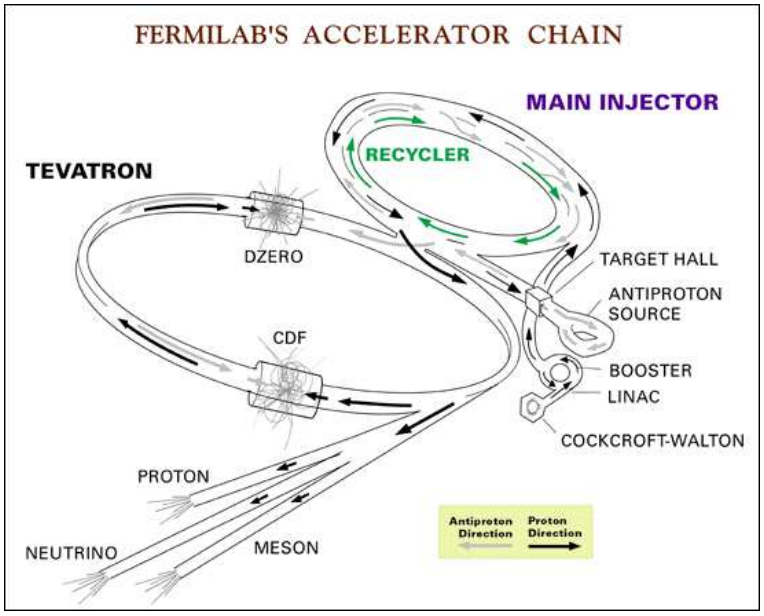

Figure 4.1: Diagram of the Fermilab accelerator complex.

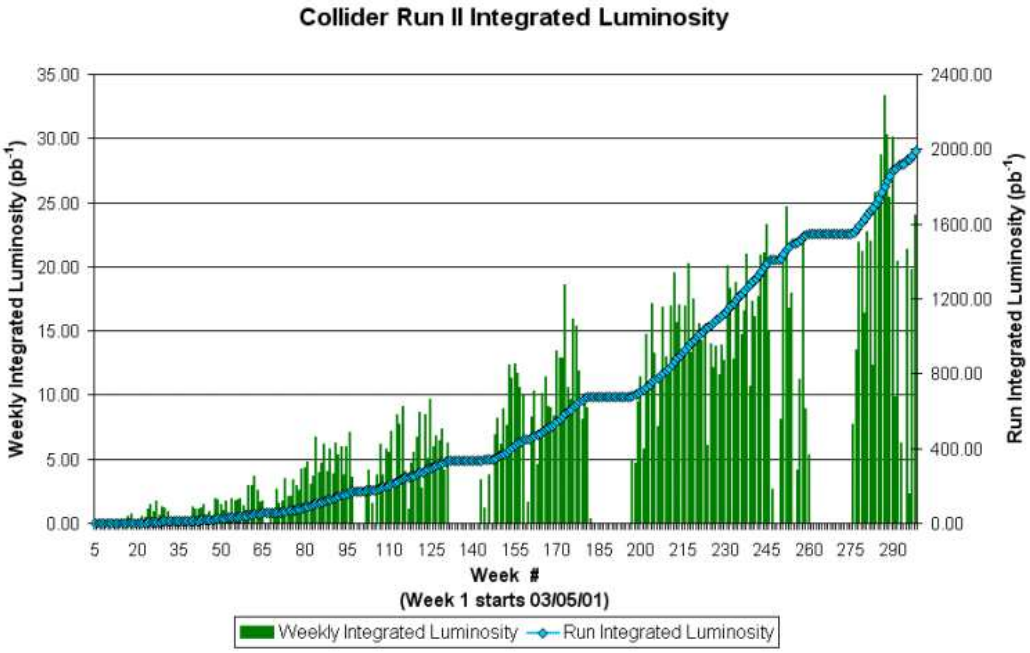

Figure 4.2: Plot of the weekly integrated luminosity and its cumulative total during Run II of the Tevatron.

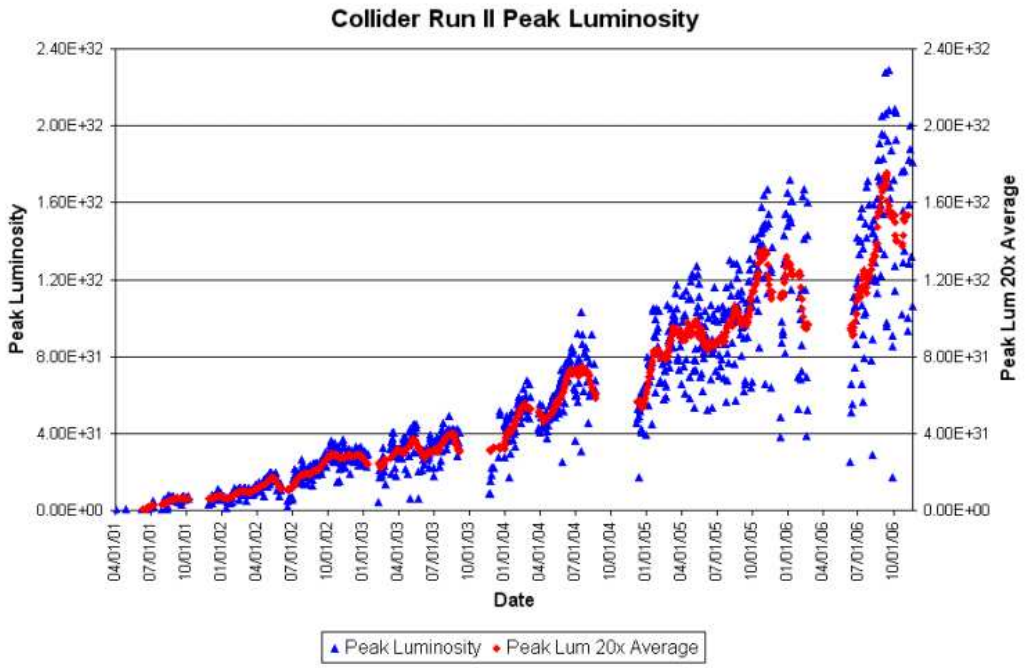

Figure 4.3: Plot of the peak luminosities obtained during Run II of the Tevatron.

4.2 The Run IIa DØ Detector

As mentioned previously, the Run II DØ detector is a significantly different piece of apparatus to that used during Run I. The upgrades were made to extend the scope of the detector, taking advantage of the improvements in the Tevatron. The major additions in the upgrade were the tracking system and the forward muon systems, while the original Run I calorimeter and the central muon system have been kept. The tracking system used during Run I did not have a magnetic field and suffered from radiation damage, so a tracking system capable of operating during the higher luminosity conditions of Run II was needed, with a magnetic field to allow momentum measurement. The forward muon system was also replaced, both to improve the coverage and to operate better in the Run II environment. The much smaller interval between bunch crossings in the detector also meant significant upgrades to the readout electronics and trigger system were made. This section provides an overview of the detector, further detail can be found in [33].

A diagram showing the main subsystems of the detector is shown in Figure 4.4. In common with most particle detectors, the DØ detector is essentially a cylinder with the beam pipe along the axis, with a layered structure of subdetectors. The various subsystems of the main detector are described in greater detail below, but first the definitions of coordinates used are given.

4.2.1 Coordinate System

A right handed system of co-ordinates with origin at the centre of the detector is used. The z-axis lies along the beam axis, pointing in the direction of the proton beam, and the y-axis points vertically upward. This means that the x-axis points away from the centre of the Tevatron ring. Often spherical polar coordinates are used, with the radial coordinate r lying perpendicular to the beam direction and the azimuthal angle given by $\phi = \arctan(y/x)$. The polar angle $\theta = \arctan(r/z)$

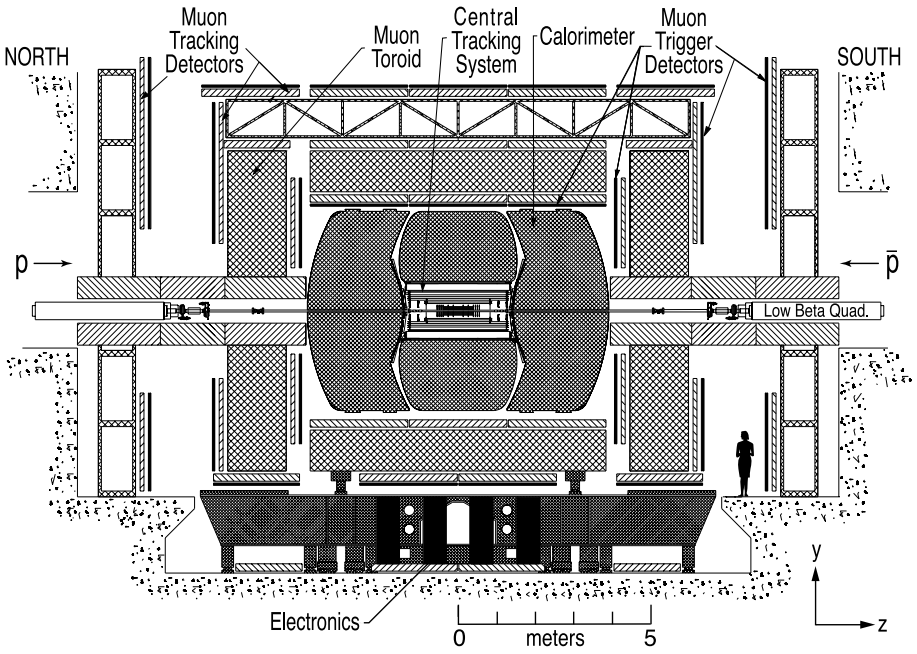

Figure 4.4: Cross-sectional view of the DØ Detector.

is usually replaced by the *pseudorapidity*, η, which is defined as

$$\eta = -\ln\left(\tan\frac{\theta}{2}\right). \tag{4.1}$$

The pseudorapidity is an approximation to the rapidity

$$y = \frac{1}{2}\ln\left(\frac{E+p_z}{E-p_z}\right) \tag{4.2}$$

for $E >> m$, where E, p and m are the energy, momentum and mass of a particle respectively. The two quantities are identical for massless particles.

The term *transverse* refers to the (x, y) plane, and quantities are often measured in this plane, such as the transverse momentum, $p_T = p\sin\theta$, and the transverse energy, $E_T = E\sin\theta$. The term *forward* refers to points at large $|z|$.

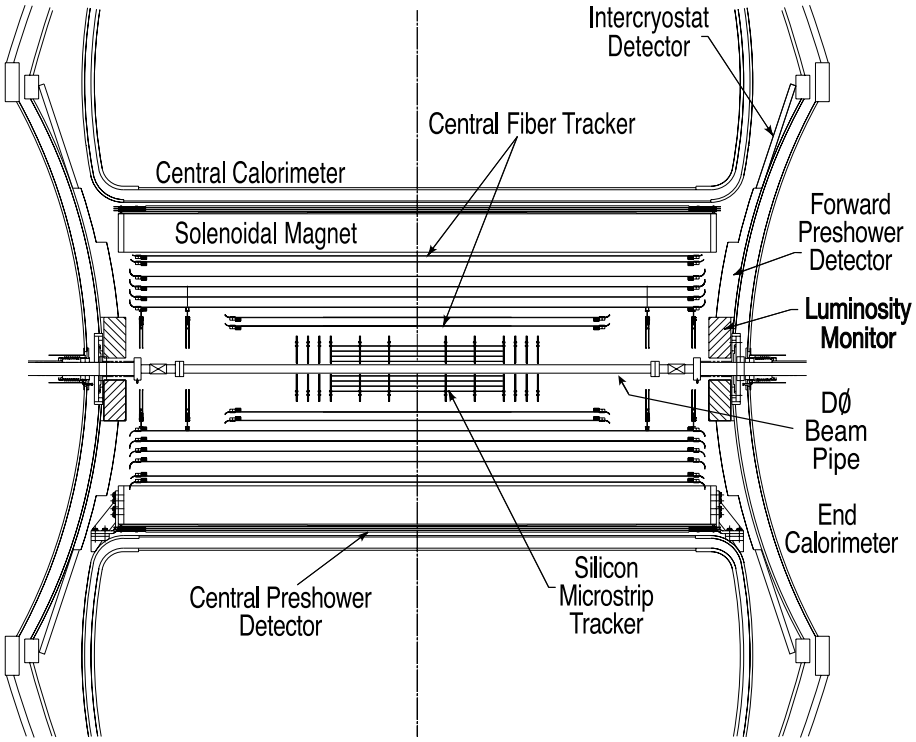

Figure 4.5: Cross-sectional view of the DØ central tracking system, also showing the luminosity monitors, preshower detectors and parts of the calorimeters.

4.2.2 Central Tracking

The tracking detectors are the closest detectors to the interaction region. The tracking system is indicated at the centre of the detector in Figure 4.4. It consists of a silicon microstrip tracker (SMT) closest to the beam pipe, surrounded by a scintillating central fibre tracker (CFT). These two subsystems are enclosed within a superconducting solenoid which provides a field of 2T. The system was designed to measure the momentum of charged particles over a large range of pseudorapidity, and allow the reconstruction of secondary vertices. The constituent parts can be seen in Figure 4.5, along with the adjacent parts of the detector.

The Silicon Microstrip Tracker(SMT)

The high resolution and radiation hardness of silicon detectors led to these being chosen for the precision vertex detector that surrounds the beam pipe. The

SMT has a structure of barrels and disks, as shown in the three-dimensional view in Figure 4.6. The layout is designed to accommodate the variation of the interaction point, which has a standard deviation in z of around 25 cm, while ensuring that particles cross the detector planes at near perpendicular angles. The barrels primarily provide measurements of the $r - \phi$ coordinates of a track, while the disks give three dimensional measurements for reconstruction of particles at high $|\eta|$ where there is no coverage by the CFT.

In the central region there are six barrel sections, each 12 cm long with an inner radius of 2.7 cm and an outer radius of 10.5 cm. These each contain eight layers of silicon detectors known as 'ladders'. A cross section of a barrel section, showing the arrangement of the ladders is shown in Figure 4.7. Each barrel section is capped at high $|z|$ by a disk containing 12 wedge-shaped detectors, known as an 'F-disk'. At either end of the central section lie three additional F-disks. In each of the forward regions there are two larger disks, known as 'H-disks'. These have an inner radius of 9.5 cm and an outer radius of 26 cm, and consist of 24 wedge-shaped sensors. The H-disks are located at $|z|$ =100.4 cm and $|z|$ = 121.0 cm, while the furthest forward F-disks are at $|z|$ =53.1 cm.

Various types of silicon sensor are used throughout the SMT. Most of the ladders are double sided sensors, with p-side axial strips oriented parallel to the beam, and n-side strips at a stereo angle. In layers 3, 4, 7 and 8 of the barrels, this angle is 2°. In layers 1, 2, 5 and 6 it is 90°, with the exception of the outermost two barrel sections which contain single sided axial detectors. The F-disks also contain double sided detectors, with strips on either side at a relative angle of 30°. The H-disk wedges each contain two single sided detectors mounted back-to-back, with the strips having a relative angle of 15°. The pitch of the strips in the detectors varies between the sensor types, as shown in Table 4.2. The signal to noise ratio in the detectors is between 12:1 and 18:1. The sensors are read out using custom made SVXIIe chips [34]. The pulse height information from these is used

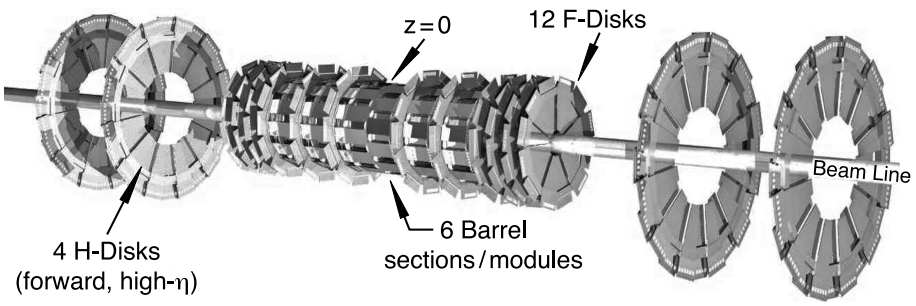

Figure 4.6: Diagram showing the disk and barrel structure of the silicon microstrip tracker (SMT).

Sensor	Pitch(μm)
Barrel axial	50
Barrel 2°	62.5
Barrel 90°	153.5
F-disk (p-side)	50
F-disk (n-side)	62.5
H-disk	80

Table 4.2: Strip pitch values for the different SMT sensors.

to calculate the centres of clusters of hit strips, and can also be used to calculate the energy loss, dE/dx, for low momentum tracks, to assist particle identification.

The Central Fibre Tracker(CFT)

The CFT is located outside the SMT, between 20 cm and 52 cm from the beam pipe. It consists of eight concentric cylinders, on each of which are mounted two doublet layers of scintillating fibres. The inner two cylinders are located within the outer radius of the SMT H-disks, so are 1.66m long. The remaining cylinders are outside the H-disks and are 2.52m long. This provides coverage to a value of $|\eta|$ of approximately 1.7. Each cylinder contains one doublet layer in which the fibres are oriented parallel to the beam, and one doublet layer in which the fibres are at a stereo angle of $+3°$ or $-3°$. The stereo angle alternates between these two values between adjacent cylinders. The fibres themselves are constructed from a polystyrene core with two claddings, and have an overall diameter of 835

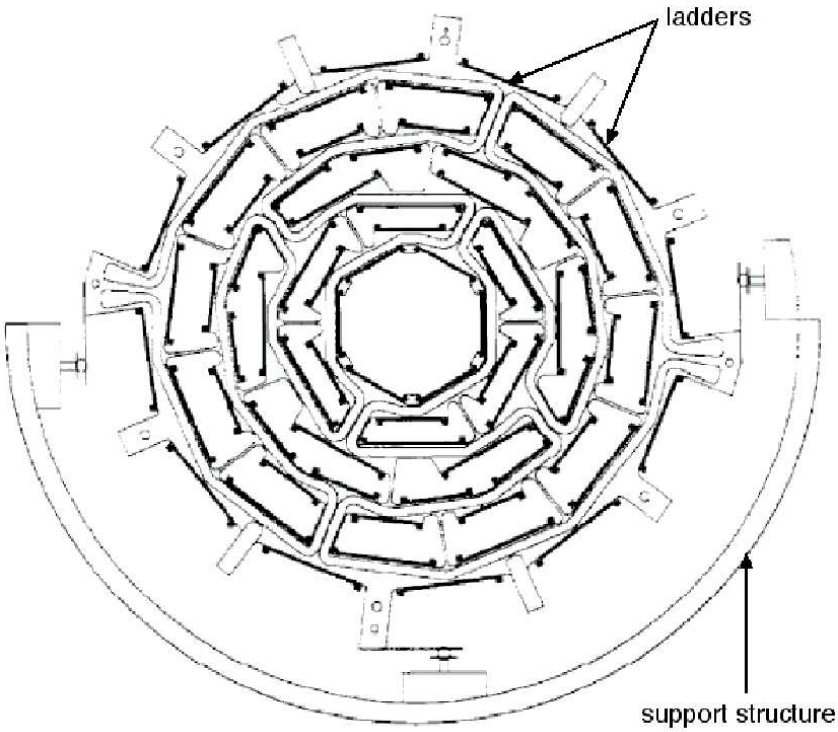

Figure 4.7: Cross section of an SMT barrel module.

μm. The polystyrene is doped with the fluorescent dye paraterphenyl and the wave-shifter dye 3-hydroxyflavone. Excitations in the polystyrene are transferred to the paraterphenyl, which undergoes fluorescence decay and emits light with wavelength of around 340 nm. The mean free path of this wavelength in the polystyrene is very short, so the wave shifter dye is used to absorb this light and emit light with a 530 nm wavelength, which travels large distances. Each fibre is connected by a clear fibre waveguide to a visible light photon counter(VLPC). The VLPCs are silicon avalanche photodetectors that have a high gain and high quantum efficiency, allowing them to detect single photons.

The Solenoid Magnet

The superconducting solenoid surrounds the tracking system. Its size was determined by the space inside the Run I calorimeter that is still used in the current

detector. The solenoid is 2.73 m long and 1.42 m in diameter. An operating field of 2 T was selected after consideration of tracking resolution dependence, and the dimensions of the components required. Since the available volume is relatively small the solenoid and its support cylinder and cryostat were required to be as thin as possible to avoid further reduction of the tracking volume. The solenoid was designed to have a uniform field over as much of the volume as possible, and this has been achieved to within 0.5% [35]. This uniformity was obtained by using a higher current density at the ends of the solenoid by using narrower windings of the conductor. Its thickness was designed to be approximately one radiation length, to give optimal performance of the central preshower (CPS) detector, which is located outside the solenoid.

Performance of Tracking System

The combined SMT-CFT system can measure the position of the primary vertex in the z direction with a resolution of around 35 μm. The resolution of the distance of closest approach to the beam axis is around 50 μm for a track with $p_T \approx 1$ GeV/c, but improves for higher p_T, with tracks with $p_T > 10$ GeV/c having a resolution of around 15 μm. This spatial resolution combined with the design magnetic field gives an expected transverse momentum resolution of $\Delta(p_T)/p_T \approx 0.002 p_T$ [35].

Problems have reduced the number of active tracking elements, but at May 2005 90% of the SMT sensors were functional. By September 2005 there were around 1500 dead fibres in the CFT, which is a fraction of around 2%. About half of these failures are due to dead VLPCs [36]. Since late 2004 the solenoid has been run at a 4550 A current instead of the design current of 4750 A, after it no longer could sustain this current reliably. This resulted in the magnetic field changing to 1.92T since this point.

4.2.3 Preshower Detectors

The preshower detectors are located between the tracking system and the calorimeters. They provide both position and energy measurements. Electron identification is aided by the shower sampling and improved spatial matching between tracks and calorimeter showers that they provide. The information can also be used to correct the electromagnetic energy measurement for the losses that occur in the tracking system and other materials encountered before the calorimeter. There are two separate preshower detectors, the central preshower (CPS) and the forward preshower (FPS). Both consist of scintillator strips that have a triangular cross section with sides of approximately 6 mm. The strips are nested together so that most tracks will traverse two strips. In the centre of each strip is a wavelength shifting fibre that collects the scintillation light. Readout of the fibres proceeds similarly to the CFT fibres, using waveguides and VLPCs.

The Central Preshower Detector(CPS)

The central preshower detector is indicated in Figure 4.5. It is a barrel-shaped detector that lies in the 5 cm gap between the solenoid and the central calorimeter, covering the region $|\eta| < 1.3$. Between the CPS and the solenoid is a lead absorber approximately 0.55 cm thick. The absorber and the solenoid provide approximately two radiation lengths of material for showering before the CPS. The CPS consists of three layers of strips. Strips in the inner layer are oriented axially, while the central and outer layers have strips at stereo angles of approximately $\pm 24°$.

The Forward Preshower Detector(FPS)

The forward preshower detectors are also indicated in Figure 4.5. They are mounted on the inside faces of the end calorimeter cryostats, between the luminos-

ity monitor and the intercryostat detector. They contain two layers of detectors, which are separated by a lead-stainless-steel absorber. In each of the layers there are two measuring planes, with strips at a relative angle of 22.5°. The layer of detectors closest to the interaction region is known as minimum ionising particle (MIP) layer, while the layer on the opposite side of the absorber is known as the shower layer. The MIP layer gives a spatial measurement for charged particles passing through, before they go on to produce showers in the absorber which are sampled by the shower layer. The level of showering can be used to discriminate between electrons and heavier particles, while signals in the shower layer not accompanied by a MIP signal are indicative of a photon or π^0. The coverage of the shower layers is in the range $1.5 < |\eta| < 2.5$, while the region $1.65 < |\eta| < 2.5$ is covered by the MIP layers and the absorber. In the region $1.5 < |\eta| < 1.65$ particles will traverse the solenoid material, producing showers before the FPS is reached, so this region is covered by only the shower layer.

4.2.4 Calorimeters

The DØ calorimeters provide measurements of the energy of electrons, photons and jets, as well as measuring the overall transverse energy in an event. The calorimeters were part of the original detector in Run I [37], although the front end electronics were replaced during the Run II upgrade in order to cope with the higher bunch crossing frequency. They are sampling calorimeters which use liquid argon as the active material. Particles traversing the calorimeter pass through alternating layers of absorber and liquid argon. The absorber plates induce electromagnetic or hadronic showers, which then cause ionisation of the liquid argon. The resulting charge is collected and measured to estimate the energy deposited.

The structure of the calorimeters is shown in Figure 4.8. There are three separate calorimeters, consisting of a central section which covers up to $|\eta| \approx 1$,

and two end caps which cover the region between $|\eta| \approx 1$ and $|\eta| \approx 4$. Each section is located within a separate cryostat, which maintains the calorimeter temperature at around 90 K. Each calorimeter section contains electromagnetic regions and fine and coarse hadronic regions which use different types of absorber. The electromagnetic sections use plates of nearly pure depleted uranium of 3 or 4 mm thickness interspersed between 2.3 mm layers of liquid argon. In the fine hadronic sections the absorbers are 6 mm thick and are made of uranium-niobium(2%) alloy, whereas the coarse hadronic regions use 46.5 mm plates which in the central section are copper and in the end calorimeters are stainless steel.

The calorimeter is segmented into individual readout cells, which typically cover an area $\Delta(\eta) \times \Delta(\phi) \approx 0.1 \times 0.1$. These cells are arranged in layers to allow measurement of the longitudinal shower shape. There are four layers of cells in the electromagnetic regions. The third layer is at the EM shower maximum and the cells are segmented twice as finely in η and ϕ in this layer. The majority of hadronic showering occurs in the fine hadronic sections, which contain three layers of cells. Any remaining hadronic energy is deposited in the coarse hadronic section where there is a single readout layer. The calorimeters can measure the energy, E, of electrons, photons and jets with a resolution approximately given by $\sigma(E)/\sqrt{E} \approx 0.2$ [38, 39, 40]. The energy uncertainty is given by $\sqrt{N}$, where N is the number of particles produced in the shower. N increases proportionally with the energy E, and hence $\sigma(E)$ is proportional to $\sqrt{E}$.

Intercryostat Detector(ICD)

Particles traversing the gaps between the central and end calorimeters encounter large amounts of unsampled material, such as the cryostat walls and readout electronics that lie in the gaps. The energy lost in this material reduces the energy resolution. The ICDs provide sampling in the region between the cryostats, in order to correct for this energy loss. They are mounted on the end cryostat faces

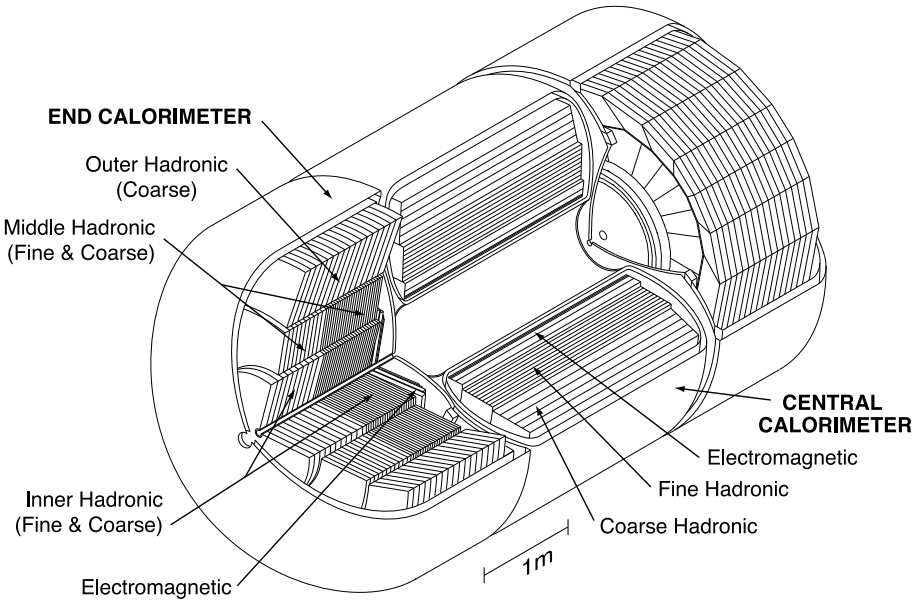

Figure 4.8: Diagram of the the DØ calorimeters.

as indicated in Figure 4.5, and cover the region $1.1 < |\eta| < 1.4$. The ICDs are scintillator tile arrays, with a segmentation in η and ϕ which matches that of the calorimeter cells. Wavelength-shifting fibres in the tiles transport the scintillation light to clear optical fibres which lead to photomultiplier tubes(PMTs).

4.2.5 Muon System

Electrons, photons and hadrons are generally expected to deposit their entire energy in the calorimeter. Apart from neutrinos, muons are the only particles that are likely to traverse the full calorimeter thickness, since they do not readily lose energy by showering. Layers of drift tubes and scintillation counters outside the calorimeters provide capabilities for muon triggering and reconstruction. The drift tubes provide precise spatial measurements, while the scintillation counters give a fast signal to allow triggering. These detectors are located either side of a system of toroidal magnets, which bend the muon trajectory to allow measurement of the momentum. The muon system is split into two regions, which are described separately below. The central muon system provides coverage for $|\eta| < 1.0$, while

the forward muon system covers the range $1.0 < |\eta| < 2.0$.

The Central Muon System

For coordinate measurements, the central muon system uses three layers of proportional drift tubes (PDTs), which lie in planes in x and y. The inner 'A' layer is inside the central toroid, while the 'B' and 'C' layers are outside. The central toroid, which is visible in Figure 4.4, provides a field of 1.8 T to bend the path of muons in the $r - z$ plane. Each PDT layer does not provide complete coverage, so only 55% of the central detector region is covered by all three layers, but around 90% is covered by at least two. The PDTs are made of rectangular aluminium tubes, which form individual drift cells. The B and C layer PDTs have a thickness of three cells, whereas those in the A layer are mostly four cells deep. The cells have a width of 10.1 cm and lengths up to 6 m. They are filled with a gas mixture consisting of 84% argon, 8% methane and 8% CF_4. An anode wire runs along the centre of each cell, with cathode pads located above and below it. Particles passing through the gas release electrons which drift to the wire with a velocity of around 10 cm/μs, giving a maximum drift time of around 500 ns. The arrival time of charge at the wire allows the drift distance to be calculated with a resolution of approximately 1 mm, giving a measurement of the z coordinate of the hit. Each anode wire is connected to readout electronics at one end of the cell, and at the other end is connected to the wire in the neighbouring cell. Hence the cells form pairs, so that a hit in one of the cells is read out by both sets of readout electronics. The difference in the timing of the two signals allows the position of the hit along the wire to be estimated with a precision between 10 cm and 50 cm. Charge deposition on the cathode pads gives the position of the hit along the wire with precision of about 5 mm in cells where the pads are instrumented. All A layer pads are instrumented, but in the B and C layers this is only the case for around 10% of cells.

A layer of scintillation counters is located outside the C layer PDTs, and there is also a layer between the calorimeter and the A layer PDTs. The former are known as the 'cosmic cap' and 'cosmic bottom' and the latter are known as the 'Aϕ counters'. The maximum drift time for the PDTs is larger than the bunch crossing interval of 396 ns, so a faster detector is needed to allow triggering and to associate PDT hits with the correct bunch crossing. The cosmic cap and bottom counters provide accurate timing signals to match PDT hits to a bunch crossing or reject them as cosmic ray background. Hits in the Aϕ counters are matched to tracks in the CFT to provide muon triggers with p_T thresholds. They also provide the timing information for low p_T muons which are absorbed by the toroid and do not reach the outer layers. The scintillators in both of the layers have a segmentation in ϕ of approximately 4.5°. Wavelength shifting fibres embedded in the scintillator material lead to PMTs for readout. The time resolution for a scintillator hit is approximately 2 ns.

The Forward Muon System

The forward muon system covers the range of $|\eta|$ between approximately 1.0 and 2.0, and is comprised of mini drift tubes (MDTs) and scintillation counters. The MDTs are similar to PDTs but have smaller cells, which have a cross section of only 9.4 mm × 9.4 mm. The arrangement of MDTs is similar to the PDTs of the central region, with an 'A' layer between the end calorimeter and end toroid and 'B' and 'C' layers forward of the end toroid. Also each of the layers contains the same number of planes of drift cells as the corresponding layer in the central region. The cells have a 50μm thick gold-tungsten anode wire, and a conductive inner surface that forms a cathode. They contain a gas mixture of 90% CF_4 and 10% methane. The smaller cross section of the cells gives an electron drift time of less than 60 ns, so there is no problem in associating the hits with a particular bunch crossing. The coordinate resolution of the MDTs is approximately 0.7 mm.

The main contribution to this is from the digitising electronics, which measures the signal arrival time with an uncertainty of 18.8 ns.

In the forward muon system there are also three layers of scintillation counters. These provide timing measurements with a resolution of less than 1 ns, to reject background MDT hits and trigger on muon events. The scintillators have a segmentation of 4.5° in ϕ and 0.12 or 0.07 in η.

4.2.6 Luminosity Monitor

The instantaneous luminosity at DØ is measured by determining the fraction of bunch crossings in which one or more inelastic collisions occurs. These collisions result in proton and antiproton remnants being scattered to small angles, even if no hard scatter occurs. The luminosity monitor (LM) detectors, which are indicated in Figure 4.5, are positioned to detect these remnants. They are located on the inside faces of the end calorimeters, in the radial region between the forward preshower detectors and the beam pipe. This corresponds to the pseudorapidity range $2.7 < |\eta| < 4.4$. Each of the two LM detectors is a circular array of 24 plastic scintillating wedges, on each of which is mounted a photomultiplier tube for readout. The rate of hits in the LMs is combined with the inelastic cross section and the acceptance of the LMs to estimate the luminosity. The information from the LMs is also used for the most basic level of triggering, as discussed in the next section.

4.2.7 Trigger System

Collisions at DØ occur at a rate of approximately 2.5 MHz, which greatly exceeds the rate at which it is feasible to record data to tape. This is because only a small fraction of collisions produce interesting physics processes, and the luminosity is maximised to produce such events at the highest possible frequency. Therefore

a trigger system is used, which makes a fast examination of the detector signals to decide whether an event should be recorded. The DØ trigger consists of three levels of decision making, which are described separately below. Successive levels give a more detailed evaluation of the events that are passed to them. The trigger system is designed to accept events at a rate of around 50 Hz. The rate to tape is limited to this value due to the time taken for events to be fully reconstructed offline.

Level 1(L1)

The L1 trigger uses information from all of the detector subsystems besides the SMT to initially examine each event for features of interest. In Figure 4.9 the flow of information through the level 1 and level 2 trigger systems is shown. Each of the L1 subsystems uses hardware based on field programmable gate array (FPGA) technology to determine whether objects in the detectors satisfy the conditions defined by various trigger terms. This information is sent to the trigger framework(TFW), which uses FPGAs to combine the information from the separate subsystems. The TFW defines up to 128 triggers using different logical combinations of the information. The passing of one of these triggers, along with coincident hits in the luminosity monitors is sufficient for the TFW to issue an L1 accept. The full evaluation of an event by L1 is performed in approximately 4 μs, and events are accepted at a rate of around 1.6 kHz.

The L1CAL trigger sums the transverse energy deposited in columns of calorimeter cells known as 'trigger towers'. These point away from the interaction region, and each tower covers an area $\Delta\eta \times \Delta\phi = 0.2 \times 0.2$. A set of threshold energies is defined, and the number of towers with energy above each threshold is counted. A trigger term is satisfied if the count exceeds a certain number of towers. The total transverse energy is determined by summing the values for all towers, and trigger terms are defined using thresholds on the total E_T and the amount of missing E_T.

Thresholds are also set on the E_T value for small groups of neighbouring towers, in order to trigger on jets.

The level 1 central track trigger (L1CTT) uses the fast responses of the CFT, CPS and FPS detectors to provide triggering on tracks at level 1. Track candidates are found by comparing hit patterns in the CFT axial layers with hit maps generated by a set of 20,000 predefined track equations. The track candidates are sent to the level 1 muon trigger system, for use in muon triggers. Electron candidates are found by matching hits in the CPS axial layers to CFT track candidates. Several trigger terms are defined, using combinations of criteria including p_T thresholds, isolation of tracks, and the existence of a matching CPS cluster. Separate trigger terms are used for the FPS, which triggers on electron candidates by matching MIP layer track stubs with shower layer clusters.

The L1Muon trigger system forms muon candidates using information from the muon system and the track candidates found by the L1CTT trigger. One set of candidates are formed by matching scintillator hits to central track candidates. Muon candidates are also formed by reconstructing track stubs from drift tube hits, providing the hits are confirmed by scintillator hits. Track stubs in each of the layers are then matched to create higher quality muon candidates. Various muon trigger terms are defined using different sets of requirements.

Triggering is also performed using hits observed in the forward proton detectors(FPDs). These are separate from the main detector, lying at $|z| > 23$ m. They are close to the beam pipe to detect intact protons and antiprotons that are scattered to very small angles.

Level 2(L2)

The detector-specific L2 subsystems, shown in Figure 4.9, use additional information and more sophisticated algorithms to improve identification of the objects reconstructed at level 1. The information from the separate subsystems is

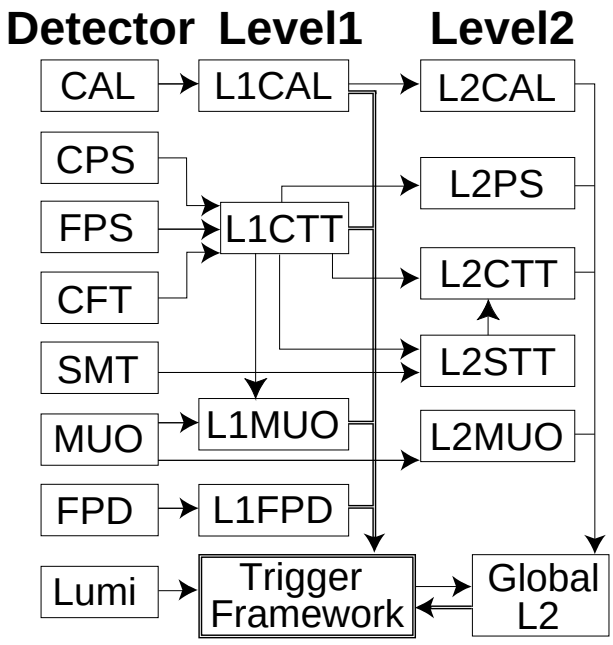

Figure 4.9: Overview of the Level 1 and Level 2 trigger systems. The flow of trigger-related information between the subsystems is indicated by the arrows.

then combined by the level 2 global (L2Global) system, which reconstructs global physics objects based on the individual objects and the correlations between detector signatures. L2Global then filters the global objects, using criteria set by the current trigger list. Each of the 128 L1 triggers has an associated L2 trigger. If a particular L1 trigger is fired, L2Global runs scripts associated with this trigger, to test whether the additional criteria applied at L2 are satisfied. The L2 algorithms are performed by a combination of FPGAs and microprocessor chips, which evaluate an event in around 100 μs. The L2 system is designed to accept events at rates up to 1 kHz.

The L2CAL processor runs an algorithm which identifies jets by finding clusters of trigger towers around high E_T seed towers. A similar algorithm separately finds clusters in the electromagnetic regions only, to identify electron and photon candidates. Muon identification at L2 is improved by timing and calibration information that is not used at L1. Muon candidates are assigned track parameters and quality information before they are sent to L2Global. The L2PS system per-

forms spatial matching between axial and stereo clusters in the CPS. Matches in all three layers are identified as electron candidates if a CFT track was matched at L1, or photon candidates otherwise. Calorimeter trigger towers with consistent (η, ϕ) coordinates are also matched to preshower clusters at this stage.

Tracking at level 2 is improved by the inclusion of the SMT, which reads out too slowly to be used in the L1 trigger. The level 2 silicon track trigger (L2STT) receives the list of tracks found by the L1CTT. SMT hits are assigned to each track by defining a 'road' around the track, which is extrapolated back to the SMT. Hits in axial ladder strips of the SMT are assigned to the track, and the track is refitted. The addition of the SMT hits allows a precise measurement of the impact parameter of the track with respect to the beam, which helps to identify and trigger on decays of long-lived particles such as b-hadrons. The updated track candidates are sent to L2CTT, which sorts tracks by p_T and impact parameter before they are passed to L2Global.

Level 3(L3)

The full detector readout is available for the L3 trigger, which reconstructs events similarly to the offline reconstruction software(described in Chapter 5), although using simpler and faster algorithms. Software tools reconstruct detailed physics objects and calculate relationships between them, such as invariant masses and relative angles. The L3 criteria of the current trigger list are then applied by calling a number of filter scripts. Each level 2 trigger fired leads to filter scripts associated with that trigger being executed. Filters are applied to the physics objects and their relationships. The passing of all filters in a script satisfies the L3 trigger and the event is recorded. The L3 algorithms are run by a farm of PCs, which each run the L3 software independently. Upon acceptance by L2 an event is sent to an individual node to be examined by L3. The L3 decision is typically made in 100-150 ms, and the level of rejection is set to achieve the target of 50

Hz rate to tape.

Tracks are reconstructed using the full axial and stereo information from the SMT and CFT, and the primary vertex position is calculated. The impact parameters of tracks with respect to the vertex can be measured with a resolution of 25 μm, allowing triggering on b-hadrons. Knowledge of the vertex position also improves the identification of other physics objects. The cone algorithms that identify jets and electrons in the calorimeter rely on high precision calorimeter information as well as the primary vertex measurement. A more accurate calculation of missing E_T is also obtained by centring the sum on the vertex. Muons are reconstructed using the full muon system information, and muon candidates are extrapolated to the CFT and matched to central tracks, giving improved momentum resolution over the muons at L2.

Chapter 5

Event Reconstruction and Simulation

Events accepted by the level 3 trigger are written to tape in the form of raw detector signals. Before physics analysis can take place, these must be analysed to reconstruct the physics objects present in the event. A large number of particles are produced in a typical DØ event, so reconstruction is a complex and time consuming process. The efficient reconstruction of events is crucial for the success of physics analyses. The analysis presented in this thesis relies particularly on the algorithms for the reconstruction of tracks and the identification of muons. After giving an overview of the reconstruction process, this chapter describes these algorithms in greater detail. Important inputs to the analysis are also obtained using simulated data samples, so the processes used in generating these are described in the final section.

5.1 DØRECO

Events written to tape are later processed by the DØ reconstruction code, which is known as DØRECO [41]. This converts the raw data for each event into a for-

mat known as the 'thumbnail', which contains details of the reconstructed physics objects and can be used as the input to physics analyses. The initial processing takes place using a computing farm at Fermilab. However, the DØRECO code is constantly updated to give improved reconstruction of physics objects. After a major new release of the code, the data obtained up to that point are reprocessed using the new version. The $p14$ release was the first to contain the new combination of tracking algorithms described in section 5.2. In late 2003, the collaboration began reprocessing all the existing data set with this new DØRECO version, using offsite computing facilities in Texas, France, Germany, the Netherlands, the UK and Canada. Around 100 pb^{-1} of data reconstructed with earlier versions of DØRECO was reprocessed using $p14$ over a period of approximately two months. A similar larger reprocessing took place between March and November 2005, using the later $p17$ version of DØRECO. Approximately half of the sample used for the analysis was obtained from a skim of the $p14$ processed data, while the remainder was initially reconstructed with $p17$. However, in terms of tracking there are no significant differences between $p14$ and $p17$.

The first stages in the reconstruction of an event by DØRECO involve unpacking the raw data and decoding and calibrating it to map the physical locations and determine the energies of hits and clusters. The data are calibrated by referring to a database of calibration constants. The detectors are regularly calibrated using special calibration runs, which extract the noise levels and gains for each electronic channel. For the calorimeter, a calibration run is usually performed for a few minutes following the end of each store. The calibration constants obtained are transferred to the online calibration database for use in the trigger, and to the offline calibration database which is accessed by DØRECO. In the next stage, DØRECO executes algorithms to reconstruct charged particle trajectories in the central tracking system. The tracks are then used in the next stage to determine the position of the primary vertex and identify displaced secondary vertices.

Finally algorithms for the identification of physics objects are executed. These match information from the various detectors to reconstruct electrons, photons, muons, jets and missing E_T. The reconstruction of tracks and muons are described in the following sections.

5.2 Track Reconstruction

The current DØ tracking procedure is the result of testing of different pattern recognition algorithms on a variety of data and Monte Carlo samples [42]. To ensure a consistent high performance over a wide range of track conditions, a combination of algorithms was chosen for use in DØRECO. The three algorithms used are known as Histogram Track Finding (HTF), the Alternative Algorithm (AA) and Global Track Finder (GTR). The method of combining the three algorithms in DØRECO is shown in Figure 5.1 [43]. HTF and the pattern recognition phase of AA first run simultaneously to produce a combined pool of track hypotheses. The two algorithms complement each other since AA has a higher efficiency for low p_T and high impact parameter tracks, while HTF has better performance for high p_T. The filter phase of AA is then applied to the hypothesis pool to select the best track candidates. The final fitting of the track parameters is performed by GTR, which computes fitted trajectories that account for the effects of multiple scattering and energy loss in the detectors. The combination of the algorithms results in typical efficiencies of 85-90%, and a fake rate of below 2% across the p_T spectrum.

5.2.1 Clustering

The initial stage of track reconstruction involves the assignment of hits in the tracking detectors. A charged particle traversing an element of the SMT or CFT often registers signals in multiple neighbouring strips or fibres, so an individual

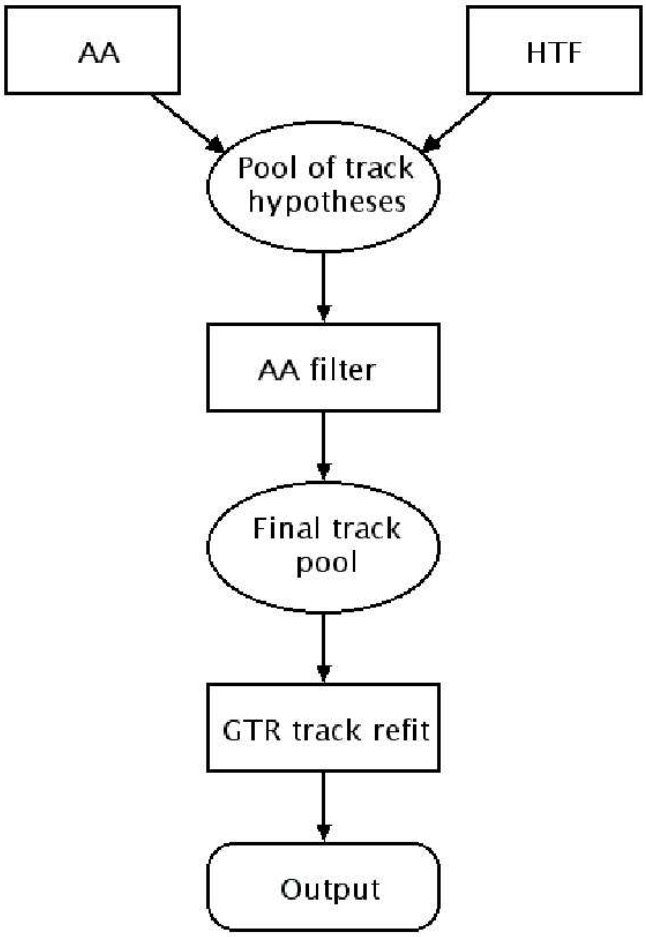

Figure 5.1: Flow diagram showing the stages of track reconstruction in DØRECO.

hit is assigned at the position of a contiguous cluster of hit strips or fibres. Contiguous sets of SMT strips which register a pulse above a set threshold are formed into clusters. The position of the SMT cluster is then calculated by averaging the positions of the strips with each weighted by its pulse height. Clustering in the CFT is performed using contiguous strips registering a light yield above a threshold, with the cluster position calculated as the average of the fibre positions. The pattern of clusters is then processed by the track reconstruction algorithms.

5.2.2 Track Finding by AA

The Alternative Algorithm (AA) [44] is the most recently developed of the three tracking algorithms. Its main aims were to improve the reconstruction of low momentum tracks and to reduce the level of fake tracks. It also significantly increased the capability for reconstructing high impact parameter tracks. These advances enable efficient reconstruction of particles such as the Λ^0 and K^0_S, which decay to low momentum tracks at relatively large distances from the primary vertex.

Construction of Track Hypotheses

The first stage of the algorithm builds all track hypotheses that fulfil a set of criteria, and adds them to the hypothesis pool to await filtering. At this stage a track hypothesis is allowed to share any number of hits with a different hypothesis. Since an axial SMT strip or CFT fibre is intersected by a large number of stereo strips or fibres, multiple tracks crossing the same detector will lead to many potential associations of axial and stereo layer measurements. Therefore a track hypothesis in the $r-\phi$ plane may be associated with a number of possible projections in $r-z$ plane. To construct a track hypothesis, the algorithm connects axial hits to create a single $r-\phi$ hypothesis, but does not attempt to deduce the correct $r-z$ projection at this stage. Instead all the potential $r-z$ projections

are stored and the best is selected when the tracks are combined into a vertex in the filtering stage.

Hypothesis construction begins by selecting a series of three axial hits in the SMT, each of which must have one or more associated stereo hits. The first hit may lie in either of the inner six layers of the barrels or in an F-disk, and the second may lie in any layer outside the first. The difference in axial angle between the first and second hits is required to be less than $\Delta\phi_{max} = 0.08$ radians, as shown in Figure 5.2. The third hit may lie in any subsequent layer, and must give a track hypothesis with a radius of greater than $R_{min} = 30$ cm and an axial impact parameter with respect to the z-axis of less than $IP_{max} = 2.5$ cm. The minimum radius corresponds to a minimum p_T requirement of 180 MeV/c.

Each initial hypothesis is then extrapolated to the following SMT or CFT layer and the expected crossing region is calculated, as indicated in Figure 5.3. A hit within this region is assigned to the hypothesis and the track is refitted. If more than one hit lies in the expected crossing region then a new hypothesis is formed for each additional hit. If no hit is found, yet the detector is known to be active, then a *miss* is recorded for the hypothesis. To allow for detector inefficiencies, a certain number of misses are allowed for a hypothesis. These are classed as *inside* misses, in which a miss is found between two hits, and *forward* and *backward* misses, which are misses on the track if it is extrapolated forwards or backwards through the detector.

The process of extrapolating to the next layer is repeated until the outside of the CFT is reached or three consecutive misses are recorded following a hit. The tracks saved to the final hypothesis pool must then fulfil the following conditions:

- At least 4 layers (SMT or CFT) containing both an axial and stereo hit;
- Number of inside misses ≤ 3;
- Number of inside misses in SMT ≤ 2;

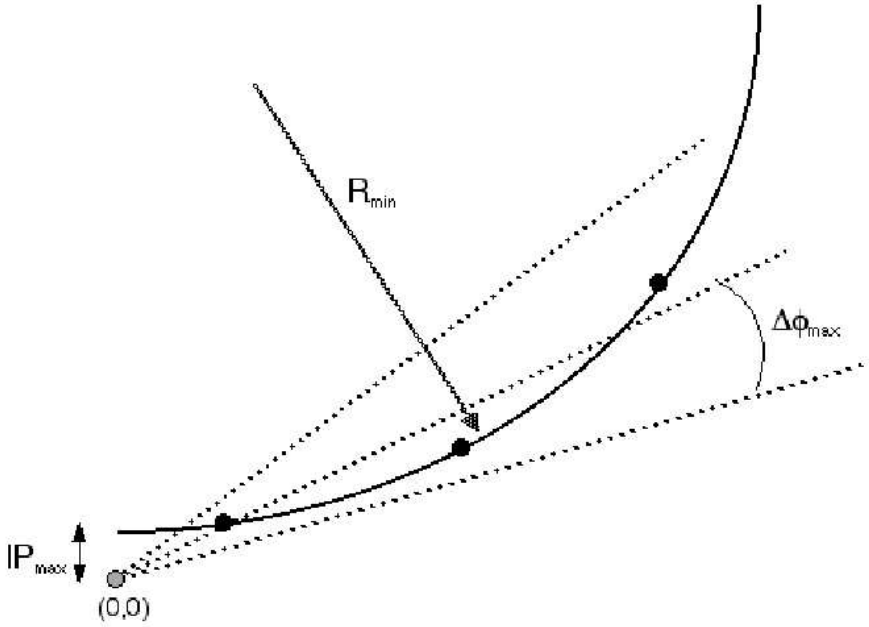

Figure 5.2: Initial requirements for a track hypothesis in the AA algorithm. The second hit must lie within axial angle $\Delta\phi_{max}$ relative to the first. The three-hit hypothesis must have a radius greater than R_{min} and an axial impact parameter less than IP_{max}.

- Number of (forward + backward) misses ≤ 6;
- At least 5 times as many hits as misses;
- If a hypothesis has one or more inside misses:
  - Number of (inside + forward) misses ≤ 4;
  - Number of (inside + backward) misses ≤ 3.

Track Filtering

The list of accepted tracks is obtained using a two pass filtering procedure. The first filtering produces a preliminary list of tracks, from which the positions of primary vertices are estimated. The final list of tracks is obtained by repeating the filtering, with the vertex locations used to impose additional criteria.

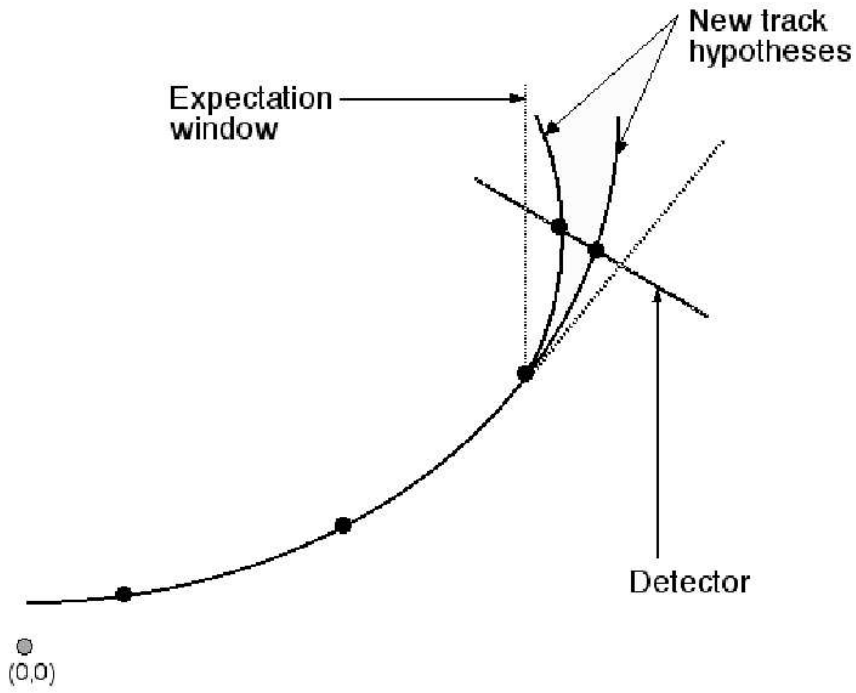

Figure 5.3: Extension of a track hypothesis in the AA algorithm. Hits in the subsequent detector layer that lie within the expectation window are associated to the hypothesis. Additional hypotheses are created if the window contains multiple hits.

For the first filtering the hypotheses are placed in descending order according to the number of hits on the track. For tracks with equal numbers of hits, those with fewer total misses are placed first. If the numbers of misses are also equal, then the χ^2 value of the track fit is used to discriminate, with lower values placed ahead. The hypotheses are then considered in the order that they are listed, and are accepted as tracks if they meet criteria on the number of hits that are shared with previously accepted tracks. If N_{shared} is the number of shared axial hits and N_{total} is the total number of axial hits, then the hypothesis must satisfy:

- $N_{shared} \leq \frac{2}{3} N_{total}$;
- $N_{shared} \leq \frac{1}{5} N_{total}$ OR $N_{total} - N_{shared} \geq 4$.

Using the tracks accepted, the primary vertices are then found by the AA vertexing algorithm, which is based on a method used by the DELPHI collaboration [45, 46]. To obtain the final track list, the hypotheses in the pool are reordered so that those passing close to a primary vertex are preferred over those that are more offset. This is achieved by adding two artificial hits to each hypothesis that has a small impact parameter with respect to a vertex. The ordering and filtering described above is then repeated. This method ensures that for pairs of hypotheses with many shared hits, a track passing close to the primary vertex is favoured over a displaced track, and hence the number of fake tracks should be reduced.

CFT-only Tracks

Some tracks have hits only in the CFT or very few SMT hits, so a separate CFT-only track search is performed. This takes place after the filtering of SMT-based hypotheses, because the primary vertex positions are needed to assist the CFT track search. The number of potential combinations of axial and stereo hits is typically much higher in the CFT than the SMT, so many more possible stereo

projections remain for CFT-only tracks. These are reduced by requiring that the CFT-only tracks pass close to a primary vertex in both the (r, ϕ) and (r, z) planes when they are extrapolated backwards. CFT track hypotheses are constructed in a similar manner to the hypotheses that begin in the SMT. The tracks are then extrapolated backwards and any possible SMT hits are added. The CFT-based hypotheses are subjected to the same criteria as given above, with the additional requirement that the axial and stereo impact parameters with respect to a primary vertex must be less than 1.5 cm.

5.2.3 Track Finding by HTF

The Histogram Track Finding (HTF) algorithm [47] was developed as an alternative to the GTR road-finding method which was initially used at DØ. The road-finding method performs well but is very time consuming for the hit multiplicities that typically occur at DØ, so a faster algorithm to perform the initial pattern recognition was desirable. The HTF algorithm was developed from techniques used in bubble chamber experiments in the 1950's.

The Hough Transform

The projection of a track in the $x - y$ plane may be described by three parameters. These are the curvature, $\rho = qB/p_T$ (where B is the magnetic field and q is the particle charge), the distance of closest approach to the beam axis, d_0, and the track direction at the point of closest approach, ϕ. When searching for tracks with small impact parameters these can be reduced to the two coordinates ρ and ϕ, and any such track can be represented by a point in the (ρ, ϕ) parameter space. In this parameter space, a hit in the tracking detectors is represented by a line, or by a band if the errors on the hit position are included. A number of hits belonging to the same track will produce a set of bands which intersect at the

point representing the track parameters. The HTF algorithm splits the parameter space into discrete regions, creating a 2-dimensional histogram. The band for each hit is plotted on the parameter space, and the histogram cells it covers are each incremented. This leads to a peak in the histogram where the hits from the same track intersect. These steps are illustrated in Figure 5.4.

In a similar way the projection of a track in the $r-z$ plane can be represented by the coordinates (z_0, C), where z_0 is the point on the z axis where the track intersects, and $C = dz/dr$ is the angle of the track in the $r-z$ plane. The (z_0, C) plane is histogrammed in a similar way to the (ρ, ϕ) plane and the stereo hits are used to create stereo track candidates.

Track Finding Strategy

The algorithm runs two separate track finding methods. One method produces the (ρ, ϕ) and (Z_0, C) histograms for SMT hits to find tracks in the SMT. These are then extended outward and CFT hits are added. The other method builds CFT tracks which are then extrapolated inward to add SMT hits. The two sets of tracks are combined and duplicates are removed. In practice the large number of hits at DØ leads to substantial background in the histograms, which complicates the identification of tracks. Instead of simply finding peaks, cells with entries below a threshold are discarded and all remaining cells are treated as track candidates. These then undergo filtering using a Kalman filter. This fits the track candidates similarly to the fitting described in the next section, but rejects the track if the incremental χ^2 increase due to adding a hit is above a limit.

5.2.4 Track Fitting

After track candidates are identified by the pattern recognition algorithms of HTF and AA, the final fitting of the track parameters and their errors is performed by

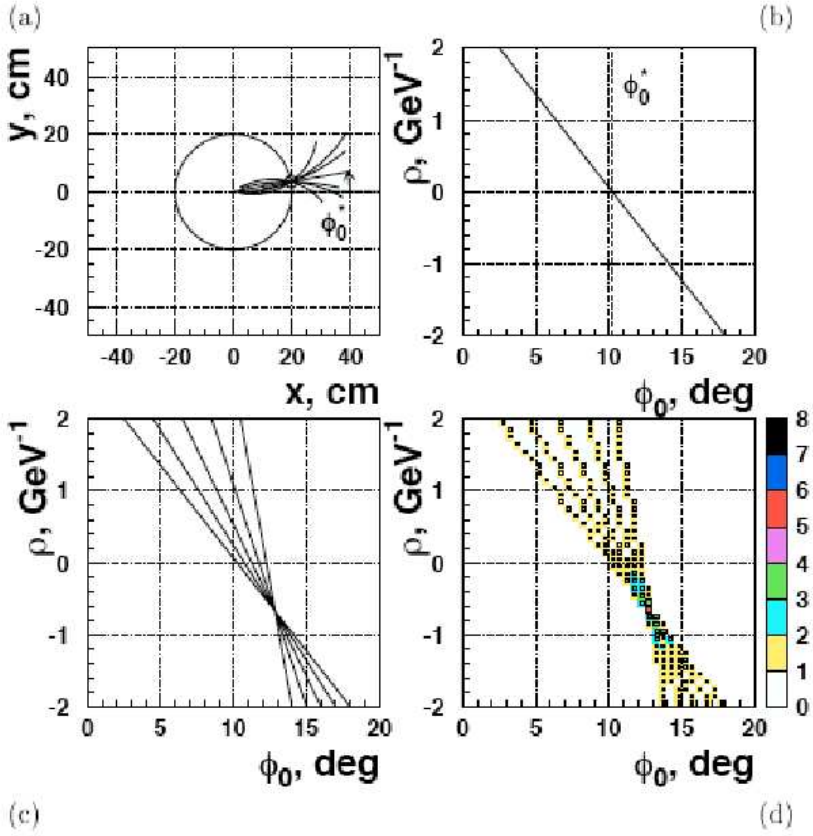

Figure 5.4: Principle of the HTF algorithm. (a) A hit in the tracking detectors is crossed by a family of trajectories that intersect the origin. (b) This family is represented by a line in the (ρ, ϕ) parameter space. (c) For hits on the same track, the lines intersect at a point representing the track parameters. (d) The algorithm creates a (ρ, ϕ) histogram, and for each hit the corresponding cells are incremented. A track may be identified by a peak in the histogram.

GTR using the Kalman fit algorithm [48]. Starting from an approximate set of track parameters, each hit is added in turn by propagating the track to the next detector surface, where the location of the hit is used to update the track parameters and their covariance matrix. The tracks are propagated through the detector by the DØ interacting propagator [49], which models the particle motion in the magnetic field as well as the effects of energy loss and multiple scattering in the detector material. At each stage, the χ^2 of the track fit is defined as the value for the track using the current set of hits, plus an incremental χ^2 that is added by including the new hit. Requiring this χ^2 to be a minimum allows derivation of the updated track parameters and their covariance matrix without a need for iterative refinement. The updated values are the optimal fit values for the set of measurements they are based on.

5.3 Primary Vertex Reconstruction

Following the completion of the track reconstruction, DØRECO runs an algorithm to reconstruct the primary vertices in the event [50]. Tracks with at least two SMT hits and p_T greater than 0.5 GeV/c are included in the vertex fitting. The algorithm first runs to find seed vertices, using tracks selected by a loose cut on their impact parameter with respect to the z-axis. The algorithm runs a second time to fit the final vertices, this time using tracks which have an impact parameter significance of less than 5 with respect to one of the seed vertices. The vertex position is calculated using the impact parameters technique [51], with the χ^2 per degree of freedom of the fit required to be less than 10. If the χ^2 is above this limit, tracks giving the largest contribution are removed until a satisfactory value is reached. The positions of the primary vertices in a single data taking run (typically lasting 2 to 4 hours) are averaged to estimate the position of the beamspot during the run, since the beam position is not constant.

In many b-physics studies the primary vertex positions used in the analysis are calculated later using an alternative method, which uses the position of the beamspot as an additional constraint. The analysis that follows also uses this technique, which is described in section 6.1.1.

5.4 Muon Reconstruction

The muon reconstruction process aims to identify muons among the central tracks. First the drift tube and muon scintillator hits are used to reconstruct tracks within the muon system, which are known as *local* muons. Extrapolation of trajectories through the detector then allows central tracks to be matched with local muons to create *global* muons.

5.4.1 Local Muon Reconstruction

The reconstruction of local muons begins with the association of wire hits to build straight track segments within each of the three layers of the muon system. Matching of segments between layers is then performed, and the trajectory through the toroid is fitted to extract an estimate of the muon momentum.

Segment Reconstruction

A linked list algorithm [52] is used to find the track segments. The timing information from the PDTs and MDTs is used to calculate the electron drift distance for each wire registering a hit. This allows drift circles to be plotted around the wires, as shown in Figure 5.5. A hit candidate is assigned at each point where a drift circle intersects a wire plane, hence two hit candidates are associated with each wire hit. The algorithm then assigns straight link segments between pairs of hit candidates that fulfil certain criteria. The hits in a pair must lie in different wire planes, unless they are nearest neighbours from two adjacent wires. Their

distance of separation along the wire planes must be less than 20 cm. The algorithm then recursively attempts to match each link segment with all others that follow it, creating a new longer link when the hits from the two links are consistent with a straight line. All of the resulting segments are fitted in two dimensions. The segments are then sorted according to the number of hits, with the χ^2 of the fit used to order those with equal numbers of hits. The best four segments in each region are kept, and are extrapolated to the scintillator layers. Scintillator hits that are consistent with the track segments are matched. In the forward region the track is refitted after assigning a scintillator hit. Since the MDTs do not give a measurement of the position of the hit along the wire, the resolution of the drift time is degraded by the unknown time for the signal to reach the readout electronics. An associated scintillator hit gives a measurement of this coordinate so the drift time measurements may be improved. The segment is refitted using the improved information. Finally the algorithm attempts to find matches between the remaining B and C layer segments. Since there is no magnetic field in or between the two layers, each B layer segment is extrapolated along a straight trajectory to the C layer, and a C layer segment within the expected window is matched. The new segment is refitted using both sets of hits. Any unmatched segments are retained as muon candidates. A final filtering then selects the segments with the lowest χ^2 values in each region of the muon system.

Track Fitting

A set of algorithms is then used to associate A layer segments with those in either or both of the B and C layers, and to fit the trajectory through the toroid [53]. Segment pairs are formed from an A layer segment and a BC layer segment in the same or adjacent octants of the muon system. The pairs are filtered using a set of cuts. These require that the A segment direction is consistent with the z position of the primary vertex, and that the relative positions and

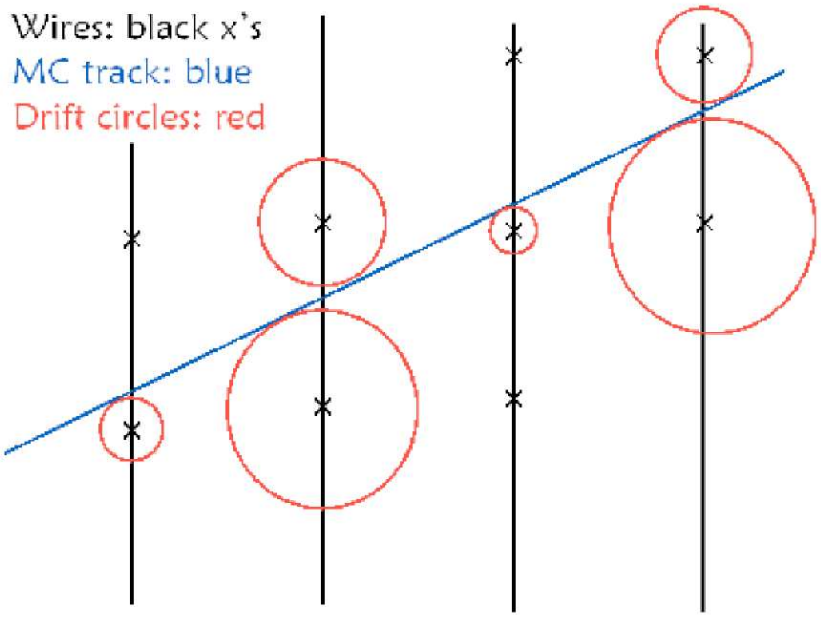

Figure 5.5: Muon segment reconstruction. A track traversing the drift tubes leads to hits being registered in several wires. The timing information is used to plot drift circles around each wire. A hit candidate is assigned at each point where a drift circle intersects a wire plane.

directions of the segments are within expected ranges. The deviation angle is used to calculate a first estimate of the momentum, and a minimum cut is applied. For each pair selected, the trajectory through the toroid is fitted by an algorithm which estimates the energy loss as a function of momentum and accounts for multiple scattering in the material. The fit gives an improved measurement of the momentum and determines the muon track parameters and their error matrix.

5.4.2 Central Track Matching

In the final stage of muon reconstruction, local muon tracks or segments are matched with tracks in the central tracking system. If the local muon has a fitted track through the toroid, then the track parameters and their error matrix are propagated back to the point of closest approach to the beam [54]. These parameters and those of any potentially matching central track are weighted to compute combined parameters and their error matrix. The χ^2 of the match is used as a criterion for acceptance. If only an A or BC segment is present, or if the local fit fails to converge, then central tracks are extrapolated to the muon system [55] and spatial matching is performed. In this case the parameters of the central track are assigned. Matched or unmatched muons may be used in physics analysis if practicable. Reconstructed muons are described by a variety of types [56], which refer to location of segments in the muon system (A layer, BC layer or both) and whether or not a central track has been matched.

5.5 Event Simulation

Simulation of events is used in the analysis to estimate certain properties of the signal and background events. A full simulation of the interaction and the detector response is performed. The following sections outline the processes involved in producing simulated data samples.

5.5.1 Event Generation

The simulation of the hard scatter and resulting interactions is performed by one of several *event generator* programs. These use theoretical knowledge and Monte Carlo techniques to generate the different processes in an event. All samples used in the analysis were produced by Pythia [57], which is one of the most commonly used generators. Pythia uses leading order predictions in perturbation theory to model the hard scatter of two partons, which are picked out of the proton and antiproton by referring to parton distribution functions (PDFs). The accumulation of the resulting quarks into hadrons is performed using a non-perturbative model. The decays of unstable particles are also computed by Pythia. However, in the case of b-hadrons, Pythia is usually prevented from performing the decay and this task is instead implemented by the EvtGen [58] package. EvtGen is a specialised package developed for modelling b-hadron decays, and it contains a number of detailed models for simulating the various types of decay. Specified particles may be forced by EvtGen to decay via the desired route, increasing the generation efficiency.

The events containing decays of interest are selected at the generation stage and passed on to the detector simulation packages. The selection is usually performed by a package known as DØ_MESS (DØ Monte Carlo Event Selection System) [59], which allows selection of events by a series of cuts. Cuts may require the presence of specified particles, which may also be required to originate from a specified parent particle. Cuts may also be applied to the transverse momentum and pseudorapidity of each particle. A more sophisticated selector, known as bselect [60], has since been developed for use with b-physics samples. This allows more complicated selections such as cuts on collections of particles or the selection of an inclusive final state from any B meson decay.

5.5.2 Detector Simulation

The response of the DØ detector to each selected event is then modelled. The first stage involves modelling the interactions of particles with the material of the detector, and computing the energy deposited. This is performed by a package known as DØGSTAR [61] (DØ GEANT Simulation of the Total Apparatus Response), an implementation of the CERN GEANT [62] package. DØGSTAR contains a model of the DØ detector built from many smaller volumes of specified materials, through which the generated particles are propagated. Secondly, a package called DØSIM [63] performs modelling of the detector electronics to include the effects of readout in the simulation. These include the effects of detector noise, inefficiencies and digitisation of the data. The package also simulates the effects of 'pile-up', caused by additional interactions occurring within the same bunch crossing as the hard scatter.

The output from DØSIM is finally passed to DØRECO for reconstruction using the same methods as used for data. The output is identical to real data except that the thumbnail also contains the generated Monte Carlo information, in order to allow comparison of reconstructed and generated objects.

Chapter 6

Selection of Semileptonic Λ_b^0 Decays

In this chapter, the initial stages of the analysis are described. These involve reconstruction and selection of semileptonic Λ_b^0 decays, and techniques to reduce the high level of background that is also reconstructed. Since the resulting sample of events will be used to measure the lifetime, the main requirement of the selections is that they do not modify the lifetime distribution. The decay used is $\Lambda_b^0 \to \Lambda_c^+ \mu^- \bar{\nu}_\mu X$,[1] and the Λ_c^+ is reconstructed using its decay $\Lambda_c^+ \to K_S^0 p$. This decay of the Λ_c^+ is relatively simple to reconstruct at DØ since the K_S^0 can easily be identified by its decay to two oppositely charged pions. However, there is still a large combinatoric background, and the following sections describe techniques to reduce this background while using selections that do not bias the lifetime distribution in the selected sample.

[1] Charge conjugates are implied throughout.

6.1 The BANA Package

The analysis is performed using the BANA package [64], that is used for many b-physics analyses at DØ. The package can be used with the thumbnail format of data, but most often is used with a format known as AADST. This analysis uses data in the AADST format, which has been converted from the thumbnail format and stored on disk. This format is simpler than the thumbnail since it contains only tracking and muon information, which is all that is required for most b-physics analyses. This means that the size of the stored events is smaller and they can be stored on disk, allowing relatively easy access. This allows analyses to be developed more quickly than the standard methods used at DØ. The BANA package accesses the information in the AADST data, and provides a number of methods for reconstructing decays and calculating parameters that are needed for analyses. It provides classes for particles and vertices, allows the calculations of vertices and impact parameters and their errors and allows calculation of the invariant masses from the decay products, as well as the constraining of masses of particles. Also provided are methods to search for commonly used particles such as J/ψ, K^0_S and Λ^0.

6.1.1 Vertexing

The primary vertices are reconstructed by a method based on that used by the DELPHI collaboration for tagging b-hadrons [45, 46]. This uses the stored beam spot position for the run to provide an additional constraint on the vertex location. The position of the beamspot in the (x, y) plane is parametrised as a function of z, since the beams have a small tilt angle with respect to the detector axis, and the primary interactions occur over a large range of z. The parametrisation is obtained by measuring the positions of 1000 primary vertices in each run and performing a fit to the distribution. The size of the beamspot in the transverse plane is

approximately 30 μm, and including it in the vertex fit improves the resolution of the primary vertex in the (x, y) plane to around 20 - 25 μm, compared to around 30 - 60 μm without the beamspot constraint. The χ^2 for the vertex is given by,

$$\chi^2(\vec{V}) = \sum_a \sum_{\alpha,\beta=1,2} d^a_\alpha (S^{-1}_a)_{\alpha\beta} d^a_\beta + \sum_i \frac{(V^{sp}_i - V_i)^2}{(\sigma^{sp}_i)^2}, \tag{6.1}$$

where (d^a_1, d^a_2) is the vector containing the axial and stereo impact parameter for each track, and S_a is the covariance matrix of the impact parameter components with respect to the origin. V^{sp}_i and σ^{sp}_i give the coordinates of the beamspot in x and y and its size. The use of the axial and stereo components of the impact parameter means each track contributes two degrees of freedom to the fit. After the χ^2 value has been calculated using the initial sample of N_{tr} tracks, each track is removed one at a time, and the χ^2 with $N_{tr} - 1$ tracks is calculated for N_{tr} combinations. The track causing the largest change in χ^2 is removed if the change is larger than a value $\Delta_{max} = 9$. This process is repeated until no more tracks are removed from the vertex.

The positions of reconstructed secondary vertices are found by minimisation of the first term of the χ^2 function in (6.1), with the term for the beamspot constraint excluded.

6.2 Data Sample and Triggers

The analysis uses the full sample of data collected in Run IIa of the Tevatron, between April 2002 and March 2006. This corresponds to an integrated luminosity of approximately 1.3 fb^{-1}. The data used were taken from a sample stored on disk in AADST format that consisted of events that passed an inclusive single muon skim [65]. The skim was performed by the b-physics group to facilitate the selection of subsamples for many analyses. The events containing a single muon

correspond to about 30% of the total events. The requirements of this skim were:

- Muon track segments in the B-C layer or both the A and B-C layers;
- A matched central track;
- $p_T(\mu) > 1.5$ GeV/c;
- Convergence of the local muon fit;
- Track has greater that 1 SMT hit and greater than 1 CFT hit.

The first selection that must be performed on the data is on the triggers. A set of triggers was implemented in recent trigger lists which require tracks with significant impact parameters to be reconstructed. Since particles created further from the primary vertex will have larger impact parameters, the lifetime distributions in these events are biased, and hence these events must first be removed. This was done using a list of triggers that do not bias the lifetime distribution, with those requiring impact parameters removed [66]. Any event firing one of these triggers was accepted. In this way an event that fires a biased trigger as well as an unbiased one is kept.

6.3 Decay Reconstruction

Events that satisfied the above requirements were searched for the decays of interest. The primary vertex for the event was fitted using the method described in section 6.1.1, and the central tracks were clustered into jets. Since the events of interest generally contain relatively low p_T jets, which will not be efficiently reconstructed by the calorimeter, only the charged tracks observed in the central tracking system were used to reconstruct the jets. In high p_T physics, a combination of tracking and calorimeter information is generally used. The jet

reconstruction was performed using the DURHAM clustering algorithm [67]. This performs the clustering by calculating the scaled transverse momentum,

$$y_{kl} = 2(1 - \cos\theta_{kl})\min(E_k^2, E_l^2)/s, \tag{6.2}$$

for every pair of particles (k, l), which have energies E_k and E_l and lie at a relative angle θ_{kl}. s denotes the centre-of-mass energy squared. The pair with the smallest value of y_{kl} are then combined to form a new 'pseudoparticle', and the pairing process is then repeated with the remaining particles and pseudoparticles until all remaining pairs have y_{kl} larger than a cutoff value, y_{cut}. The clusters of particles remaining at this point are defined as the jets. In this case the cutoff parameter, y_{cut}, is set to 15 GeV/c. The decay products were then searched for, and the secondary vertices in the decay chain were reconstructed.

6.3.1 Muon Selection

Selection of muons of a reasonable quality had already been applied in the single muon skim, so there were few additional requirements imposed at the analysis stage. The cut on p_T of the muon was tightened to $p_T > 2.0$ GeV/c for higher rejection of muons from other decays.

6.3.2 K_S^0 Selection

The jet containing a selected muon was searched for K_S^0 candidates. The K_S^0 has a branching fraction of approximately 69% for decay to a $\pi^+\pi^-$ pair, and a mean lifetime of approximately 0.89×10^{-10} s [2], so is likely to fly several centimetres from its production vertex before decaying. Therefore a K_S^0 can be identified by two oppositely charged tracks originating from a secondary vertex at large displacement from the primary vertex. The invariant mass of the decaying

particle can be calculated for the assumption that both tracks are pions, and plotting these masses should reveal a peak due to K^0_S. A sample can then be selected using an appropriate mass window around the peak. The tool for finding K^0_S and Λ^0 particles provided by the BANA package was used for the selection. It sets a number of criteria in order to reduce background.

K^0_S and Λ^0 secondary vertices are required to pass a quality cut of χ^2 of less than 25 to reduce fake vertices caused by random track coincidences. The vertex is required to lie at a large or significant distance from the primary vertex. This is done by calculating the distance to the reconstructed primary vertex, d_{V^0}, and the error on this distance, $\sigma(d_{V^0})$, and requiring that d_{V^0} be greater than 0.5cm or be at least $4\sigma(d_{V^0})$. Since the tracks should originate from this secondary vertex, the two tracks forming the vertex may collectively have a maximum of two associated hits before the vertex.

Further selections were then applied to the tracks and reconstructed vertex. Any vertices containing the identified muon as one of the tracks were rejected and both tracks were required to have at least one hit in the CFT, since the two pions produced are stable particles and normally should cross the entire detector. The particle reconstructed was required to have p_T of at least 0.7 GeV/c.

To select K^0_S the two tracks were assumed to be $\pi^+\pi^-$ and their invariant mass was calculated. An invariant mass plot for a small data sample is shown in Figure 6.1. The signal is fitted with a Gaussian, and this gives a central mass of 494.2 ± 0.2 MeV/c^2. Mass peaks observed at DØ are generally not consistent with the PDG values, due to momentum calibration uncertainties, and this is true in this case, since the PDG gives a mass of 497.648 ± 0.022 MeV/c^2 for the K^0 [2]. Candidates with invariant mass within the range 480.0 MeV/c^2 – 507.5 MeV/c^2 were accepted as K^0_S. These limits both correspond to approximately $1.8\sigma_{K_S}$ from the centre of the mass peak, where σ_{K_S} is the fitted width. The masses of the candidates within the accepted window were constrained to the PDG value, and

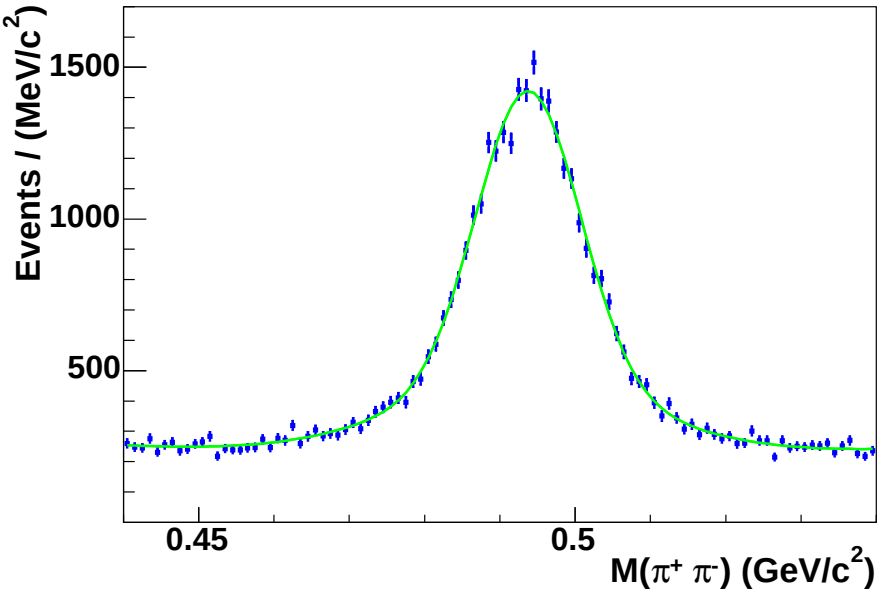

Figure 6.1: The $\pi^+\pi^-$ invariant mass for a small sample of $K^0_S \to \pi^+\pi^-$ candidates. The fitted peak lies at a central mass of 494.2 ± 0.2 MeV/c^2.

the magnitudes of the momenta of the pions were adjusted accordingly. This will allow a more precise reconstruction of the Λ_c^+ mass.

The invariant mass was also calculated for the case where one of the two tracks was assumed to be a proton and the other a pion, in both possible permutations. In the corresponding invariant mass plot a peak is observed close to 1.115 GeV/c^2 due to the decay $\Lambda^0 \to p\pi^-$. If this decay is reconstructed but is assumed to be $K^0_S \to \pi^+\pi^-$ some of the events will have $M(\pi^+\pi^-)$ within the window used to select K^0_S candidates, and will increase the background. Therefore those K^0_S candidates for which $M(p\pi^-)$ or $M(\pi^- p)$ lies between 1.109 GeV/c^2 and 1.120 GeV/c^2 were rejected, since this range encompasses most of the observed Λ^0 mass peak. This reduces the size of the K^0_S sample by approximately 4%.

6.3.3 Λ_c^+ and Λ_b^0 Reconstruction

For each reconstructed K^0_S candidate, the remaining tracks in the jet were searched for proton candidates. Each track with $p_T > 1.0$ GeV/c and at least 2 hits in the

silicon detector was assumed to be a proton candidate. Each proton candidate was vertexed with the reconstructed K^0_S candidate. The reconstructed vertex was required to have a value of χ^2 less than 9. The K^0_S and proton candidates were combined to form a Λ_c^+ candidate. This was then required to form a vertex with the muon, also with χ^2 less than 9.

6.4 Signal Optimisation Cuts

The requirements on the transverse momenta and quality of the decay products and vertices remove much combinatorial background, but to establish a significant signal further selection criteria must be applied. Some of the cuts described below were first used together with lifetime biasing cuts on the angle and impact parameter of the Λ_c^+ candidate, in order to obtain a signal in a subsample of the data [68]. The values of those cuts were varied individually to find the values that optimised the signal significance:

$$significance = \frac{N_s}{\sigma(N_s)} = \frac{N_s}{\sqrt{N_s + N_b}}, \tag{6.3}$$

where N_s and N_b are the numbers of signal and background events respectively. The same values of those cuts are used here, but the lifetime biasing cuts have been removed. Additional cuts on the isolation of the Λ_b^0 candidate and the Λ_c^+ transverse momentum were subsequently added.

Λ_c^+ Flight Distance

The Λ_c^+ has a proper decay length of $c\tau = 59.9\mu$m [2]. This is relatively short compared to most weakly decaying particles, so cutting on the flight distance of the Λ_c^+ removes background very effectively. The transverse distance, d_T^{bc}, between

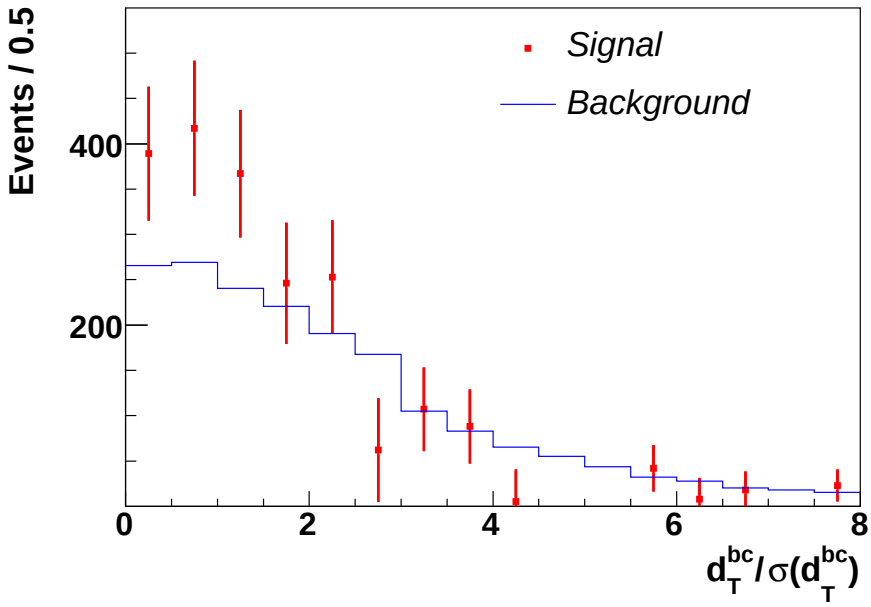

Figure 6.2: Estimated distributions of $d_T^{bc}/\sigma(d_T^{bc})$ for signal and background events.

the Λ_b^0 decay vertex and the Λ_c^+ decay vertex and its uncertainty, $\sigma(d_T^{bc})$, were calculated. A cut on the significance of the measured distance was then applied. Requiring that $d_T^{bc} < 3.3\sigma(d_T^{bc})$ was found to give a good rejection of background. The distributions of this variable for signal and background events were estimated with the lifetime biasing cuts applied. Sidebands were used to estimate the background distribution, while the signal distribution was estimated by obtaining the distribution for the signal region and subtracting the background distribution. The distributions, shown in Figure 6.2, illustrate the effectiveness of this cut in removing background.

Vertex Distance Difference

Since the distance between the Λ_b^0 and Λ_c^+ vertices is small, its measured value is often consistent with zero, and the resolution effects sometimes cause the Λ_c^+ decay vertex to be reconstructed closer to the primary vertex than the Λ_b^0 decay vertex. Therefore the Λ_c^+ decay vertex is allowed to be closer to the primary ver-

tex, but if the difference is significant the event is likely to be background and so is rejected. The transverse distance, d_T^b, of the Λ_b^0 decay vertex from the primary vertex and the corresponding distance for the Λ_c^+ decay vertex, d_T^c, were calculated and the significance of the difference, $(d_T^c - d_T^b)/\sigma(d_T^c - d_T^b)$, was determined. The value of this quantity was required to be larger than -3, so background in which the Λ_c^+ vertex is significantly closer to the primary vertex is rejected.

$\Lambda_c^+\mu^-$ Invariant Mass

The Λ_b^0 candidate was partially reconstructed using the Λ_c^+ candidate and the muon, and the invariant mass was calculated. Since a neutrino is missing an upper bound can be placed below the value of the Λ_b^0 mass of 5.624 GeV/c^2 [2]. An upper limit was placed at 5.4 GeV/c^2, and a lower limit at 3.4 GeV/c^2. The distributions for signal and background events are shown in Figure 6.3, which shows that these limits remove significant background while retaining a high proportion of the signal.

Relative Muon Transverse Momentum

Some background is also rejected by applying a cut on the p_T of the muon with respect to the direction of the Λ_c^+, known as p_{Trel}. This was required to be greater than 0.35 GeV/c.

Λ_c^+ Transverse Momentum

A cut on the Λ_c^+ transverse momentum of $p_T(\Lambda_c^+) > 2.0$ GeV/c^2 was applied since the Λ_c^+ is expected to have higher momentum and no signal is seen with $p_T(\Lambda_c^+)$ below this value. Since this variable is used in the likelihood ratio selection described in the next section, the value of this cut is chosen to remove a region of negligible signal, as shown in Figure 6.4, and is not optimised for signal significance.

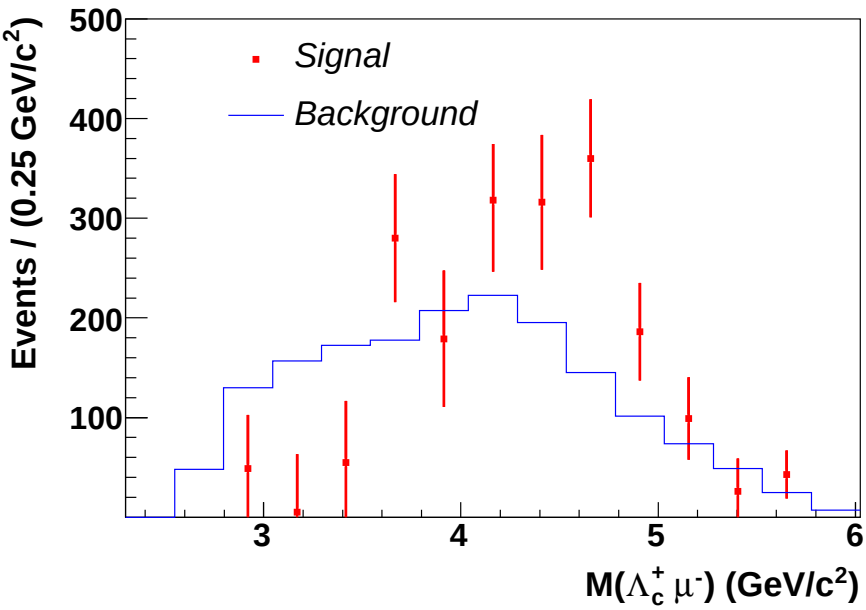

Figure 6.3: Estimated distributions of $\Lambda_c^+\mu^-$ invariant mass for signal and background events.

Isolation

A b-hadron takes a large proportion of the momentum within a b-jet, whereas this is not the case for combinatoric background. To use this to improve the signal, the quantity known as isolation is defined. A cone of $\sqrt{(\Delta\phi)^2 + (\Delta\eta)^2} < 0.5$ is defined around the momentum of the $\Lambda_c^+\mu^-$ system. The isolation is defined as the fraction of the total momentum within the cone carried by Λ_b^0 candidate. To reduce background this was required to be greater than 0.5. This variable is also used in the likelihood ratio method so it is not optimised for significance. However, as shown in figure 6.5, it removes a significant fraction of background while removing a negligible fraction of the signal.

The $K_S^0 p$ invariant mass plot for $\Lambda_c^+\mu^-$ pairs selected using this set of cuts is shown in Figure 6.6. The distribution is fitted with a signal Gaussian and a fourth order polynomial background. The fit gives a signal of 5465 ± 609 signal events,

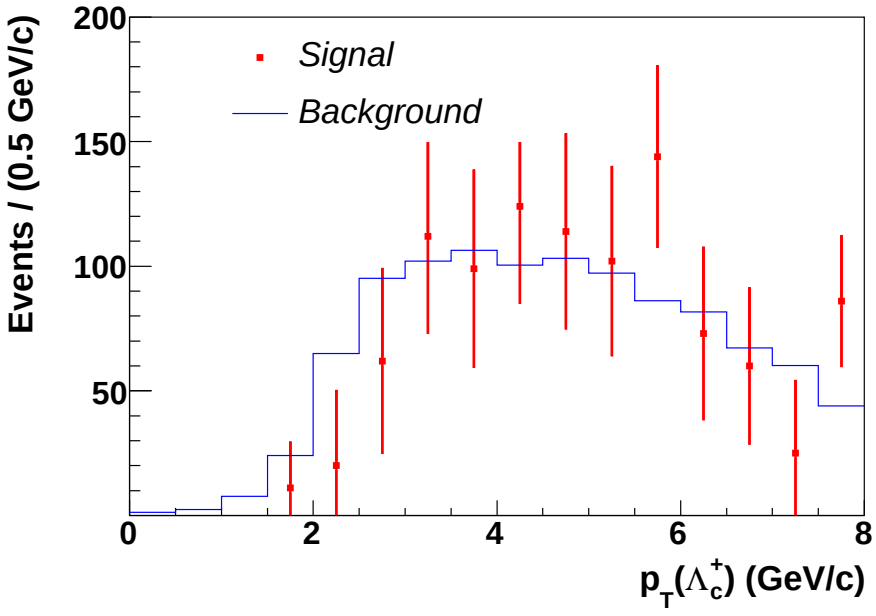

Figure 6.4: Estimated distributions of Λ_c^+ transverse momentum for signal and background events.

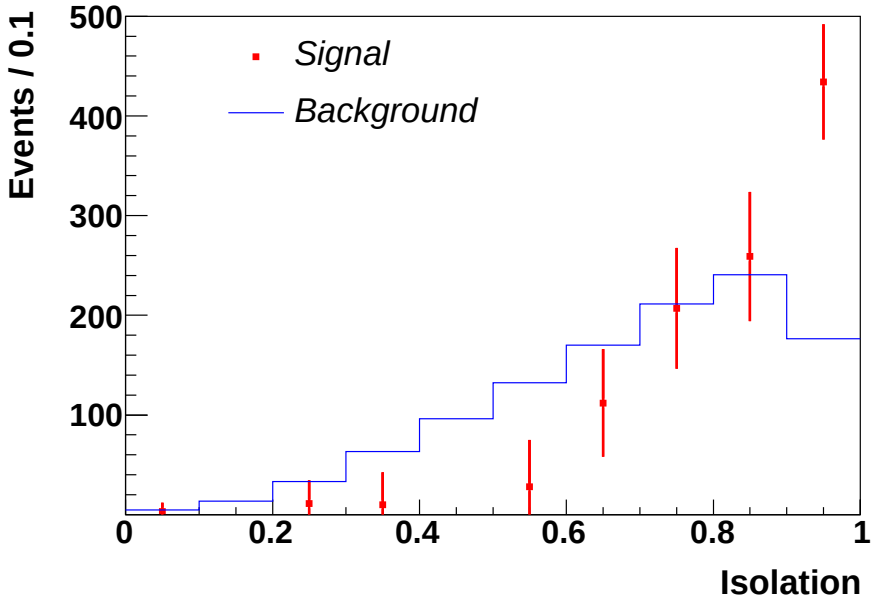

Figure 6.5: Estimated distributions of $\Lambda_c^+\mu^-$ isolation for signal and background events.

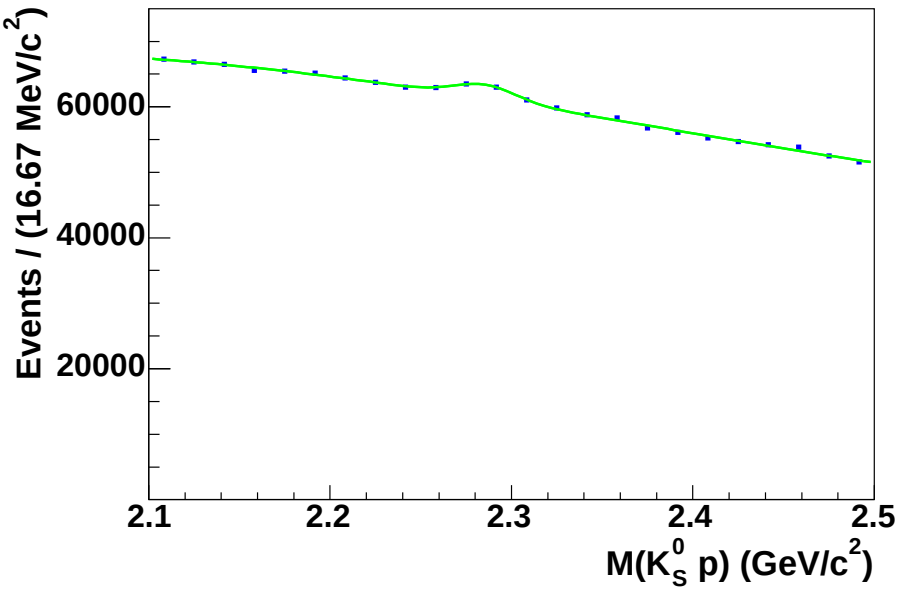

Figure 6.6: The $K^0_S p$ invariant mass for Λ^0_b candidates selected using the criteria described in section 6.4. A signal of 5465 ± 609 events is fitted, at a central mass of 2285.80 ± 2.0 MeV/c^2. The mass peak has a width of 17.02 ± 2.46 MeV/c^2.

at a mass of 2285.80 ± 2.0 MeV/c^2, and with a width of 17.02 ± 2.46 MeV/c^2. The signal has a significance of approximately 10.2. The background is still very high, however, so a likelihood ratio method was used to further improve the signal significance.

6.5 Likelihood Ratio Selection

The likelihood ratio selection [69] is a technique that has been used in other studies at DØ [70], where it has successfully reduced background levels. A number of discriminating variables are combined to give an overall measure of how likely an event is to be signal or background. A cut on this combined variable is then applied.

6.5.1 Method

A set of discriminating variables $x_1, ..., x_n$ is defined. For each of the variables, x_i, a pair of probability distributions is defined, one for signal events, $f_i^s(x_i)$, and another for background events, $f_i^b(x_i)$. A combined variable y is defined as follows:

$$y = \prod_{i=1}^{n} y_i, \tag{6.4}$$

where

$$y_i = \frac{f_i^b(x_i)}{f_i^s(x_i)}. \tag{6.5}$$

The two distributions for each of the variables are estimated, and the ratio, y_i, is parametrised, so for each event the combined variable y may be estimated using the parametrisation. If the variables $x_1, ..., x_n$ are independent then this method gives the optimal tagging of signal events [69]. A cut is applied to y to optimise the signal significance.

6.5.2 Estimation of Distributions

A method for estimating $f_i^s(x_i)$ and $f_i^b(x_i)$ is required, and in this case they are estimated from the data, using B meson decays that are kinematically similar to the Λ_b^0 signal decays. The decays of $\bar{B}^0 \to D^+\mu^-\bar{\nu}_\mu X(D^+ \to K_S^0\pi^+)$ and $\bar{B}_s^0 \to D_s^+\mu^-\bar{\nu}_\mu X(D_s^+ \to K_S^0K^+)$ are allowed into the sample when the proton candidate is in fact the pion or kaon from either of these decays. When the $K_S^0\pi^+$ or $K_S^0K^+$ invariant mass is plotted a single peak is observed, as is shown in Figure 6.7 and Figure 6.8 for a subsample of the data, using a modified selection. As shown in section 6.6, when kaons from the decays of D_s^+ are incorrectly identified as pions from D^+ decays, or vice versa, the invariant mass peak for the wrongly

identified events lies very close to that of events which are correctly identified. There is substantial overlap between the two peaks in either the $K^0_S\pi^+$ or $K^0_SK^+$ invariant mass plot, so only one peak is seen in data. The similarity between the kinematics of these decays and the Λ^0_b signal decay allows these decays to be used to estimate the probability distributions. A cut of $D_{xy} > 2\sigma(D_{xy})$ was applied in order to obtain the signal shown in in Figure 6.7 and Figure 6.8, where D_{xy} is the signed distance between the primary vertex and the b-hadron decay vertex. If $\vec{X}$ is the vector which points from the primary vertex to the decay vertex, then the sign of D_{xy} is defined by the sign of $\vec{X} \cdot \vec{p}_T(\Lambda^+_c\mu^-)$. This cut was not used when selecting events for the lifetime measurement. The cut $d^{bc}_T < 3.3\sigma(d^{bc}_T)$ was also removed, since this reduces the signal significance in these channels due to the longer lifetime of the D^+ and D^+_s. The cut on $(d^c_T - d^b_T)/\sigma(d^c_T - d^b_T)$ was changed to require the value to be greater than zero, since this gave an increase in signal significance for these channels. Using these selections a yield of 3109 ± 169 $D^+\mu^-$ and $D^+_s\mu^-$ candidates is obtained from the fit to Figure 6.7, which contains events selected from approximately 60% of the full data sample.

Using the signal shown, the probability distributions were obtained by defining a signal region and sideband regions as follows:

- $S : 1.82 < M(K^0_S\pi^+) < 1.91$ GeV/c^2;
- $B_1 : 1.70 < M(K^0_S\pi^+) < 1.745$ GeV/c^2;
- $B_2 : 1.985 < M(K^0_S\pi^+) < 2.03$ GeV/c^2.

The distribution of each variable for background events, $f^b_i(x_i)$, was obtained using events in the two sidebands, B_1 and B_2. To obtain the distribution for signal events, $f^s_i(x_i)$, the distribution of $f^b_i(x_i)$ was subtracted from the corresponding distribution obtained for events in the S region. The distributions were normalised and the distributions of the ratios y_i were obtained. Polynomial functions were then used to parametrise the y_i distributions.

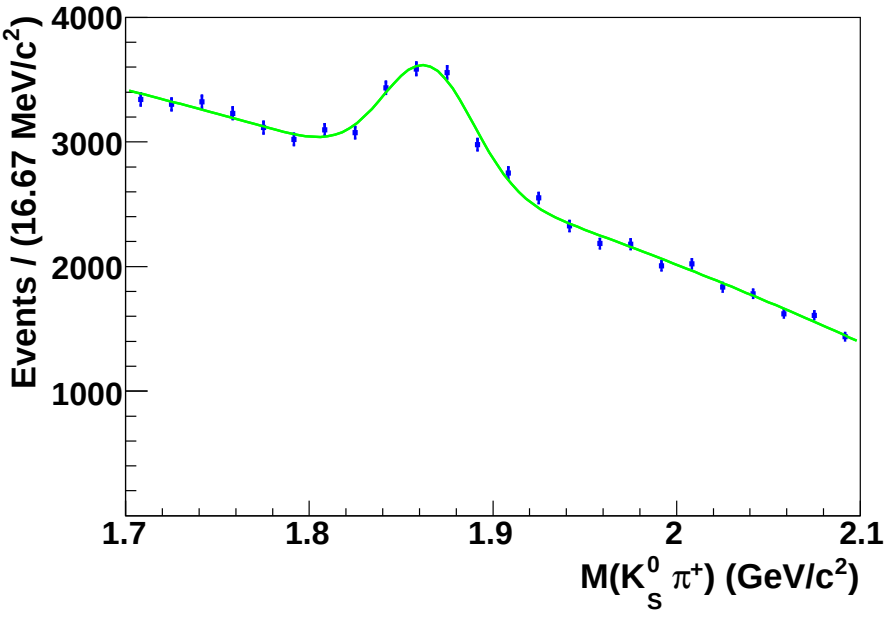

Figure 6.7: The $K^0_S\pi^+$ invariant mass for the sample selected for the likelihood ratio method by the criteria described in section 6.5.2.

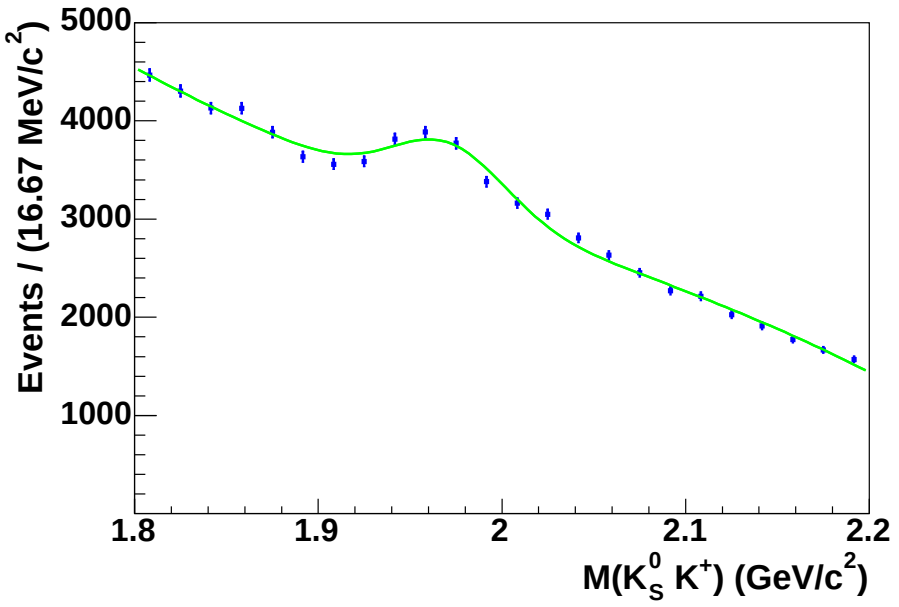

Figure 6.8: The $K^0_SK^+$ invariant mass for the sample selected for the likelihood ratio method by the criteria described in section 6.5.2.

6.5.3 Selection of Variables

The discriminating variables chosen for use in the final selection of events for the lifetime measurement are:

- Isolation, defined as above;
- $p_T(K^0_S)$;
- $p_T(p/\pi^+)$;
- $p_T(\Lambda^+_c/D^+)$;
- $M(\mu^- + \Lambda^+_c/D^+)$.

The estimated $f^s_i(x_i)$ and $f^b_i(x_i)$ distributions for each variable are shown in Figure 6.9. In Figure 6.10 it is shown how the ratios, y_i, are parametrised.

In taking the ratio, any bins in which no signal was observed had their value of y_i set to a maximum value of 3, since this is larger than any other value for the variables for which this occurred. Other variables were initially included, but were later dropped since they caused no observed improvement of the selection. These were the invariant mass of the original K^0_S candidate, the decay length of the K^0_S candidate and the χ^2 values for the Λ^0_b/B^0 and Λ^+_c/D^+ decay vertices. Subsequent Monte Carlo studies of the Λ^0_b and $\bar{B}^0$ decays suggest that the agreement between the distributions of the chosen variables is good in most cases. The distributions of the variables for the two samples are shown in Figure 6.11.

6.5.4 Final Selection

The distributions of $\ln(y)$, for signal and background events were estimated using the same method used to estimate $f^s_i(x_i)$ and $f^b_i(x_i)$, and are shown in Figure 6.12. A cut on the value of $\ln(y)$ was applied, and varied around the region where the signal and background distributions intersect. The resulting significance of the

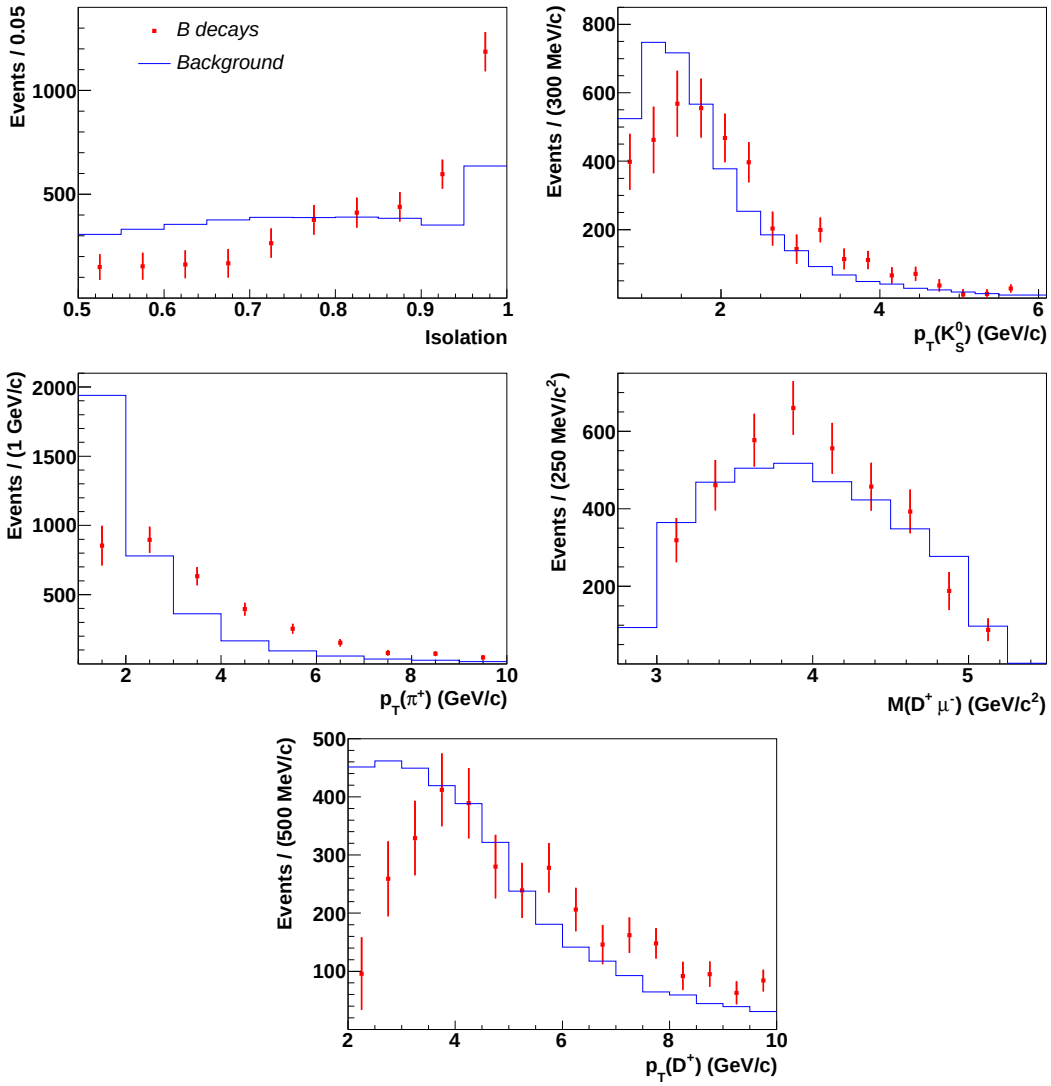

Figure 6.9: Distributions of the discriminating variables used in the likelihood ratio method for B meson decays and for background events.

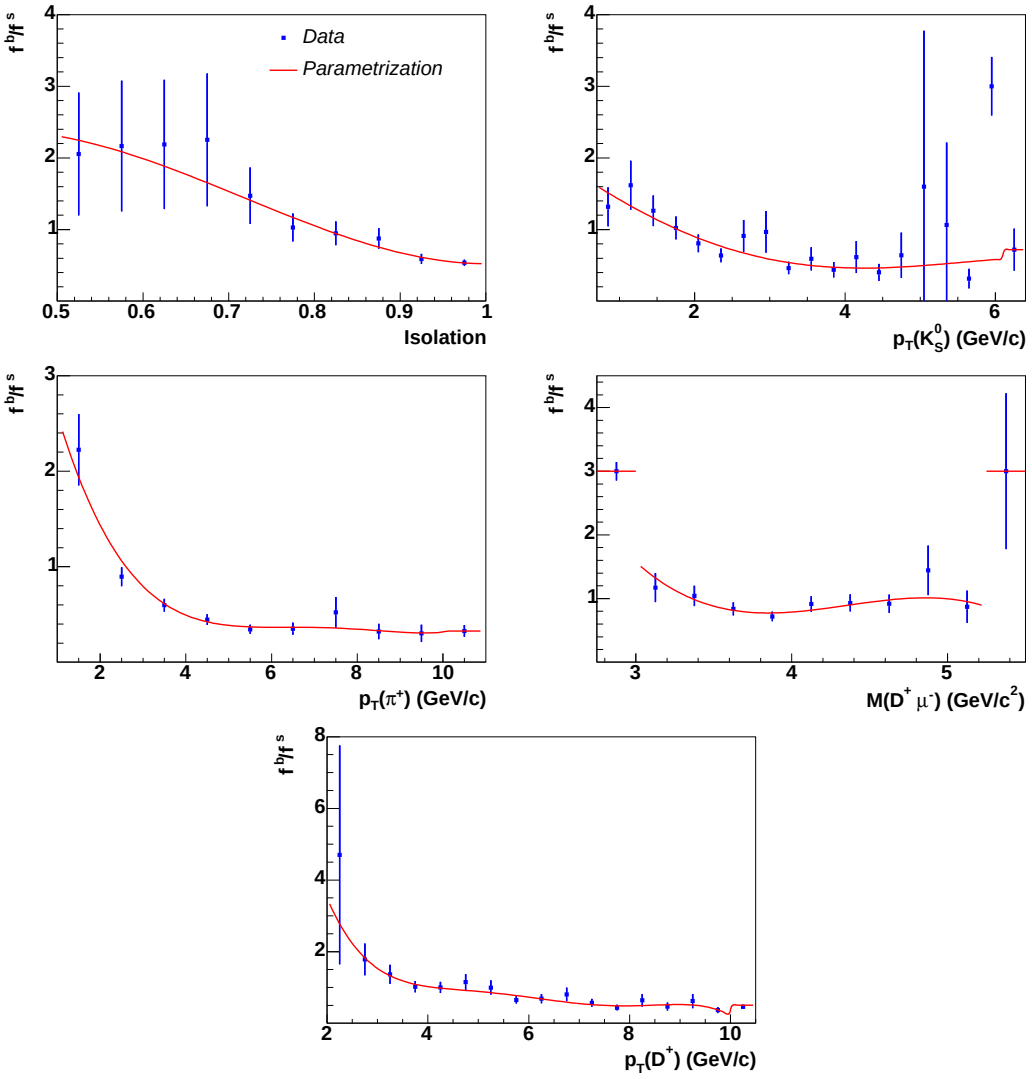

Figure 6.10: Likelihood ratios, y_i, for each of the discriminating variables, estimated using the distributions in Figure 6.9, also showing the parametrisation of each distribution.

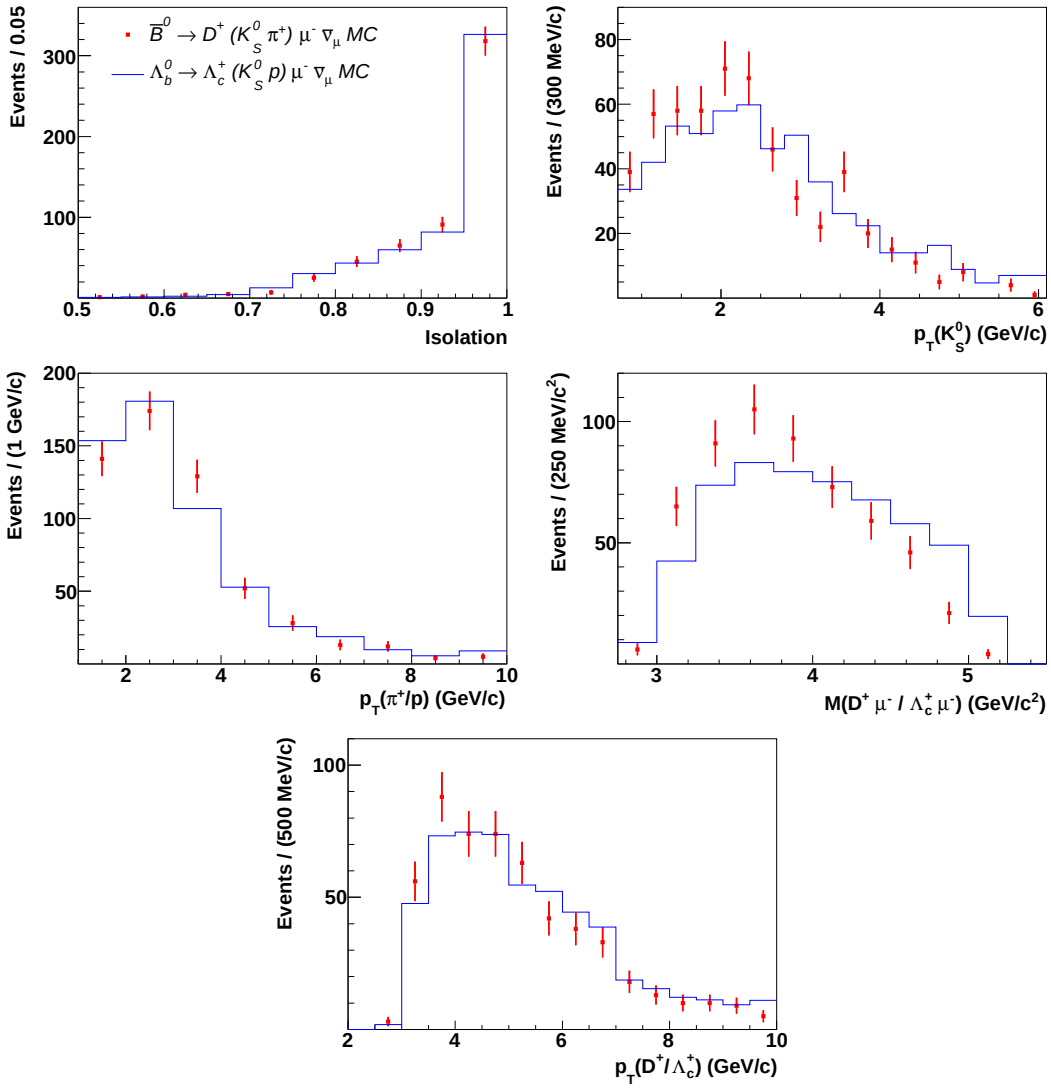

Figure 6.11: Distributions of the discriminating variables for Λ_b^0 and B meson decays in Monte Carlo.

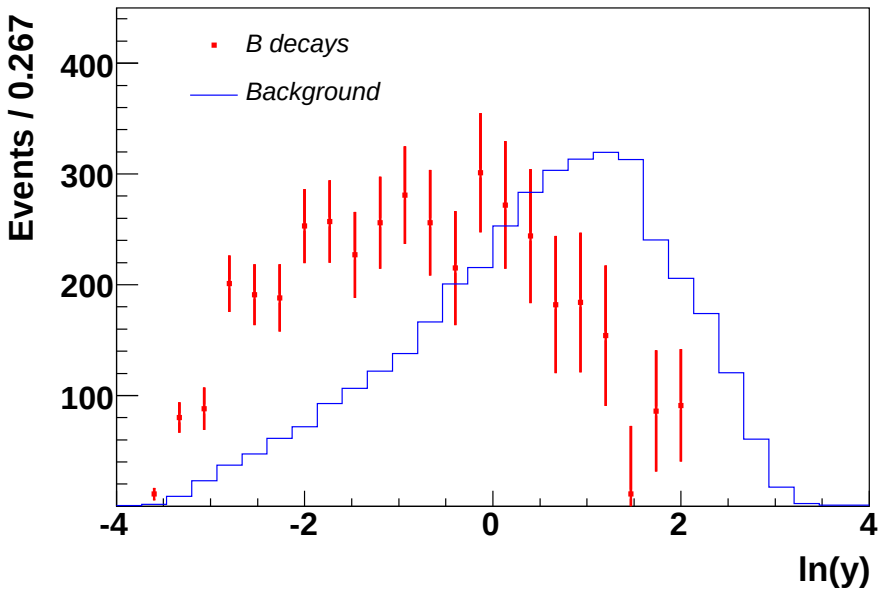

Figure 6.12: Distribution of the combined variable, y, for B meson decays and background events.

$\Lambda_c^+\mu^-$ signal was observed and used to determine an optimal cut of $\ln(y) < 0.1$ to select events for the lifetime measurement.

The $K_S^0 p$ invariant mass distribution for all $\Lambda_c^+\mu^-$ candidates, using this selection, is shown in Figure 6.13. Fitting with a Gaussian signal and fourth order polynomial background, a signal of 4437 ± 329 events is now observed at a central Λ_c^+ mass of 2285.80 ± 1.7 MeV/c^2. This mass is consistent with the PDG value of 2286.46 ± 0.14 MeV/c^2. The width of the mass peak is 20.56 ± 1.74 MeV/c^2. Using the final selection, the signal significance has been increased to approximately 16.2. Also shown in Figure 6.13 is the $K_S^0 p$ invariant mass histogram for $\Lambda_c^+\mu^+$ combinations, which shows no evidence of any excess in the signal region.

6.6 Reflection of B Meson Decays

Since the decays of B mesons also enter the sample, as described section 6.5.2, some of these events will be contribute to the $K_S^0 p$ invariant mass plot shown in

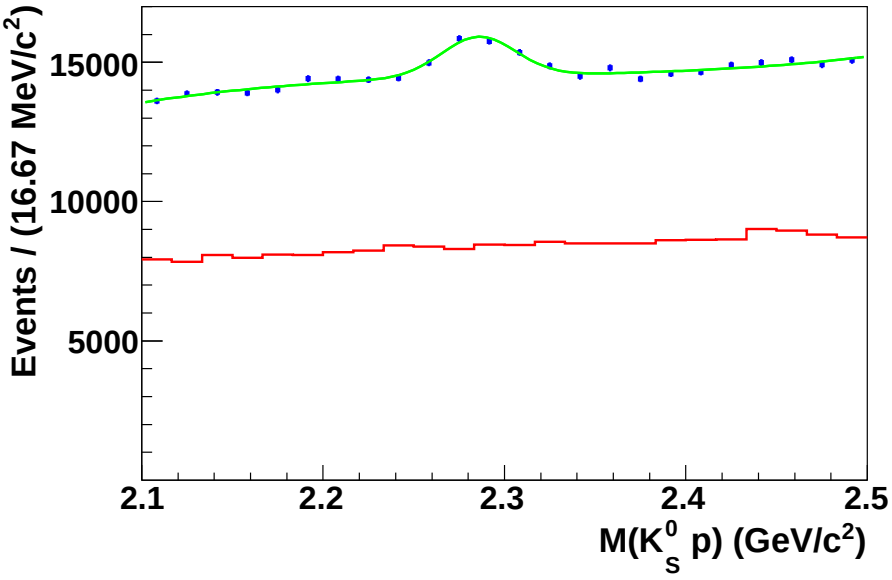

Figure 6.13: The $K^0_S p$ invariant mass for the final selection, shown for right-sign $\Lambda_c^+ \mu^-$ pairs (upper histogram) and wrong-sign $\Lambda_c^+ \mu^+$ pairs (lower histogram). The fit to the right-sign distribution yields a peak containing 4437 ± 329 events at a central mass of 2285.80 ± 1.7 MeV/c^2. The mass peak has a width of 20.56 ± 1.74 MeV/c^2.

Figure 6.13. It is necessary to ensure that the distribution of these reflected events does not contribute to the observed excess in the mass distribution.

Two Monte Carlo samples were used to show how these mass peaks appear when the π^+ or K^+ from either of these decays is wrongly assumed to be a proton. The $D^+\mu^-\bar{\nu}_\mu X$ state may be produced by several decays of $\bar{B}^0$, B^- and $\bar{B}^0_s$ mesons to excited D mesons, as well as by $\bar{B}^0 \to D^+\mu^-\bar{\nu}_\mu$. Therefore to simulate this reflection the bselect package [60] was used to produce a sample containing all of these decays. The decays included are:

- $B^- \to D_1(2420)^0\mu^-\bar{\nu}_\mu$;
- $B^- \to D^{*0}\mu^-\bar{\nu}_\mu$;
- $B^- \to D_2^*(2460)^0\mu^-\bar{\nu}_\mu$;
- $B^- \to D^*(2010)^+\pi^-\mu^-\bar{\nu}_\mu$;
- $B^- \to D^+\pi^-\mu^-\bar{\nu}_\mu$;
- $\bar{B}^0 \to D^*(2010)^+\mu^-\bar{\nu}_\mu$;
- $\bar{B}^0 \to D^+\mu^-\bar{\nu}_\mu$;
- $\bar{B}^0 \to D_1(2420)^+\mu^-\bar{\nu}_\mu$;
- $\bar{B}^0 \to D^{*+}\mu^-\bar{\nu}_\mu$;
- $\bar{B}^0 \to D^*(2460)^+\mu^-\bar{\nu}_\mu$;
- $\bar{B}^0 \to D^*(2010)^+\pi^0\mu^-\bar{\nu}_\mu$;
- $\bar{B}^0 \to D^+\pi^0\mu^-\bar{\nu}_\mu$;
- $\bar{B}^0_s \to D_{s1}(2536)^+\mu^-\bar{\nu}_\mu$;
- $\bar{B}^0_s \to D_{s2}(2573)^+\mu^-\bar{\nu}_\mu$;

- $\bar{B}_s^0 \to D^*(2010)^+ K^0 \mu^- \bar{\nu}_\mu$;
- $\bar{B}_s^0 \to D^+ K^0 \mu^- \bar{\nu}_\mu$.

D^+ mesons produced in any of these decay chains were then forced to decay to $K_S^0 \pi^+$. The decay $\bar{B}_s^0 \to D_s^+ \mu^- \bar{\nu}_\mu X (D^+ \to K_S^0 K^+)$ also enters into the selection, so a separate sample containing these decays was also generated.

The samples were reconstructed using the same procedure and selection criteria as the data, and the candidates in which the decays were properly reconstructed were identified using the generator information.

Figures 6.14 and 6.15 illustrate the reflection effects mentioned in section 6.5.2. If a pion is misidentified as a kaon, or vice versa, then the distribution of misidentified events produces a peak lying close to the peak for the correctly identified events, meaning the amount of each type of event in the sample is difficult to estimate from the data. The case in which the pion or kaon is assumed to be a proton is shown in Figure 6.16. Here it is seen that both samples produce wide distributions with no significant peaking features in the region of the Λ_c^+ mass, so these decays contribute to the background and not to the observed signal peak.

Using the relative reconstruction efficiencies, the fractions of decays to $D^+ \mu^-$ and $D_s^+ \mu^-$ in the final sample were estimated, and these were used together with the distributions in Figure 6.16 to create a combined $K_S^0 p$ mass distribution for these decays. The shorter lifetime of the D_s^+ means that the efficiency is significantly higher for these decays, and they provide a larger contribution than decays to $D^+ \mu^-$. The $K_S^0 \pi^+$ invariant mass distribution in data using the final selection was fitted to estimate the number of reflected events in the $\Lambda_c^+ \mu^-$ sample. The combined mass distribution was normalised to this number to estimate the $K_S^0 p$ mass distribution for the reflected B meson decays in the final sample. This is plotted together with the $\Lambda_c^+ \mu^-$ signal in Figure 6.17.

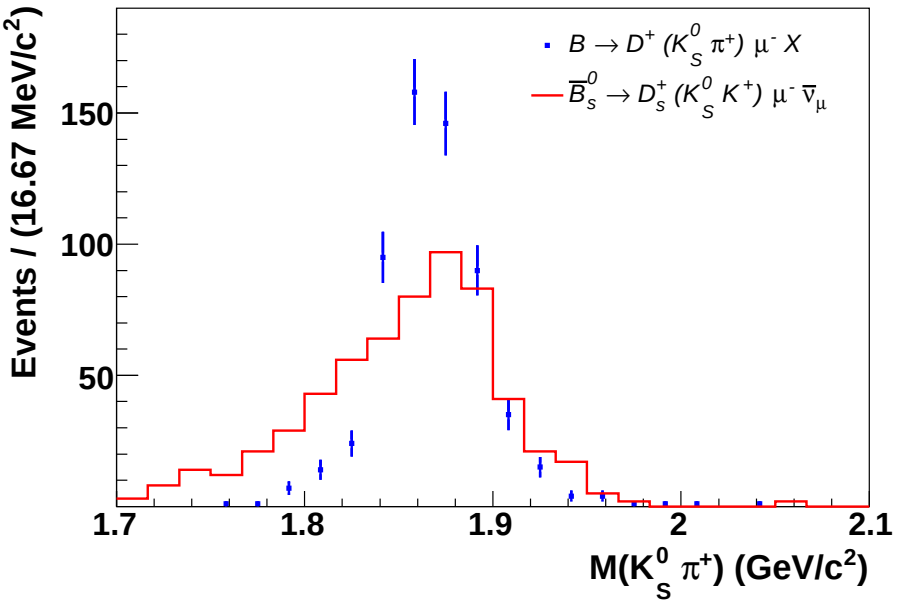

Figure 6.14: The $K^0_S\pi^+$ invariant mass for $B \to D^+\mu^-\bar{\nu}_\mu X$ ($D^+ \to K^0_S\pi^+$) decays and the reflection due to $\bar{B}^0_s \to D^+_s\mu^-\bar{\nu}_\mu X$ ($D^+_s \to K^0_s K^+$), obtained using simulated events.

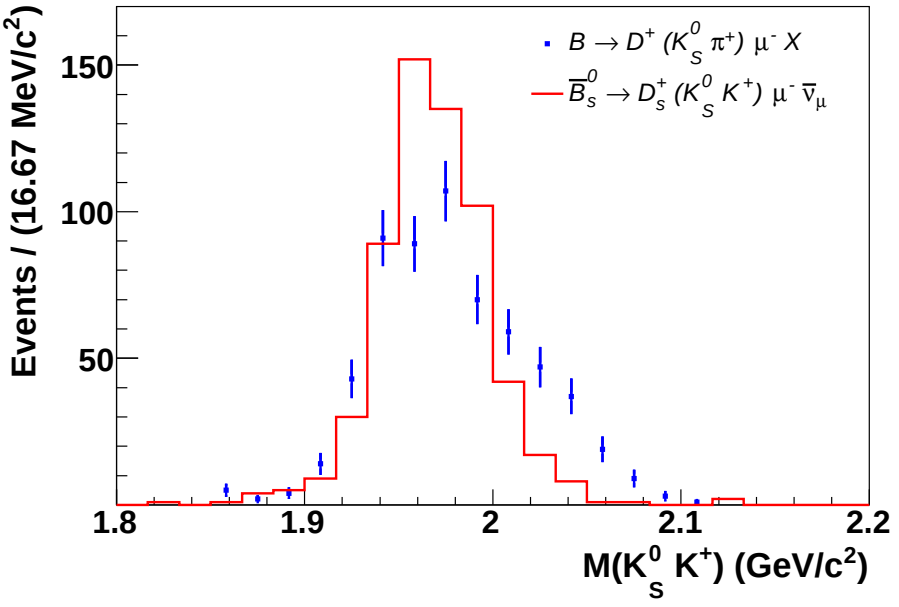

Figure 6.15: The $K^0_S K^+$ invariant mass for $\bar{B}^0_s \to D^+_s\mu^-\bar{\nu}_\mu X$ ($D^+_s \to K^0_s K^+$) decays and the reflection due to $B \to D^+\mu^-\bar{\nu}_\mu X$ ($D^+ \to K^0_S\pi^+$), obtained using simulated events.

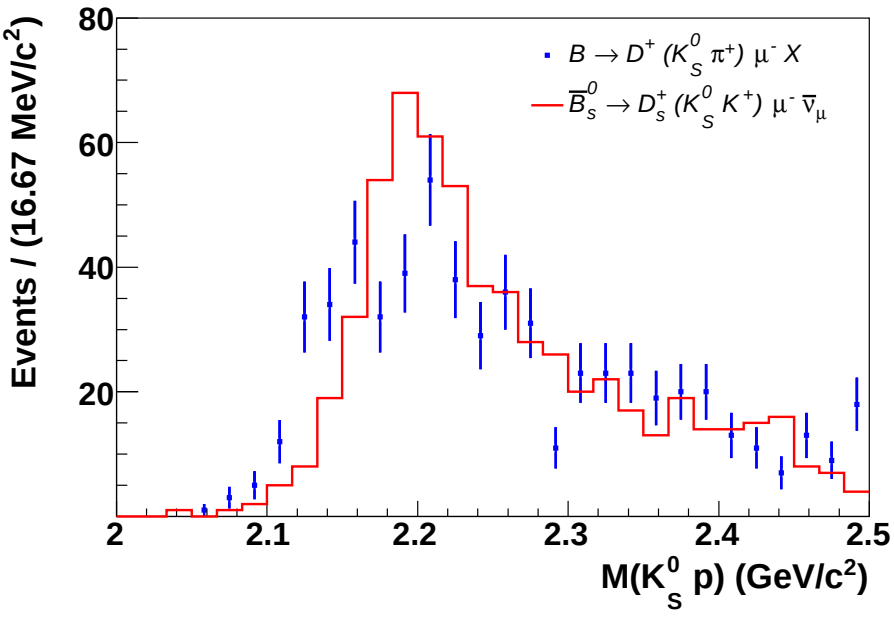

Figure 6.16: The $K^0_S p$ invariant mass distributions for $B \to D^+\mu^-\bar{\nu}_\mu X$ ($D^+ \to K^0_S\pi^+$) and $\bar{B}^0_s \to D^+_s\mu^-\bar{\nu}_\mu X$ ($D^+_s \to K^0_s K^+$) decays in which the π^+ or K^+ is misidentified as a proton, obtained using simulated events.

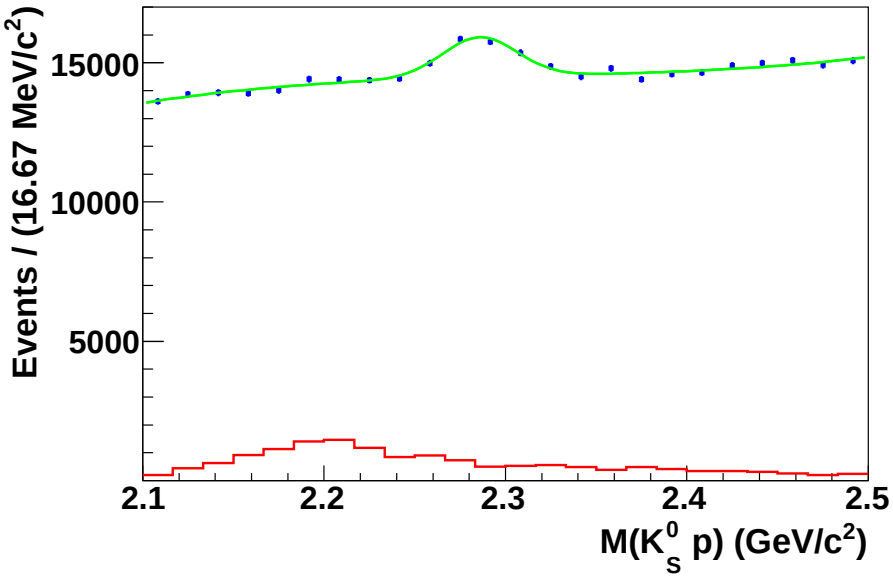

Figure 6.17: The $K^0_S p$ invariant mass for the final sample of $\Lambda^+_c\mu^-$ pairs shown together with the estimated contribution to this distribution from the reflection of $B \to D^+\mu^-\bar{\nu}_\mu X$ ($D^+ \to K^0_S\pi^+$) and $\bar{B}^0_s \to D^+_s\mu^-\bar{\nu}_\mu X$ ($D^+_s \to K^0_s K^+$) decays (lower histogram).

Chapter 7

Measurement of the Λ_b^0 Lifetime

The signal shown in the final event selection is sufficient to perform a measurement of the Λ_b^0 lifetime. The selection criteria were chosen so that the lifetime distribution in this sample should be unbiased, although so far the lack of bias is assumed and has not been checked. After defining relevant quantities, this chapter outlines the checks of the selection before describing the lifetime fitting procedure and its results. The fitting procedure is also tested for bias, and finally the systematic uncertainties on the lifetime results are estimated.

7.1 Visible Proper Decay Length and K-factor

In order to make a lifetime measurement it is necessary to measure the distance flown by each Λ_b^0 candidate before decaying, and then correct for the boost to determine the proper time for which the particle lived. The distribution of proper lifetimes can then be fitted to obtain a measurement of the mean lifetime.

If the lifetime of a particle in its rest frame is denoted τ, then the lifetime in the lab frame for a particle moving with speed v is given by $\tau' = \gamma\tau$, where $\gamma = 1/\sqrt{1-\beta^2}$ for $\beta = v/c$. Therefore the distance travelled in the lab frame is $v\gamma\tau$. If both mass, m, and momentum, p, are quoted in units of GeV, the

momentum is given by $p = \beta\gamma m$ and hence the decay length L is given by

$$L = v\gamma\tau = \frac{pc}{\gamma m}\gamma\tau = \frac{pc\tau}{m}. \tag{7.1}$$

In this analysis the transverse component of the decay length, L_{xy}, and the transverse momentum are used, since measurements in the transverse plane have greater precision than 3-dimensional measurements. In this case the above is converted to the following relation:

$$L_{xy} = \frac{c\tau p_T}{m}. \tag{7.2}$$

In the semileptonic decays used in this analysis the Λ_b^0 candidates are not fully reconstructed, so $p_T(\Lambda_b^0)$ cannot be measured. Instead $p_T(\Lambda_c^+\mu^-)$ is measured and the distribution of the quantity known as *visible proper decay length* (VPDL) is fitted. The VPDL, λ, for a Λ_b^0 candidate which lives for a proper time τ_{Λ_b}, is given by

$$\lambda = \frac{c\tau_{\Lambda_b}}{K} = L_{xy}\frac{m(\Lambda_b^0)}{p_T(\Lambda_c^+\mu^-)}, \tag{7.3}$$

where K is a correction factor for the missing momentum,

$$K = \frac{p_T(\Lambda_c^+\mu^-)}{p_T(\Lambda_b^0)}. \tag{7.4}$$

Therefore to measure the lifetime using semileptonic decays, the K-factor must be estimated. The probability distribution for the K-factor is obtained from Monte

Carlo, as outlined in section 7.3.

The measured value of the transverse decay length, L_{xy}, is defined by

$$L_{xy} = \frac{\vec{X} \cdot \vec{p_T}(\Lambda_c \mu)}{|p_T(\Lambda_c \mu)|} \tag{7.5}$$

where $\vec{X}$ is the vector pointing from the primary vertex to the Λ_b^0 decay vertex in the transverse plane. The projection of $\vec{X}$ onto the transverse momentum is used in preference to $|\vec{X}|$ to estimate the decay length, since for candidates with very short lifetimes the resolution effects will play a large part in determining $\vec{X}$, and only its component parallel to the Λ_b^0 momentum may be attributed to the lifetime. When calculating L_{xy} the primary vertex position is calculated with the tracks from the decay products of the Λ_b^0 removed to avoid these biasing the primary vertex position towards the secondary vertex.

Measured values of the VPDL are referred to as λ_M in the following sections. λ refers to the true value of the visible proper decay length, or the generated value in the case of Monte Carlo events.

7.2 Checks of Selection

As stated previously, an unbiased selection with respect to lifetime is necessary to obtain a correct measurement of the lifetime. Therefore variables which are known to be uncorrelated with the lifetime were chosen as the discriminating variables used to reduce background. Monte Carlo can be used to check the selections to ensure that no lifetime bias is present in the sample. A sample of the decays $\Lambda_b^0 \to \Lambda_c^+ \mu^- \bar{\nu}_\mu$ with $\Lambda_c^+ \to K_S^0 p$ was generated and was reconstructed using the methods and selection criteria applied to the data. The generator level information was used to establish which decays had been correctly reconstructed.

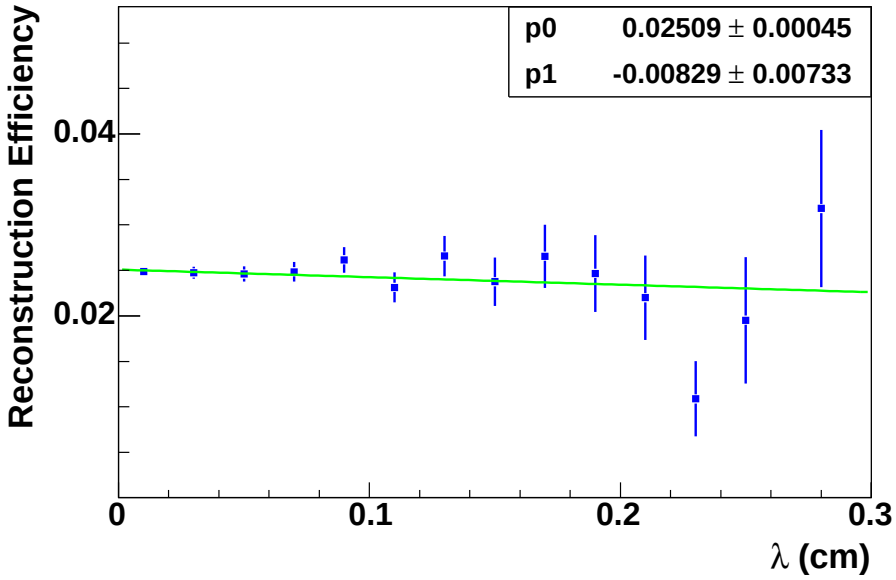

Figure 7.1: The efficiency of event selection for the $\Lambda_b^0 \to \Lambda_c^+ \mu^- \bar{\nu}_\mu$ Monte Carlo sample, versus the generated visible proper decay length.

The fraction of generated events that were correctly reconstructed was calculated for several intervals of generated VPDL. These fractions are plotted in Figure 7.1 to show the dependence of the reconstruction efficiency on λ. Here it is shown that the efficiency does not change significantly for values of λ up to 0.3cm. Therefore the selection criteria are shown to have no statistically significant biasing effect on the generated lifetime distribution.

The deviations between measured and generated values of VPDL for correctly reconstructed events are plotted in Figure 7.2. These are used to check that the measured values are not biased with respect to the generated VPDL values. Since the fitted mean for neither of the two Gaussian functions deviates significantly from zero, it is shown that the measured VPDL values are symmetrically distributed around the generated values, with no tendency towards lower or higher values.

Since these studies indicate no significant biasing effects, the sample may be used to provide an unbiased measurement of the Λ_b^0 lifetime, and the following

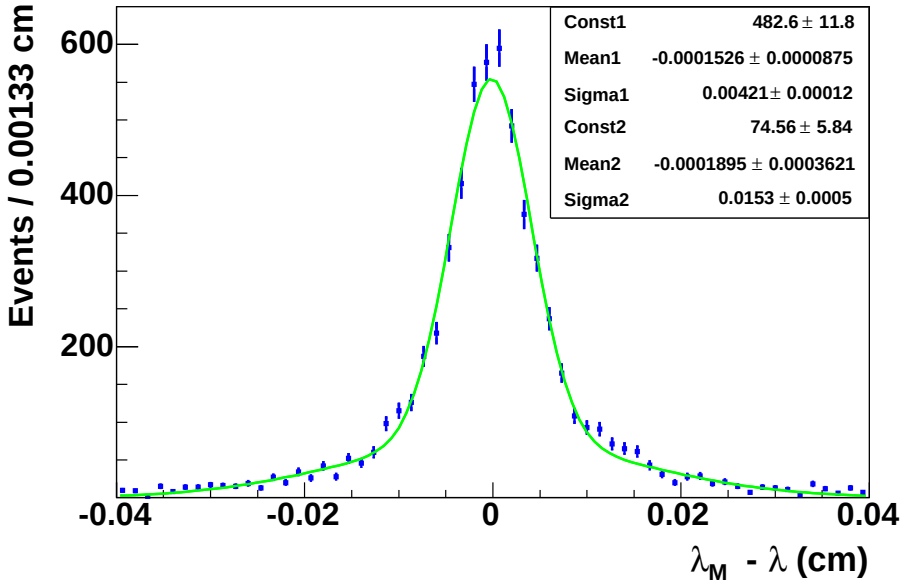

Figure 7.2: The distribution of the difference between generated and reconstructed visible proper decay length in simulated $\Lambda_b^0 \to \Lambda_c^+ \mu^- \bar{\nu}_\mu$ decays, fitted with the sum of two Gaussians.

sections describe the necessary inputs and the measurement procedure used.

7.3 K-factor Estimation

As mentioned in section 7.1, to perform any kind of lifetime fit to the VPDL distribution requires estimation of the K-factor for the events. This requires knowledge of the decays that are present in the signal. The sample will contain the *elastic* decay $\Lambda_b^0 \to \Lambda_c^+ \mu^- \bar{\nu}_\mu$ and *inelastic* decays $\Lambda_b^0 \to \Lambda_c^+ \mu^- \bar{\nu}_\mu X$, where X is any other particle(s) in the final state. In each of these cases the Λ_b^0 candidate is reconstructed using only the Λ_c^+ and the muon. If the final state does contain additional particle(s), on average the values of $p_T(\Lambda_c^+ \mu^-)$ will be decreased, and hence the value of the mean K-factor will be lower. Therefore the fraction of inelastic decays in the sample must be estimated, with errors assigned to the final result to account for any uncertainty.

7.3.1 Inelastic Decays

There are many potential decays that would give additional particles in the final state, many of which have unknown branching fractions. Therefore a precise simulation of the sample is not possible, instead the K-factor distribution for the sample is constructed using the elastic decay and one type of inelastic decay. The effects of additional inelastic decays can then be accounted for in the systematic uncertainties by variation of the inelastic contribution over a larger range than that expected for the particular inelastic decay used.

The inelastic Monte Carlo sample consists of equal fractions of the decays $\Lambda_b^0 \to \Sigma_c^{++}\pi^-\mu^-\bar{\nu}_\mu$, $\Lambda_b^0 \to \Sigma_c^+\pi^0\mu^-\bar{\nu}_\mu$ and $\Lambda_b^0 \to \Sigma_c^0\pi^+\mu^-\bar{\nu}_\mu$. The Σ_c states subsequently undergo the strong decay $\Sigma_c \to \Lambda_c^+\pi$, with a branching fraction of 100%, leading to a final state containing two additional pions. It is also possible that the Λ_b^0 decays semileptonically to an excited Λ_c^+, which then decays to $\Sigma_c\pi$ or directly to $\Lambda_c^+\pi^+\pi^-$, giving the same final state, but with slight variations in the kinematics. The relative proportions of Λ_b^0 semileptonic decays that result in $\Lambda_c^+ l^-\bar{\nu}_l$ and $\Lambda_c^+ l^-\bar{\nu}_l\pi^+\pi^-$ final states have been measured by DELPHI [71], giving the relative decay rate for elastic decays to be

$$\frac{\Gamma(\Lambda_b^0 \to \Lambda_c^+ l^-\bar{\nu}_l)}{\Gamma(\Lambda_b^0 \to \Lambda_c^+ l^-\bar{\nu}_l) + \Gamma(\Lambda_b^0 \to \Lambda_c^+\pi^+\pi^- l^-\bar{\nu}_l)} = 0.47^{+0.10}_{-0.08}(\text{stat})^{+0.07}_{-0.06}(\text{syst}). \quad (7.6)$$

This ratio will be used to determine the contribution due to inelastic decays to include in the K-factor distribution. This is the only inelastic final state for which such a measurement exists.

Additional contributions may arise from decays in which the muon is produced in a subsequent decay, such as in $\Lambda_b^0 \to \Lambda_c^+\tau^-\bar{\nu}_\tau$ followed by $\tau^- \to \mu^-\bar{\nu}_\mu\nu_\tau$. Another possibility is that the Λ_b^0 decays hadronically to a state including a Λ_c^+, and a muon is then produced by the decay of another hadron among the decay

products. The most likely of these is $\Lambda_b^0 \to \Lambda_c^+ D_s^{(*)-}$, where a D_s^{*-} decays strongly to produce $D_s^- \gamma$ or $D_s^- \pi^0$. The D_s^- may then decay semileptonically, with a resulting muon potentially being vertexed with the Λ_c^+. The lifetimes of the τ^- and D_s^- and additional particles in the final state of the $\Lambda_b^0 \to \Lambda_c^+ D_s^{(*)-}$ decays will mean the reconstruction efficiency is further reduced for these channels. A Monte Carlo sample of the $\Lambda_b^0 \to \Lambda_c^+ D_s^{(*)-}$ decays was generated and reconstructed. No measurement of the branching fraction for these decays is available, however the low reconstruction efficiency of around 19% relative to the elastic decay combined with the semileptonic branching fraction of the D_s^- meson means that even if the branching fraction is equal to that of the elastic decay, the contribution from this decay will still be below 1%, and hence is assumed to be negligible. The fraction of $\Lambda_b^0 \to \Lambda_c^+ \tau^- \bar{\nu}_\tau$ decays is suppressed due to the branching fraction of $\tau^- \to \mu^- \bar{\nu}_\mu \nu_\tau$ of approximately 18% [2]. Due to the lifetime of the τ, the efficiency should be lower than that of $\Lambda_b^0 \to \Sigma_c \pi \mu^- \bar{\nu}_\mu$, leading to a contribution of only a few percent. These and any other decays are accounted for in the systematic uncertainties by increasing the fraction of $\Lambda_b^0 \to \Sigma_c \pi \mu^- \bar{\nu}_\mu$ decays above the expected range.

7.3.2 Combination of Distributions

To obtain the elastic and inelastic fractions to be used in estimating the full K-factor distribution, the relative branching fraction was set according to the value shown in (7.6). The inelastic Monte Carlo sample contains decays to each of the three Σ_c baryons, one of which results in a final state containing two neutral pions. The DELPHI measurement only refers to final states containing two charged pions, so the inelastic branching fraction used was 1.5 times the value implied by (7.6).

The efficiencies and branching fractions were combined to estimate the elastic and inelastic fractions. The values are shown in Table 7.1, with the inelastic branching fraction and efficiency shown relative to the values for the elastic sam-

	$\Lambda_b^0 \to \Lambda_c^+ \mu^- \bar{\nu}_\mu$	$\Lambda_b^0 \to \Sigma_c \pi \mu^- \bar{\nu}_\mu$
Relative Branching Fraction	1	1.6915
$\langle K \rangle$	0.8933	0.8010
Relative Efficiency	1	0.342
f_K	0.6332	0.3668

Table 7.1: K-factor information and efficiency for the elastic and inelastic samples. The fractions f_K give the fraction of each process in the combined K factor distribution.

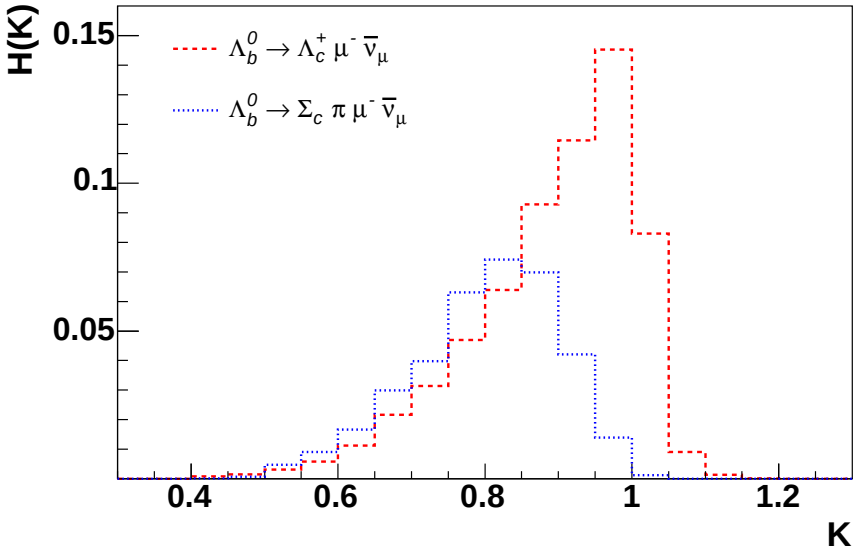

Figure 7.3: K-factor distributions for the elastic and inelastic processes, shown normalised to their estimated fractions, f_K.

ple.

Figure 7.3 shows the K-factor distributions for each of the samples, shown in their normalised fractions. Figure 7.4 shows the combined K-factor distribution used for the lifetime fit, obtained by adding the elastic and inelastic contributions.

7.4 Physics Background

The signal peak seen in Figure 6.13 is likely to contain significant contributions from other processes that produce a $\Lambda_c^+ \mu^-$ pair in the final state. These will have

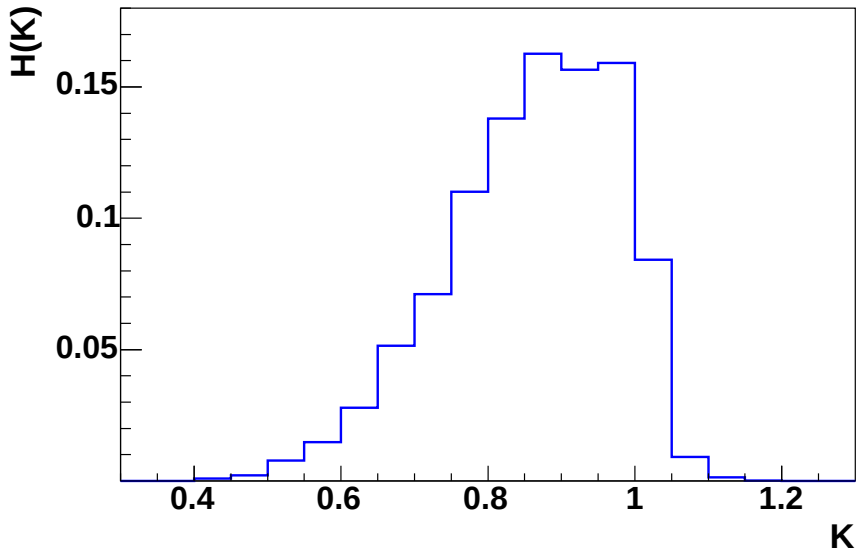

Figure 7.4: The combined K-factor distribution for elastic and inelastic decays.

a different lifetime distribution to the signal and hence their contributions must be estimated in the measurement procedure.

7.4.1 Peaking Background

The signal peak may also contain events in which the Λ_c^+ and μ^- are produced by decays of different particles, but are vertexed together to give a fake Λ_b^0 candidate. In addition to decays of Λ_b^0, a Λ_c^+ may also be produced by the hadronisation of a $c\bar{c}$ quark-antiquark pair arising from a hard scatter. $c\bar{c}$ pairs are readily produced at the Tevatron, with a cross section approximately ten times that for $b\bar{b}$ production [15]. Hence a Λ_c^+ baryon has a higher probability of being created at the primary vertex than in a b hadron decay. The other charm hadron produced may decay semileptonically to give a μ^-, which could then be vertexed with the Λ_c^+ if the tracks pass in sufficiently close proximity to each other. Since the crossing point of the Λ_c^+ and the muon track is random, the measured lifetime distribution of the Λ_b^0 candidates should be centred on zero in such events. Similar but smaller

contributions may also arise from $b\bar{b}$ events, where a b-hadron decays to a Λ_c^+ with the other b-hadron producing a μ^-, or from events in which a track is incorrectly identified as a muon. These processes are referred to as *peaking background*. They are expected to produce a significant fraction of the measured signal, and hence their visible proper decay length distribution must be known to accurately fit the Λ_b^0 lifetime. In similar analyses this fraction has been around 10% of the signal [72].

The measured VPDL distribution of such events was determined by producing a sample of simulated $c\bar{c}$ events. Λ_c^+ baryons produced from a c quark at the primary vertex were forced to decay to $K_S^0 p$. D^-, $\bar{D}^0$ D_s^- and $\bar{\Lambda}_c^-$ produced from a $\bar{c}$ quark were decayed to all semi-muonic final states. The sample was reconstructed and passed through the same selections as the data. The events in which a Λ_b^0 candidate was constructed from the Λ_c^+ and μ^- were then selected and their distribution of λ_M was plotted. This is shown in Figure 7.5, where it is fitted with the sum of two Gaussian functions. The width of the main Gaussian is observed to be around 92 μm, while a smaller fraction of events produce a much wider distribution with width around 337 μm. The shape of this distribution is used to model the peaking background contribution in the lifetime fit. The parameters are later varied in accordance with the given errors to estimate the associated systematic uncertainties.

7.4.2 Other b-baryons and B Meson Decays

b-baryon Decays

Strange b baryons have been observed by DELPHI [73], with this observation being confirmed by ALEPH [74]. These consist of the $\Xi_b^0(usb)$ and the $\Xi_b^-(dsb)$. A more recent analysis [75] by DELPHI has produced the product branching ratio measurement,

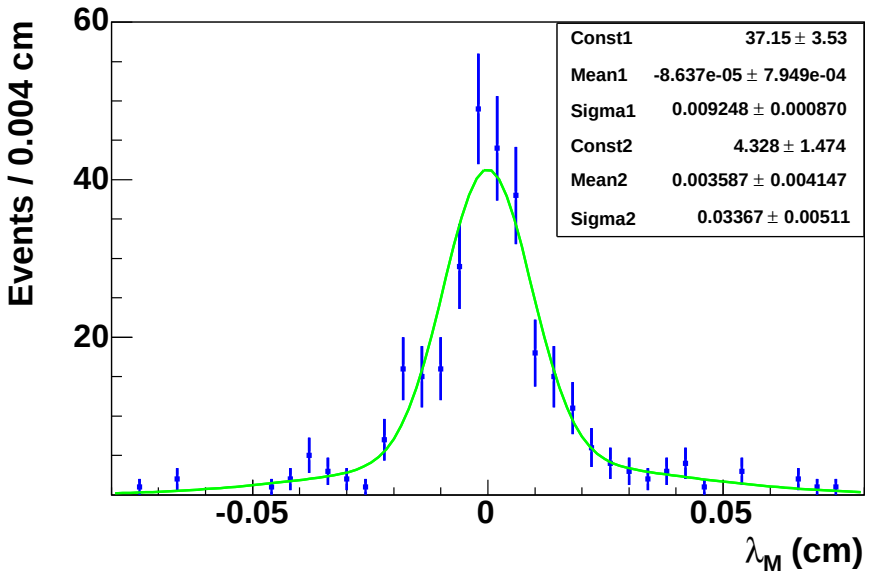

Figure 7.5: The λ_M distribution for simulated $c\bar{c} \to \Lambda_c^+ \mu^- X$ events passing the selection criteria, fitted with the sum of two Gaussians.

$$\mathrm{BR}(b \to \Xi_b) \cdot \mathrm{BR}(\Xi_b \to \Xi^- l^- X) = (3.0 \pm 1.0(\mathrm{stat}) \pm 0.3(\mathrm{syst})) \times 10^{-4}, \quad (7.7)$$

which is averaged for decays to muons and electrons. Here the Ξ_b is expected first to decay to $X_c X l^- \bar{\nu}_l$, where X_c is a charmed baryon, followed by the decay $X_c \to \Xi^- X'$. Assuming all of the X_c produced are either a Ξ_c state or a Λ_c^+, the fraction of the observed decays in which X_c is a Λ_c^+ is given by

$$R_{\Lambda_c} = \frac{\mathrm{BR}(\Xi_b \to \Lambda_c^+ X l \bar{\nu}_l)\mathrm{BR}(\Lambda_c^+ \to \Xi^- X')}{\mathrm{BR}(\Xi_b \to \Xi_c X l \bar{\nu}_l)\mathrm{BR}(\Xi_c \to \Xi^- X') + \mathrm{BR}(\Xi_b \to \Lambda_c^+ X l \bar{\nu}_l)\mathrm{BR}(\Lambda_c^+ \to \Xi^- X')} \quad (7.8)$$

The only observed decay of Λ_c^+ to a state including a Ξ^- is $\Lambda_c^+ \to \Xi^- K^+ \pi^+$ with a branching fraction of $(4.9 \pm 1.7) \times 10^{-3}$ [2]. The absolute branching fractions of Ξ_c are not known, but it will be assumed that a Ξ^- is produced in 35% of Ξ_c

decays, since this fraction of Λ_c^+ decays produce a Λ^0. The semileptonic decays of Ξ_b are expected to predominantly produce a Ξ_c via the simple spectator decay analogous to $\Lambda_b^0 \to \Lambda_c^+ \mu^- \bar{\nu}_\mu$. Assuming a contribution of Λ_c^+ to X_c of the order of 10% allows it to be estimated that

$$R_{\Lambda_c} \approx 1.55 \times 10^{-3}. \tag{7.9}$$

This leads to an estimate of the combined branching fraction,

$$\begin{aligned} \mathrm{BR}(b \to \Xi_b) \cdot \mathrm{BR}(\Xi_b \to \Lambda_c^+ X l^- \bar{\nu}_l) &= \frac{\mathrm{BR}(b \to \Xi_b) \cdot \mathrm{BR}(\Xi_b \to \Xi^- l^- X) \times R_{\Lambda_c}}{\mathrm{BR}(\Lambda_c^+ \to \Xi^- K^+ \pi^+)} \\ &\approx 9.5 \times 10^{-5}. \end{aligned} \tag{7.10}$$

A measurement of Λ_b^0 production was performed by ALEPH [24], giving

$$\mathrm{BR}(b \to \Lambda_b^0) \cdot \mathrm{BR}(\Lambda_b^0 \to \Lambda_c^+ l^- \bar{\nu}_l X) = (0.86 \pm 0.07(\mathrm{stat}) \pm 0.14(\mathrm{syst}))\%. \tag{7.11}$$

Therefore the ratio of combined branching fractions is

$$\frac{\mathrm{BR}(b \to \Xi_b) \cdot \mathrm{BR}(\Xi_b \to \Lambda_c^+ X l^- \bar{\nu}_l)}{\mathrm{BR}(b \to \Lambda_b^0) \cdot \mathrm{BR}(\Lambda_b^0 \to \Lambda_c^+ l^- \bar{\nu}_l X)} \approx 0.011. \tag{7.12}$$

As seen previously, the reconstruction efficiency is considerably reduced for decays with additional particles in the final state. Assuming an efficiency relative to the elastic signal decay of 30%, the decays of Ξ_b will provide a contribution of around 0.3%. Due to the presence of multiple additional particles in the final state, the efficiency is likely to be considerably lower than that of the $\Lambda_b^0 \to$

$\Sigma_c \pi \mu^- \bar{\nu}_\mu$, and hence this estimate is very conservative. The assumed values used for this computation may be varied considerably without the Ξ_b fraction being estimated to be greater than 1%, and hence this contribution will be considered to be negligible.

Other predicted b-baryons include the Σ_b states (uub, udb, ddb), which are expected to decay strongly [76] and so will not impact the lifetime measurement, and the $\Omega_b(ssb)$, which should provide an even smaller contribution than Ξ_b.

B Meson Decays

B^0/B^+ mesons are observed to decay to states including a Λ_c^+ or $\bar{\Lambda}_c^-$. The branching fraction for $B \to \Lambda_c^+/\bar{\Lambda}_c^- X$ is measured to be 6.4 ± 1.1 % [2]. A 90% confidence limit has been established for the fraction of these decays which contain $\Lambda_c^+ e^- X$ [77], leading to the 90% confidence limit for the branching fraction,

$$\mathrm{BR}(B \to \Lambda_c^+ e^- X) < 3.2 \times 10^{-3} \quad (90\%\mathrm{C.L.}). \tag{7.13}$$

Due to the higher production rates these decays could produce a significant fraction of $\Lambda_c^+ \mu^-$ pairs, assuming the same limit for states containing a muon. However additional particles in the final state cause considerable reductions in selection efficiency, as seen in the consideration of the inelastic fraction for the K-factor distribution. Since this final state must contain an additional baryon as well as the Λ_c^+, the efficiencies are likely to be much lower still, and value of 20% relative to the elastic Λ_b^0 decay is assumed here as a conservative estimate. The fraction of B meson decays in the sample is then given by

$$f(B \to \Lambda_c^+ \mu^- X) = \frac{F_B \times \mathrm{BR}(B \to \Lambda_c^+ e^- X) \times 0.20}{F_{b-baryon} \times \mathrm{BR}(\Lambda_b^0 \to \Lambda_c^+ \mu^- \bar{\nu}_\mu X)}, \tag{7.14}$$

where F_B is the combined production fraction for B^+ and B^0 mesons, and $F_{b-baryon}$ is the fraction for b-baryons, which is assumed to be dominated by Λ_b^0. The values for these quantities were obtained from those shown in Table 2.2. Inserting these values gives the estimate,

$$f(B \to \Lambda_c^+ \mu^- X) < 0.056 \quad (90\%\text{C.L.}). \tag{7.15}$$

Hence the contribution due to these decays is likely to be roughly 5% or lower. This contribution is not included in the fitting procedure, but its effects are estimated in the consideration of systematic uncertainties, since only an upper limit estimate is available.

7.5 Lifetime Fitting Procedure

To determine the mean Λ_b^0 lifetime, $\tau(\Lambda_b^0)$, the visible proper decay length was measured for each event. A binned minimum χ^2 fit was then used to extract the mean lifetime from the distribution of λ_M values. Attempts to perform an unbinned maximum likelihood fit, as used for all previous Λ_b^0 lifetime measurements, did not yield stable results in this case. The unbinned fit requires the use of sideband samples to constrain the background lifetime distribution, under the assumption that the lifetime characteristics of the sideband samples match those of the background under the signal peak. Either the assumption is not valid here, or the high background in this data sample causes problems for this method. Hence an alternative fitting method was used, as described below.

7.5.1 Method

The sample was split into subsamples with λ_M in the ranges shown in Table 7.2. For each of these bins, $M(K_S^0 p)$ was plotted and the binned histogram fitted with

a distribution consisting of a Gaussian signal peak and a fourth order polynomial background. The central mass and the width of the mass peak were fixed in these fits to the values obtained in the fit to the full sample shown in Figure 6.13. The yields of $\Lambda_c^+\mu^-$ pairs, n_i, and their uncertainties, σ_i, were obtained from the fits. The fitted $M(K_S^0 p)$ distributions are shown in Figure 7.6, and the n_i and σ_i values obtained are listed in Table 7.2. It can be seen in Figure 7.6 that the distribution of the combinatorial background changes significantly across the range of λ_M. This background contains contributions from many sources, which will have different fractions in each of the bins. For example, at the larger values of λ_M there will be a higher proportion of events in which a fake Λ_c^+ is constructed from the decay products of a b-hadron, whereas at values close to zero the background will be dominated by associations of unrelated tracks originating from the primary vertex. This fitting procedure obtains the number of $\Lambda_c^+\mu^-$ pairs in each bin, and these are used to extract the lifetime. This ensures that the background characteristics do not influence the lifetime fit.

Using a probability distribution, $F(\lambda_M)$, for λ_M in the signal and peaking background events, the expected $\Lambda_c^+\mu^-$ yield, n_i^e, in bin i is given by

$$n_i^e = N_{TOT} \int_i F(\lambda_M) d\lambda_M, \tag{7.16}$$

where the integration is performed over the width of bin i. N_{TOT} is the total number of events in the signal peak for the full data sample. With $c\tau(\Lambda_b^0)$ a free parameter of $F(\lambda_M)$, the best fitting value of $c\tau(\Lambda_b^0)$ is obtained by minimisation of the χ^2:

$$\chi^2 = \sum_{i=1}^{N_{BINS}} \frac{(n_i - n_i^e)^2}{\sigma_i^2}. \tag{7.17}$$

λ_M range(cm)	$\Lambda_c^+\mu^-$ yield
$[-0.06, -0.04]$	62 ± 48
$[-0.04, -0.02]$	66 ± 69
$[-0.02, 0.00]$	587 ± 156
$[0.00, 0.02]$	1172 ± 173
$[0.02, 0.04]$	999 ± 99
$[0.04, 0.06]$	540 ± 69
$[0.06, 0.08]$	299 ± 54
$[0.08, 0.10]$	225 ± 44
$[0.10, 0.20]$	454 ± 64
$[0.20, 0.30]$	47 ± 34

Table 7.2: $\Lambda_c^+\mu^-$ yields for the λ_M bins.

7.5.2 Lifetime Probability Distribution

The fit to the data must allow for contributions from signal and peaking background, and hence the basic form of $F(\lambda_M)$ is the following:

$$F(\lambda_M) = (1 - f_{bkg})F_{sig}(\lambda_M) + f_{bkg}F_{bkg}(\lambda_M). \tag{7.18}$$

$F_{sig}(\lambda_M)$ is the distribution of λ_M for the signal events, and $F_{bkg}(\lambda_M)$ is the distribution for the peaking background. f_{bkg} is the fractional contribution of peaking background. $F_{bkg}(\lambda_M)$ is parametrised by a double Gaussian centred on zero, with the widths and relative normalisation given by the parameters in Figure 7.5. The distribution for the signal events, $F_{sig}(\lambda_M)$, is given by

$$F_{sig}(\lambda_M) = \int dK H(K)\Big[\theta(\lambda)\frac{K}{c\tau(\Lambda_b^0)}e^{-K\lambda/c\tau(\Lambda_b^0)} \otimes R(\lambda_M - \lambda, s)\Big], \tag{7.19}$$

where $\theta(\lambda)$ is the step function. A normalised decay exponential is smeared with the K-factor distribution to give the expected distribution of λ. To obtain the probability density for λ_M, the distribution is also smeared by convolution with a

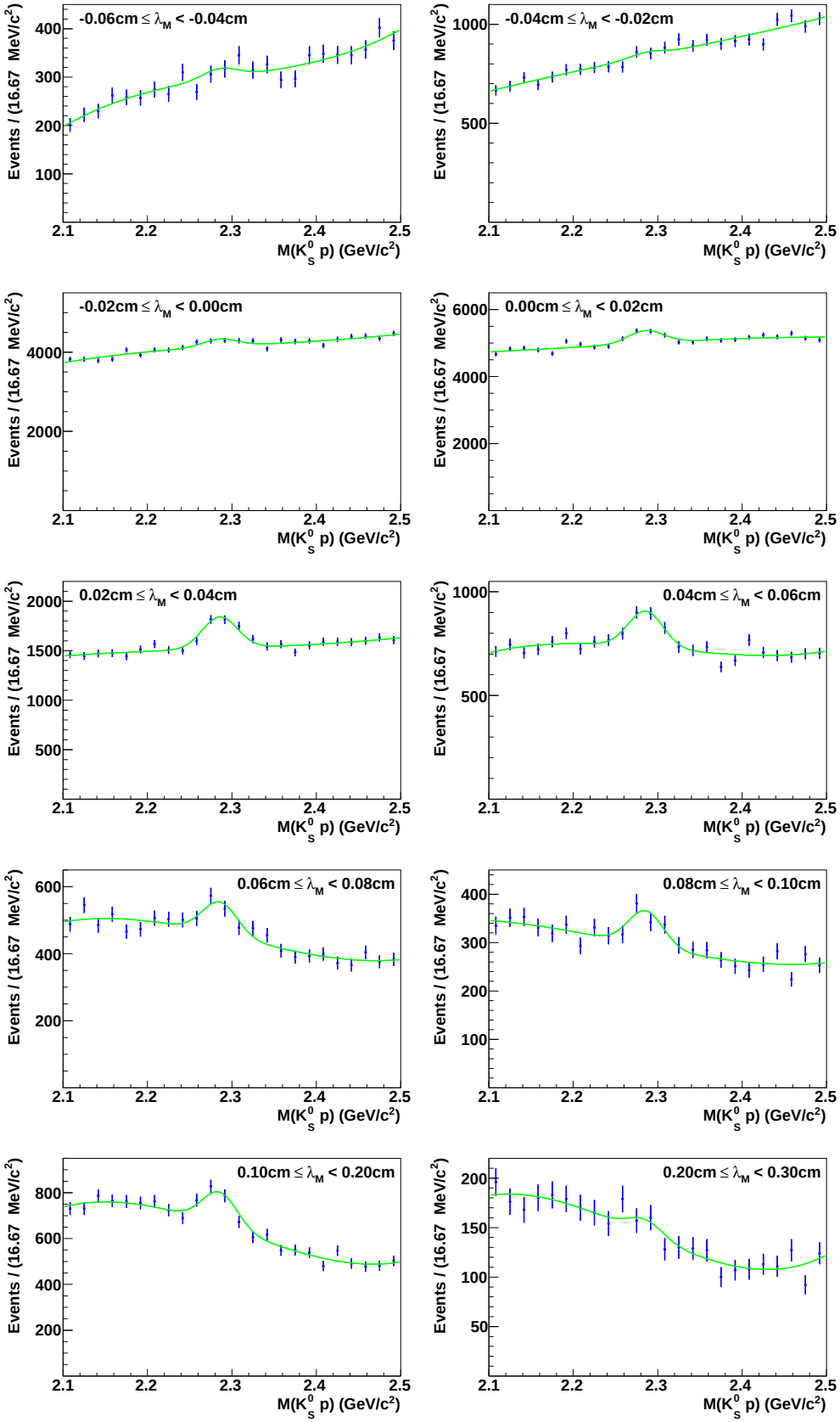

Figure 7.6: The fitted $K^0_S p$ invariant mass distributions for $\Lambda_c^+ \mu^-$ candidates within each of the λ_M bins shown in Table 7.2.

resolution function of the form

$$R(\lambda_M - \lambda, s) = \int P(\sigma) G(\lambda_M - \lambda, \sigma, s) d\sigma. \tag{7.20}$$

σ is the uncertainty in λ_M, obtained from the track and vertex uncertainties. $P(\sigma)$ is the probability distribution for σ for the signal events and $G(\lambda_M - \lambda, \sigma, s)$ is a Gaussian function given by

$$G(\lambda_M - \lambda, \sigma, s) = \frac{1}{\sqrt{2\pi}\sigma s} e^{\frac{-(\lambda_M - \lambda)^2}{2(\sigma s)^2}}. \tag{7.21}$$

A dimensionless scale factor, s, is included, giving this Gaussian a width of (σs). s exists to account for the possibility that the errors on λ_M are not correctly estimated. The track parameter uncertainties may be misestimated due to incomplete modelling of the effects of the detector material on particles passing through. This will lead to the errors on λ_M being incorrectly estimated. s is included to adjust all of the λ_M uncertainties to correct for this systematic effect. It may be released as a free parameter with its value obtained by the best fit to the data, or fixed based on information from other sources, as described in the following section. In addition to $c\tau(\Lambda_b^0)$, the other free parameters of the fit are N_{TOT} and f_{bkg}.

In practice the integral over K in (7.19) was replaced by a sum over the bins in the K-factor distribution in Figure 7.4. Similarly, the integral over σ in equation (7.20) was replaced by a sum over the bins in the distribution shown in Figure 7.8. This distribution was obtained using a technique similar to that used in the likelihood ratio selection in section 6.5.2. An additional cut requiring $\lambda_M > 200\mu$m was applied to reduce the level of background below the signal peak and decrease the contribution from peaking background. The resulting $M(K_S^0 p)$

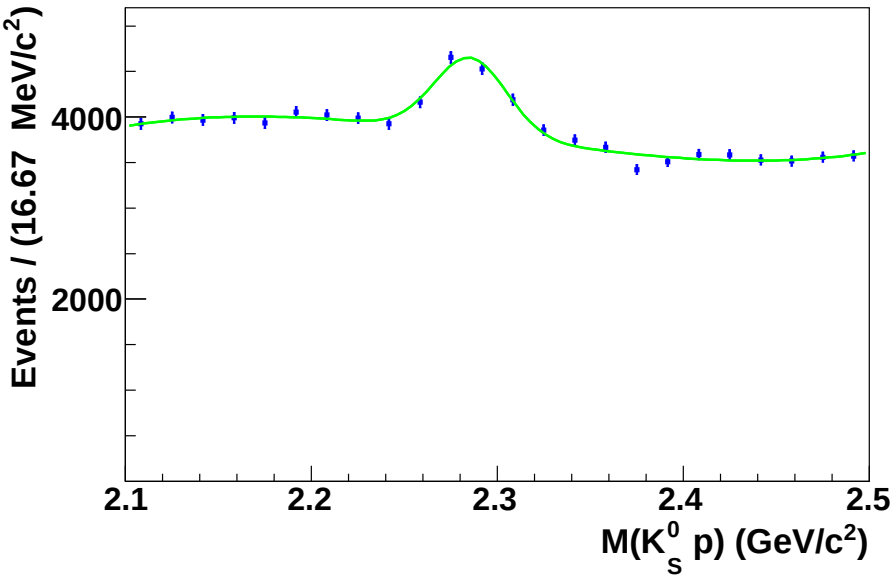

Figure 7.7: The $K^0_S p$ invariant mass for $\Lambda^+_c \mu^-$ pairs in the final sample with $\lambda_M > 200\mu$m.

distribution is shown in Figure 7.7. A signal region was defined in the range $2245 < M(K^0_S p) < 2327$ MeV/c^2, and sidebands at $2184 < M(K^0_S p) < 2225$ MeV/c^2 and $2347 < M(K^0_S p) < 2388$ MeV/c^2. The plot of $P(\sigma)$ was then obtained by subtracting the distribution of σ for the sideband samples from that of the signal region.

7.5.3 Scale Factor Measurement

The scale factor, s, has been measured for another analysis which uses the decay $\bar{B}^0_s \to D^+_s \mu^- X(D^+_s \to K^0_S K^+)$ [78]. In that analysis, a separate study was performed using the decay $D^{*+} \to D^0 \pi^+$ with $D^0 \to K^0_S \pi^- \mu^+ X$. The D^{*+} meson is predominantly produced in $c\bar{c}$ production, and decays by the strong interaction. Hence its decay vertex coincides with the primary vertex. The measured visible proper decay length of the D^{*+} meson is therefore determined by the detector resolution. The width of the distribution of the VPDL pull, λ_M/σ, gives a measurement of the scale factor. The value was determined for events with K^0_S decay

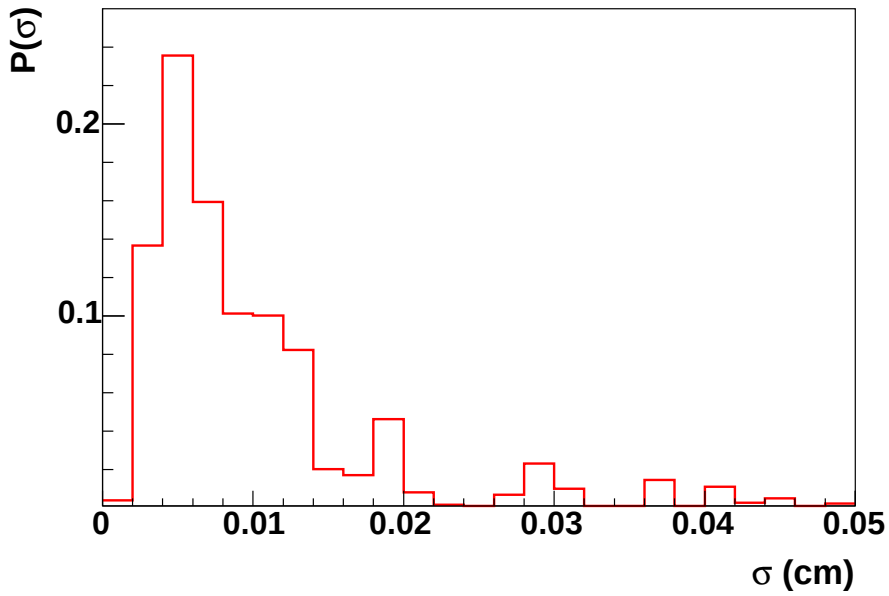

Figure 7.8: The estimated distribution of λ_M uncertainties for the signal events.

length in different intervals. Although some dependence of the scale factor on K^0_S decay length was expected, the values for the different intervals were found to be consistent with each other. The weighted average of the values was calculated to be 1.19±0.06 [79]. This measurement allows s to be fixed in this analysis, reducing the number of free parameters and hence allowing greater statistical precision in the fitted value of $c\tau(\Lambda^0_b)$. However, an additional systematic uncertainty, which is obtained by varying s by the quoted uncertainty, must then be assigned to the results. The fit was performed both with s fixed to 1.19 and with it free to check for consistency. The overall precision obtained with s fixed is superior and hence this approach was used to obtain the final result.

7.6 Lifetime Fit Results

The fit was performed using the Minuit minimisation package [80], with the minimisation performed by MIGRAD and the errors calculated using MINOS. s was fixed to 1.19 as described above. Table 7.3 shows the fitted parameter values.

Parameter	Fitted Value	Statistical Error
N_{TOT}	4471	± 296
f_{bkg}	0.160	$^{+0.068}_{-0.074}$
$c\tau(\Lambda_b^0)$	387.0 μm	$^{+35.6}_{-33.0}$ μm

Table 7.3: Results of the lifetime fit.

Figure 7.9 shows the results of this fit, where it can be seen that a reasonable fit to the data is obtained. The fit gives a χ^2 value of 5.503 for 7 degrees of freedom. The fitted value of f_{bkg} is consistent with that found in other analyses [72]. In a separate fit with s floated as a free parameter, its value converges to 1.282 ± 0.624, while the fitted value of $c\tau(\Lambda_b^0)$ is $383.0 \pm 44.5 \mu$m. The fit does not estimate s precisely, and this leads to a much larger statistical uncertainty in $c\tau(\Lambda_b^0)$. However, the fitted value is consistent with the expected value of 1.19 ± 0.06, and hence it is reasonable to fix s to this value.

7.7 Consistency Checks

Checks were performed to ensure that the results of the fitting procedure are reliable. The fit was first checked using Monte Carlo signal events that passed the selection criteria. This allows it to be checked that the fitted lifetime is consistent with the generated lifetime after the selections and fitting procedure have been performed. The lifetime fitting procedure was also checked using toy Monte Carlo. This involved performing the fit a large number of times on individually generated λ_M distributions, to check for bias in the fitting procedure and verify the accuracy of the estimated uncertainty. Also the fit was performed on different subsamples of the data to check the stability of the result.

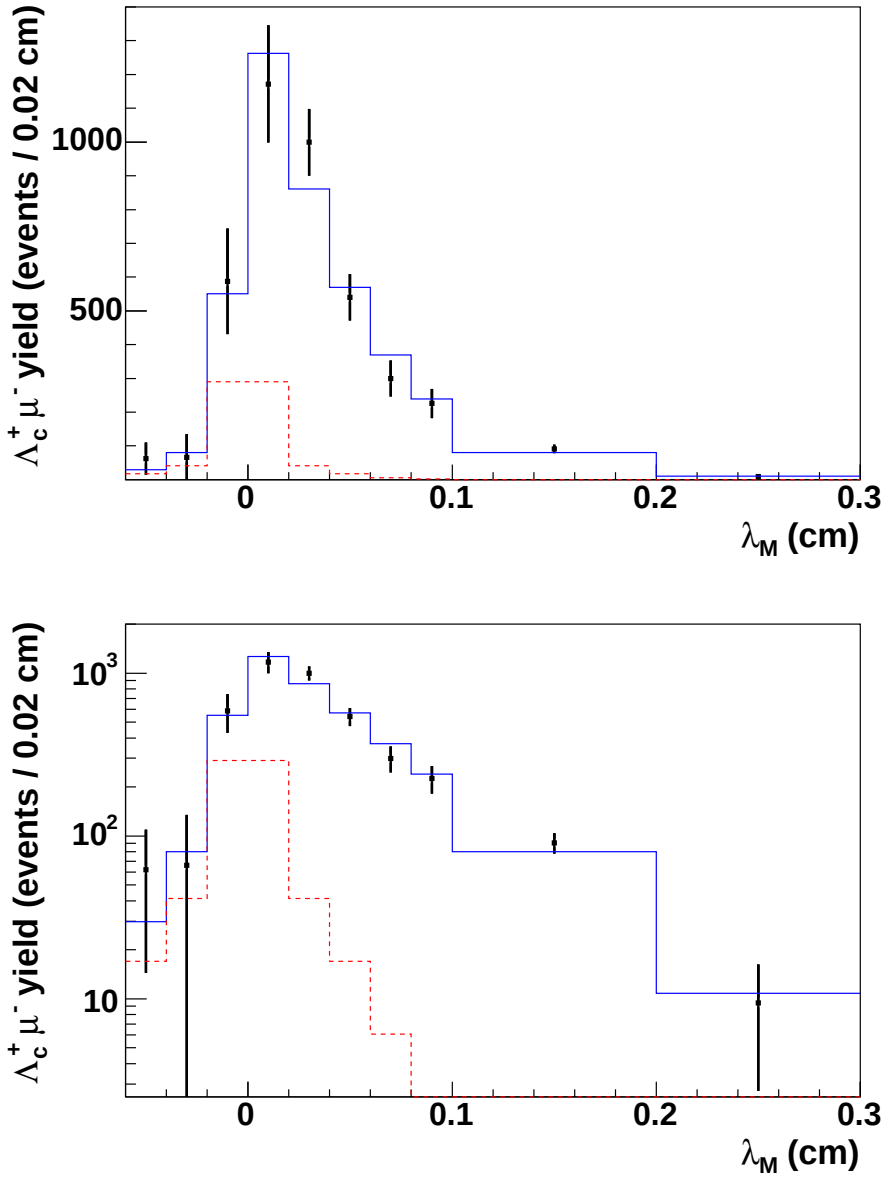

Figure 7.9: The measured $\Lambda_c^+\mu^-$ yields in the λ_M bins (points) with the result of the lifetime fit (solid line) overlaid, shown in linear and logarithmic scales. The dashed line shows the fitted contribution of peaking background.

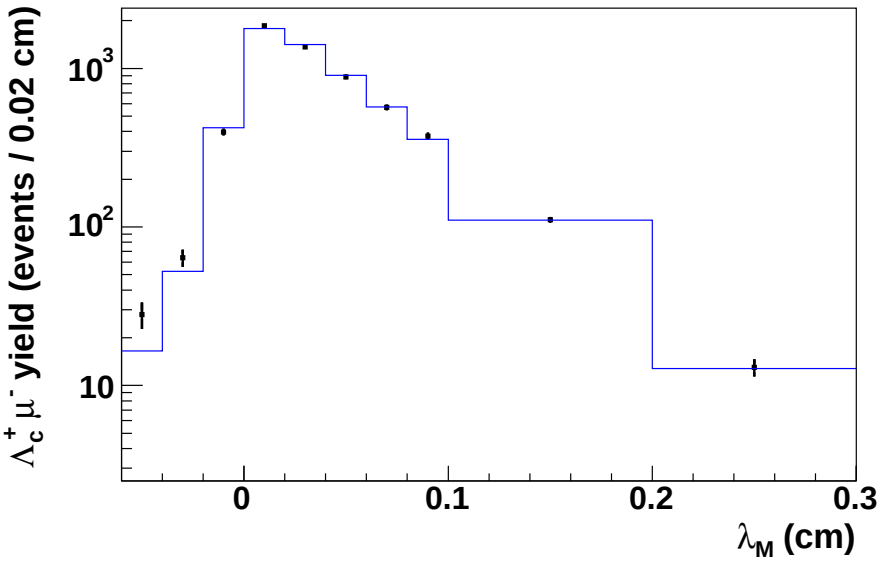

Figure 7.10: The measured $\Lambda_c^+\mu^-$ yields in the λ_M bins for 6185 simulated $\Lambda_b^0 \to \Lambda_c^+\mu^-\bar{\nu}_\mu$ events and the result of the lifetime fit to these events.

7.7.1 Fit to Monte Carlo

The lifetime fit was performed using 6185 simulated $\Lambda_b^0 \to \Lambda_c^+\mu^-\bar{\nu}_\mu$ events that were correctly reconstructed and accepted by the selection criteria. The numbers n_i were obtained by counting events in each of the λ_M bins, and the values of σ_i were estimated using $\sqrt{n_i}$. The lifetime fit was then performed using the elastic K-factor distribution, with f_{bkg} fixed to zero and s released as a free parameter. In Monte Carlo the scale factor should be consistent with unity, since the simulated tracks are propagated through the detector using the same model as used for the track fitting. The fit converged to give a value for the lifetime of $c\tau(\Lambda_b^0) = 369.3 \pm 5.5\mu$m, which is consistent with the generated value of 368μm. The fitted value of s is 1.013 ± 0.053. The results of the fit are shown in Figure 7.10. The close agreement between the generated and fitted lifetimes confirms that there are no significant biases in the full selection and fitting procedure.

7.7.2 Toy Monte Carlo Tests

Although the fit to Monte Carlo produced a result consistent with the generated lifetime, some bias may still be introduced by the fitting procedure. A bias of similar size to the statistical uncertainty would only be observed after the experiment had been repeated a large number of times. Therefore a large number of pseudo-experiments were performed, in each of which a distribution of λ_M values was generated and fitted. The distribution of the fit results would then show any bias in the fitting procedure, and the spread of the results could be checked for consistency with the statistical uncertainty given by the fit.

In each pseudo-experiment, a random number generator was used to generate a λ_M distribution containing signal events and peaking background events. Signal events were generated with a probability of 0.85, and the remaining events generated as peaking background. For the peaking background events, λ_M values were generated randomly according to the distribution in Figure 7.5. For the signal events, the lifetime was generated randomly from an exponential decay function, with the mean lifetime set to $c\tau = 385\mu$m. For each generated lifetime value, a random K-factor value was generated, using the combined K-factor distribution in Figure 7.4, and this was multiplied by the lifetime to obtain a λ value. Similarly a VPDL uncertainty was generated using the $P(\sigma)$ distribution in Figure 7.8. The deviation between λ_M and λ was simulated by multiplying the generated σ value by a random number generated using a normalised Gaussian distribution of unit width. The generated λ value was finally shifted by this deviation to obtain the simulated value of λ_M.

Since the samples contain only signal and peaking background events, a sample size of 400 events for each pseudo-experiment was used, in order to obtain fractional errors σ_i/n_i similar to those obtained in the data sample. Since some of the λ_M bins therefore contain low statistics, the uncertainties, σ_i were estimated

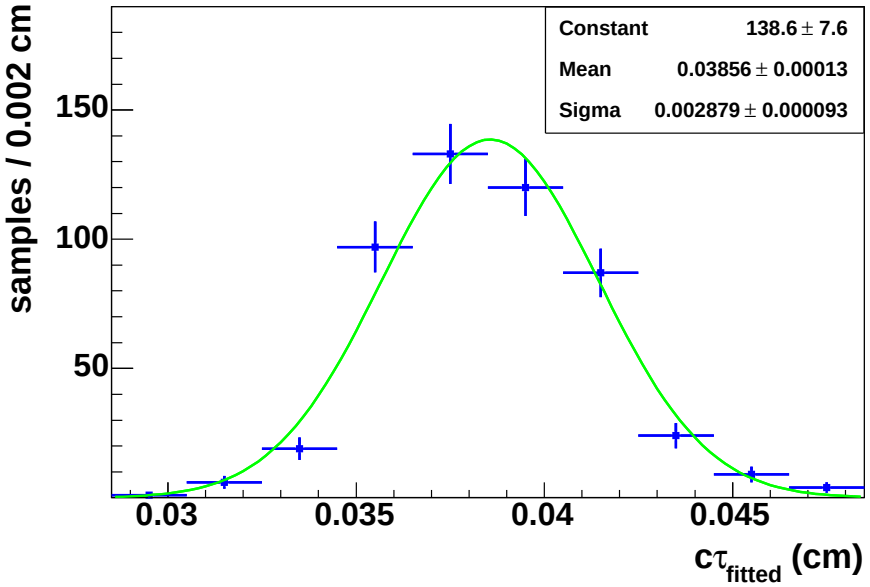

Figure 7.11: The distribution of the fitted lifetimes for the toy Monte Carlo samples, which were generated with $c\tau = 0.0385$ cm, with the results of a Gaussian fit overlaid.

by generating a sample of 5 million λ_M values, splitting the sample into the bins and using $\sqrt{n_i}$ to estimate the uncertainty. The resulting values were then scaled to give the uncertainties for a sample of 400 events.

In total 500 pseudo-experiments were performed. The distribution of the fitted lifetimes is shown in Figure 7.11. The central value of the fitted Gaussian function is seen to be consistent with the generated lifetime of $c\tau = 385\mu$m, showing that there is no statistical bias in the fit results. Figure 7.12 shows the distribution of the pull, $(c\tau_{fitted} - c\tau)/\sigma(c\tau_{fitted})$. The Gaussian distribution has a width consistent with unity, indicating that the statistical uncertainties, $\sigma(c\tau_{fitted})$, match the spread of results and hence are correctly estimated by the fit. Therefore these tests have verified the reliability of the results given by the fitting procedure.

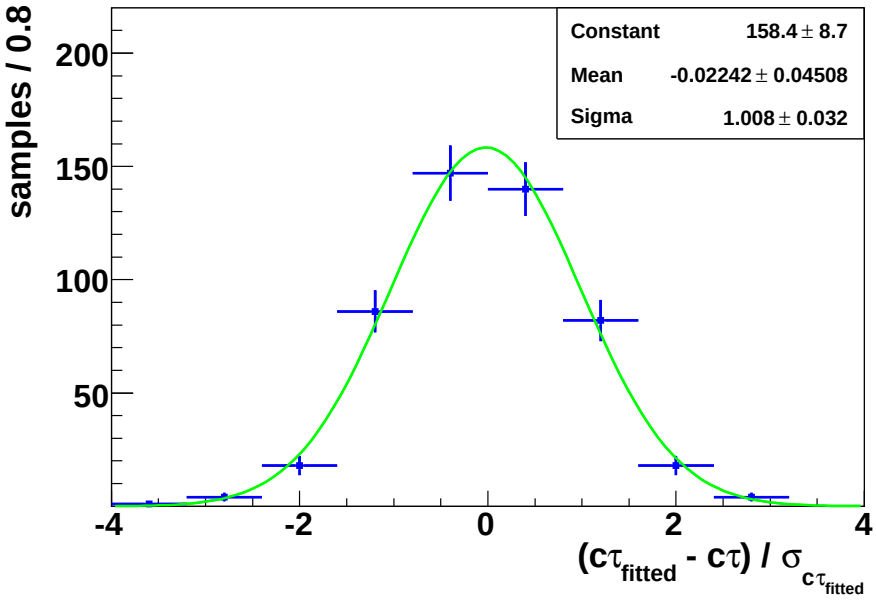

Figure 7.12: The distribution of the pull, $(c\tau_{fitted} - c\tau)/\sigma(c\tau_{fitted})$, for the fits to the toy Monte Carlo samples, with the results of a Gaussian fit overlaid.

7.7.3 Split Sample Tests

To check the stability of the lifetime measurement, some tests with the sample split into two roughly equal parts were performed. In one test the sample was split by charge, with one subsample containing Λ_b^0 candidates and the other containing $\bar{\Lambda}_b^0$ candidates. Another split was performed using subsamples of positive and negative muon pseudorapidity. Also a chronological split was used, with the run number 196000 estimated to be close to the mid point of the data sample. Finally, a split was implemented based on the measured transverse flight distance of the K_S^0, which is referred to as $d_T(K_S^0)$. This check was performed to ensure that no bias is introduced to the measurement by the long lifetime of the K_S^0, which has to be extrapolated back a few centimetres to the Λ_c^+ decay vertex. The sample was split into roughly equal parts using a split on $d_T(K_S^0)$ at 3 cm.

The lifetime measurement was repeated using each of these subsamples, with the results as shown in Table 7.4. Each subsample gives a result consistent with

Subsample	Fitted $c\tau(\Lambda_b^0)(\mu\text{m})$
Run $\leq$ 196000	422 ± 54
Run $>$ 196000	360 ± 58
$\eta(\mu) \geq 0$	384 ± 48
$\eta(\mu) < 0$	409 ± 57
Λ_b^0	383 ± 50
$\bar{\Lambda}_b^0$	380 ± 49
$d_T(K_S^0) < 3$ cm	350 ± 46
$d_T(K_S^0) \geq 3$ cm	411 ± 44

Table 7.4: Lifetime results for the split sample tests.

that obtained using the full sample, hence the fitting procedure is seen to converge to a stable result, and no bias due to the K_S^0 lifetime is evident.

7.8 Systematic Uncertainties

Systematic uncertainties in the fit results are introduced by the choices of models and parameters that are used within the fitting procedure, potential contamination of the sample by other decays and detector effects. Estimates of each of these uncertainties and their total effect on the final result are described in the following sections.

7.8.1 Mass Fitting Method

Variations in the yields of signal candidates, $n_i \pm \sigma_i$, will occur if a different function is used to model the shape of the background, or if the fitted range or bin definitions are changed. These properties were varied and the lifetime measurement repeated to estimate the variation of the results due to the changes, which is included in the systematic uncertainties.

A quartic polynomial function was used to fit the background in the histograms in Figure 7.6, since this appears to give a reasonable fit for all of the bins in the mass range shown. Due to the shape of the background in the bins at larger λ_M,

a polynomial of at least third order is required to fit the full range of 2.10 GeV/c^2- − 2.50 GeV/c^2. However, it can be seen that the background is approximately linear within the range 2.17 GeV/c^2−2.40 GeV/c^2. Therefore if the fit is restricted to this region, a lower order polynomial may be used. The bins were re-fitted using a linear background within this range, as shown in Figure 7.13. It can be seen that reasonable fits are obtained using this fitting range. Using the yields obtained in the lifetime fit, the measured lifetime is decreased by approximately 1.3μm with respect to the result in Table 7.3.

The yields are also liable to change if the same quartic polynomial is fitted,but the fitting range is changed. The measurement procedure was repeated with the first and the last bins of the mass histograms removed from the fitting range. The lifetime fit gave a result that was decreased by around 11μm with respect to the quoted result.

Variations in the width of the bins used in each of the histograms will also cause variations, as will shifting the bin centres. The histograms were produced with bins of half their original width, and also with bins of the original width, but with the edges of bins shifted downward in mass by half of the bin width. Fitting using the resulting yields gave lifetime values that were increased by 6.7μm and 20μm respectively.

The tests described above have varied the mass fitting procedure in several ways, while retaining reasonable fits to the data. These changes have been observed to cause variations in the fitted lifetime of up to 20μm. This value is given as the systematic uncertainty due to the mass fitting procedure.

7.8.2 Peaking Background

The lifetime result will vary with any change in parametrisation of the λ_M distribution of the peaking background component. The widths of the two Gaussians

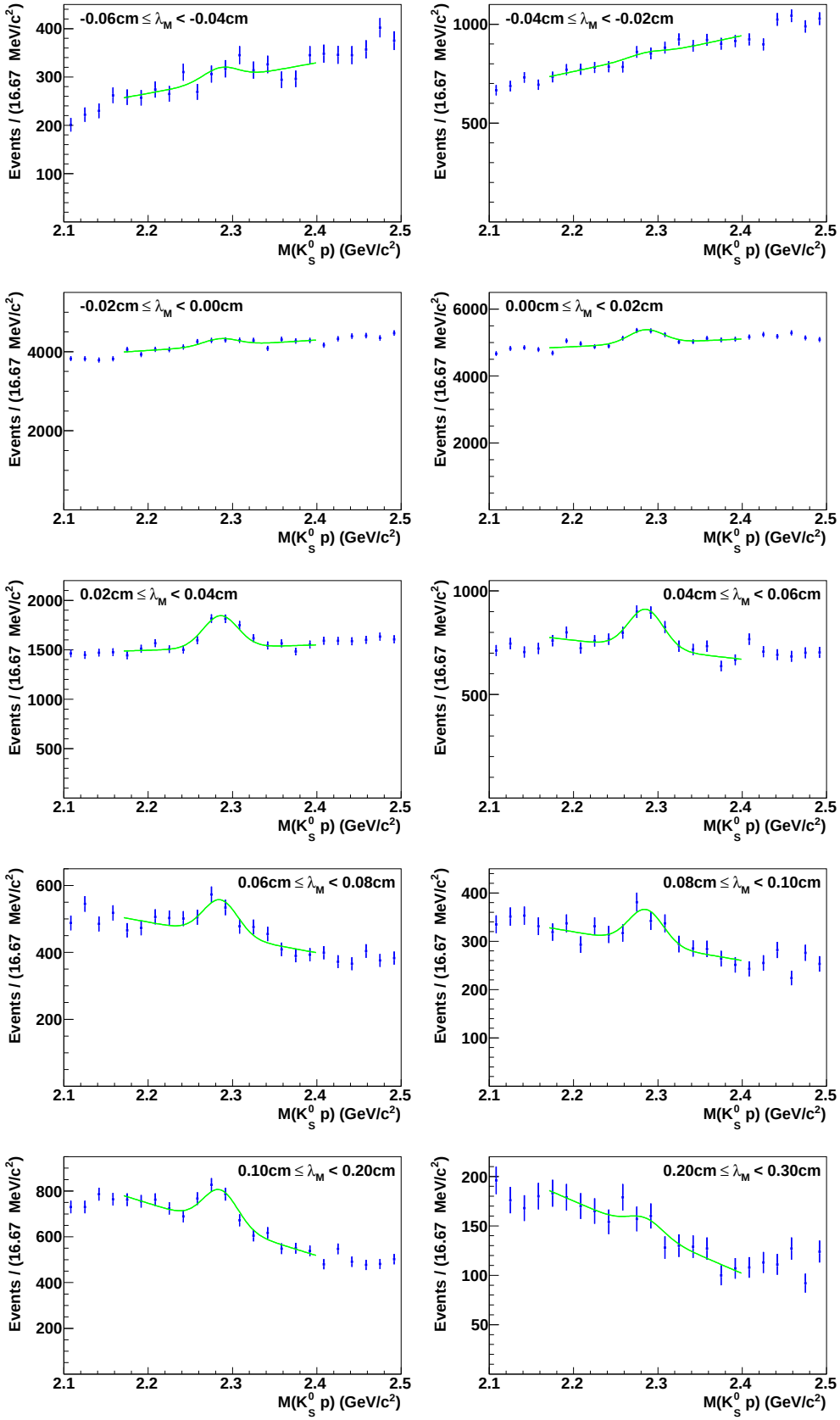

Figure 7.13: The $K^0_S p$ invariant mass distributions for the λ_M bins, fitted using a linear background function within the range 2.17 GeV/c^2– 2.40 GeV/c^2.

and the contribution of the wide Gaussian were varied by their uncertainties, separately and together in all possible combinations. The lifetime result was observed to vary by up to 3.60μm.

Another effect that is considered is due to the λ_M resolution. As mentioned previously, the resolution is poorer in data than Monte Carlo, and hence the scale factor is included in the fitting procedure. The width of the peaking background distribution is determined by the distribution of fake vertices, plus resolution effects. It is not known which proportion of the measured width is caused by resolution effects. Since the resolution is underestimated, the peaking background width may be underestimated by a factor as large as the difference between the scale factor and unity. Hence a fit was performed in which both Gaussian widths were increased by 20% to obtain the maximum possible variation and its effect on the fitted lifetime. An increase in $c\tau(\Lambda_b^0)$ of 0.97μm was observed. Since this is from a different source it is added in quadrature with the error due to the parametrization given above, to give a total systematic uncertainty due to the peaking background of 3.7μm.

7.8.3 Scale Factor

Since the scale factor is fixed to obtain the final results, it must be varied by its uncertainty to estimate the effect of this choice on the lifetime result. The study used to estimate the scale factor gave a value of 1.19 ± 0.06, while when it is released as a free parameter a value of 1.282 ± 0.624 is observed. A large variation was used, to encompass the uncertainty in the measured value and also include the fitted value within the range of variations. Changes of $\pm 20\%$ were applied to the fixed value of s, and corresponding shifts of approximately $\mp 11\mu$m were observed in the fitted lifetime. Therefore a systematic uncertainty of $\pm 11\mu$m is included for this source.

7.8.4 K-Factor Determination

To estimate the uncertainty in the result due to the uncertainty of the sample composition, the fraction of inelastic decays was varied over a wide range. The measurement shown in (7.6) gives the result $0.47^{+0.12}_{-0.10}$ for the elastic fraction, with statistical and systematic errors combined. To estimate the potential upward variation of the lifetime result, this fraction was assumed to be 0.60, and a K-factor distribution was constructed. Using this distribution in the fit gave an increase of approximately 4.8μm in $c\tau(\Lambda_b^0)$. A wider variation was used in the opposite direction to allow for the possibility of other inelastic decays in the sample, such as $\Lambda_b^0 \to \Lambda_c^+ \tau^- \bar{\nu}_\tau$. The fraction in (7.6) was assumed to be 0.30, which gave a decrease in $c\tau(\Lambda_b^0)$ of approximately 7.4μm.

Variations in the K-factor distributions for each of the decays are possible through changes in the modelling of the production and decay of the Λ_b^0 baryons. The momentum of the b quarks may be varied, and the modelling of their fragmentation and decay kinematics may be changed. A simple phase space model is used to model the Λ_b^0 decay in the samples produced for this analysis, but more sophisticated models are also available. The variation in the mean of the K-factor distribution due to using different decay models and different b-hadron momentum has been estimated in other analyses to be less than 2% [23, 81]. Therefore these effects are estimated by shifting all K-factor values by $\pm 2\%$, and observing the shift in the fitted lifetime. Shifts of approximately $\pm 7.8\mu$m were observed, and these are included with the uncertainties above.

Uncertainties may also arise due to a dependence of the K-factor distribution on p_T. Using a single K-factor distribution for all events may mean the K-factor probabilities are inaccurately modelled in some p_T regions. The K-factor distribution is plotted for some different ranges of $p_T(\mu)$ for the elastic decay in Figure 7.14, where differences in the distributions are seen. The mean of the K-

factor distribution does not change significantly with $p_T(\mu)$, however, as shown in Figure 7.15. To estimate the effect of these changes the distribution for elastic decays was also generated with a cut of $p_T(\mu) > 6$ GeV/c applied. The lifetime fit was then performed using the original elastic distribution only to model the K-factor, before repeating it using the new distribution. A shift of 1.6 μm was observed, hence this dependence has a relatively minor effect compared to the uncertainties above.

All of the shifts in the fitted lifetime described above were added in quadrature to obtain an estimate of $^{+9.3}_{-10.9}$ μm for the uncertainty due to the K-factor modelling.

7.8.5 $B \to \Lambda_c^+ \mu^- X$ Background

As shown in section 7.4.2, a small contamination of the signal due to $B \to \Lambda_c^+ \mu^- X$ decays is possible. These events will have a longer lifetime, leading to an overestimate of the Λ_b^0 lifetime. To include a fraction of B decays, an extra term should be added to equation (7.19), so the lifetime distribution for the signal events, $F_{sig}(\lambda_M)$, is replaced by

$$F_{sig}(\lambda_M) + F_B(\lambda_M) = \int dK H(K) \left[\theta(\lambda) \frac{K}{c\tau(\Lambda_b^0)} e^{-K\lambda/c\tau(\Lambda_b^0)} \otimes R(\lambda_M - \lambda, s) \right]$$
$$+ \int dK_B H(K_B) \left[\theta(\lambda) \frac{K}{\frac{m(\Lambda_b^0)}{m(B)} c\tau(B)} e^{-K_B\lambda/((m(\Lambda_b^0)/m(B))c\tau(B))} \otimes R(\lambda_M - \lambda, s) \right] \quad (7.22)$$

For the B decays the value of λ_M is not correct since the Λ_b^0 mass is used in the calculation instead of the B mass. Hence the λ_M values are overestimated, and this is corrected by multiplying the B lifetime by the ratio of masses, $m(\Lambda_b^0)/m(B)$. Although the lifetimes of B^+ and B^0 differ by around 8%, a single lifetime is assumed, since the contribution of each species is unknown.

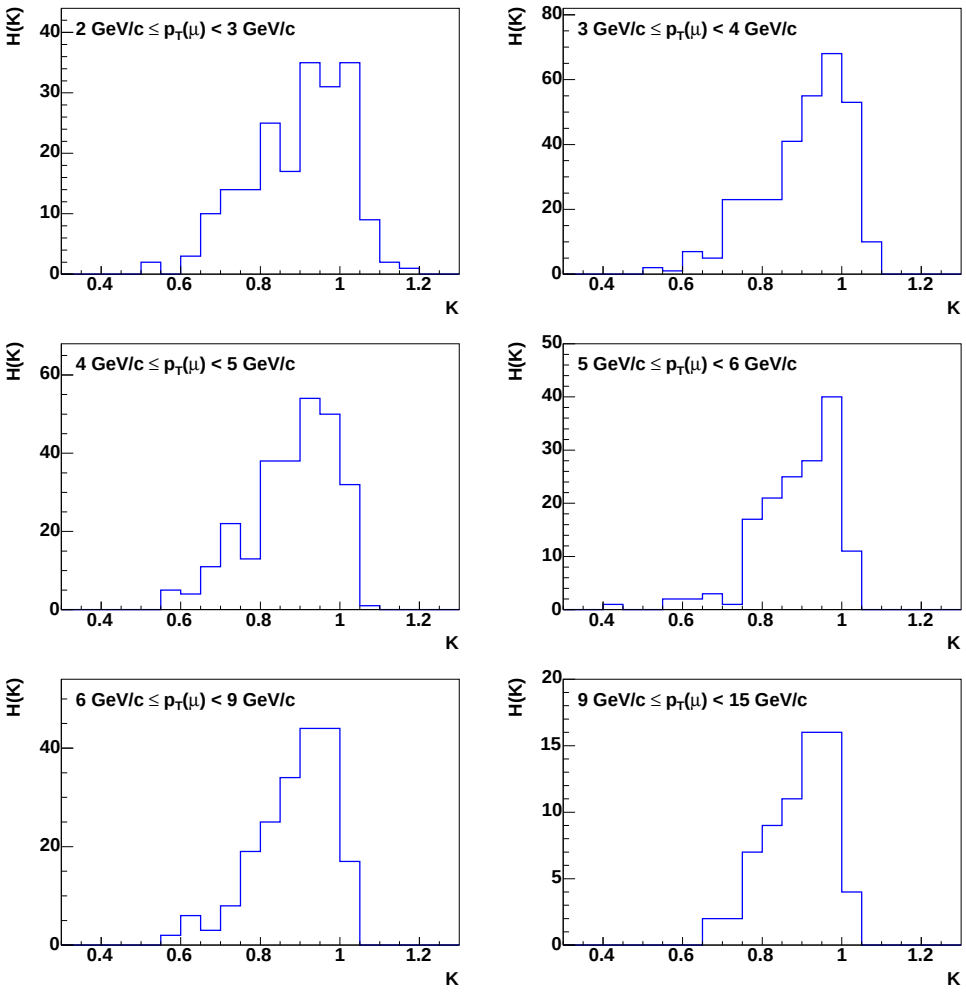

Figure 7.14: K-factor distributions for different $p_T(\mu^-)$ intervals, in $\Lambda_b^0 \to \Lambda_c^+ \mu^- \bar{\nu}_\mu$ events.

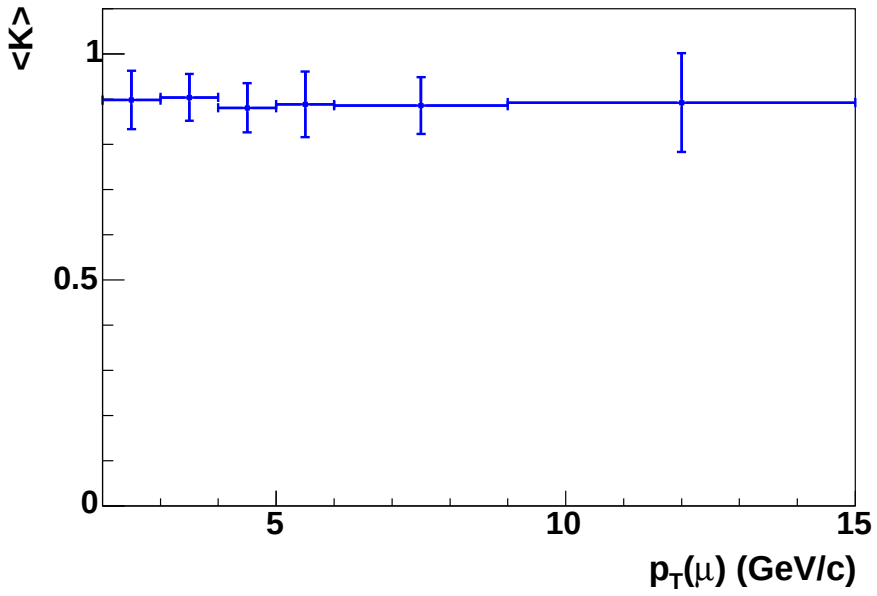

Figure 7.15: The mean value of the K-factor for each of the $p_T(\mu^-)$ intervals shown in Figure 7.14.

The systematic uncertainty due to these decays was estimated assuming a 5% contamination. The K-factor distribution for these decays was modelled using the small simulated sample of the decay $\Lambda_b^0 \to \Lambda_c^+ D_s^{(*)-}$, where the D_s^- meson decays semileptonically. As discussed in section 7.3.1, this decay was studied as a possible contribution to the signal, although it was found to be negligible. Its K-factor distribution, shown in Figure 7.16, has a lower mean value than the inelastic $\Lambda_b^0 \to \Sigma_c \pi \mu^- \bar{\nu}_\mu$ decays. Using the B^0 lifetime value for for $\tau(B)$, gave a decrease of 5.9μm in the fitted value of $c\tau(\Lambda_b^0)$, while using the larger B^+ lifetime gave a downward shift of 8.1μm. Using the larger variation, an uncertainty of $^{+0.0}_{-8.1}\mu$m is assigned to the result.

7.8.6 Detector Alignment

An additional uncertainty arises due to uncertainties in the positions of the tracking detector elements, particularly those in the SMT. If the radii of the layers are different from the expected values, then the values of λ_M will be systematically

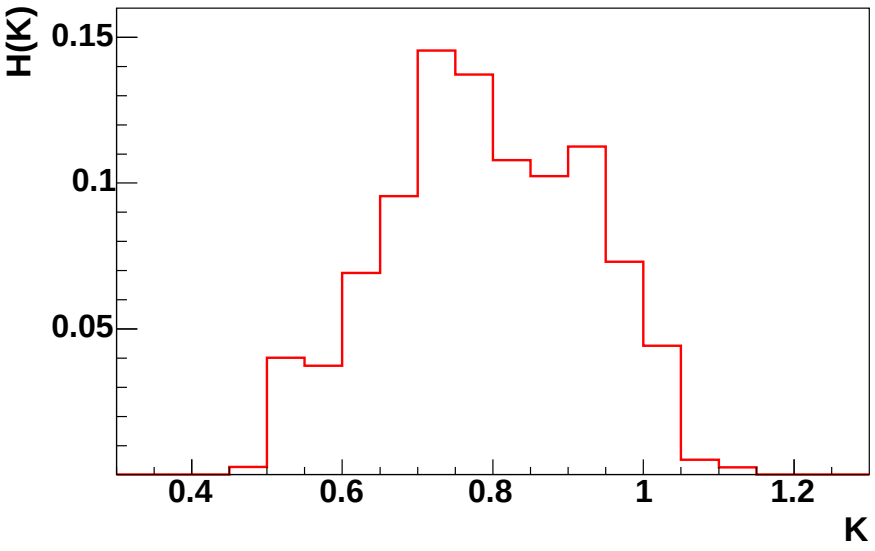

Figure 7.16: The K-factor distribution for $\Lambda_b^0 \to \Lambda_c^+ D_s^{(*)-}$ decays.

affected. This may be accounted for by repeating an analysis assuming that the SMT has a different geometry, and such studies have been performed in other analyses. In the lifetime measurement using the decay $\Lambda_b^0 \to J/\psi\Lambda$ [21], shifting the SMT sensors radially by their alignment uncertainties resulted in a systematic uncertainty of $\pm 5.4\mu$m. The corresponding uncertainty in this analysis is expected to be similar, hence the same value is quoted here.

7.8.7 Summary of Systematic Uncertainties

The systematic uncertainties are summarised in Table 7.5. The total systematic uncertainty in the value of $c\tau(\Lambda_b^0)$, obtained by adding the individual uncertainties in quadrature, is also shown.

Source	Uncertainty in $c\tau(\Lambda_b^0)(\mu\text{m})$
Mass fitting method	± 20
Peaking background	± 3.7
Scale factor	± 11
K-factor determination	$^{+9.3}_{-10.9}$
$B \to \Lambda_c^+ \mu^- X$	$^{+0.0}_{-8.1}$
Detector alignment	± 5.4
Total	$^{+25.5}_{-27.4}$

Table 7.5: Summary and combination of systematic uncertainties.

Chapter 8

Conclusions

The measurement of the Λ_b^0 lifetime has given the following result:

$$c\tau(\Lambda_b^0) = 387.0^{+35.6}_{-33.0}(\text{stat})^{+25.5}_{-27.4}(\text{syst})\ \mu\text{m}, \tag{8.1}$$

$$\tau(\Lambda_b^0) = 1.290^{+0.119}_{-0.110}(\text{stat})^{+0.085}_{-0.091}(\text{syst})\ \text{ps}. \tag{8.2}$$

Using the latest average of the B^0 lifetime [2], the value of $\tau(\Lambda_b^0)/\tau(B^0)$ implied by this result is 0.843 ± 0.096. This value is consistent with the theoretical predictions, which are still as shown in Table 2.1. This measurement has been approved by the DØ collaboration and has recently been submitted to Physical Review Letters for publication [82]. A preliminary result from this analysis, in which the result is approximately 0.01 ps lower than the latest result, was released in a conference note [83] for the 2006 DPF conference [84]. DØ has also submitted to Physical Review Letters a new measurement using the decay $\Lambda_b^0 \to J/\psi\Lambda^0$ in the full Run IIa dataset [85]. This gives a value of $\tau(\Lambda_b^0) = 1.218^{+0.130}_{-0.115}(\text{stat}) \pm 0.042(\text{syst})$ ps. The two measurements are statistically independent, and have a very small correlation of systematic uncertainties. They have been combined to give a DØ measurement of $\tau(\Lambda_b^0) = 1.251^{+0.102}_{-0.096}$ ps. Figure 8.1 shows the current set of results,

and includes the ranges of the 2006 and 2007 PDG average values. The 2006 average does not include the latest CDF result or the DØ results. The 2007 value includes the CDF result but not the DØ measurements. It can be seen that both DØ results are among the most precise, and the combination gives the most precise measurement apart from the CDF Run II measurement. The measurement presented here and the DØ combined result give stronger agreement with the 2006 world average than with the discrepant CDF measurement.

The statistical precision of this result exceeds all other measurements apart from the CDF measurement using the decay $\Lambda_b^0 \to J/\psi\Lambda^0$. Despite having backgrounds much higher than any previous result, the favourable statistical precision is achieved due to the yield of signal events, which exceeds any other measurement by several times. In terms of systematic errors, all other measurements have higher precision. However, the statistical uncertainty still dominates in this measurement, so the most simple and beneficial addition to the analysis would be larger statistics. DØ Run IIb is currently expected to last until 2009. The total integrated luminosity recorded by the detector now stands at around 2.7 fb^{-1}. At current luminosities, a further approximately 3 fb^{-1} can be expected before the end of Run II. This would give a dataset more than four times the size of that used in this measurement. Therefore an increase in the statistical precision of around 50% can be expected if this analysis is later updated with more data. Further increases in statistics may be obtained if additional Λ_c^+ decay channels are considered. Potential candidates for inclusion in the measurement are $\Lambda_c^+ \to \Lambda^0\pi^+$ and $\Lambda_c^+ \to \Lambda^0\mu^+\bar{\nu}_\mu$. The largest source of systematic uncertainty may be reduced by using unbinned fits to the mass distributions in each of the λ_M bins, although the high background may still make this the largest systematic uncertainty, due to variations when the fitting range and function are varied.

Upgrades to the detector in Run IIb may also give further improvements. The tracking has been improved by the addition of a new layer of silicon detectors close

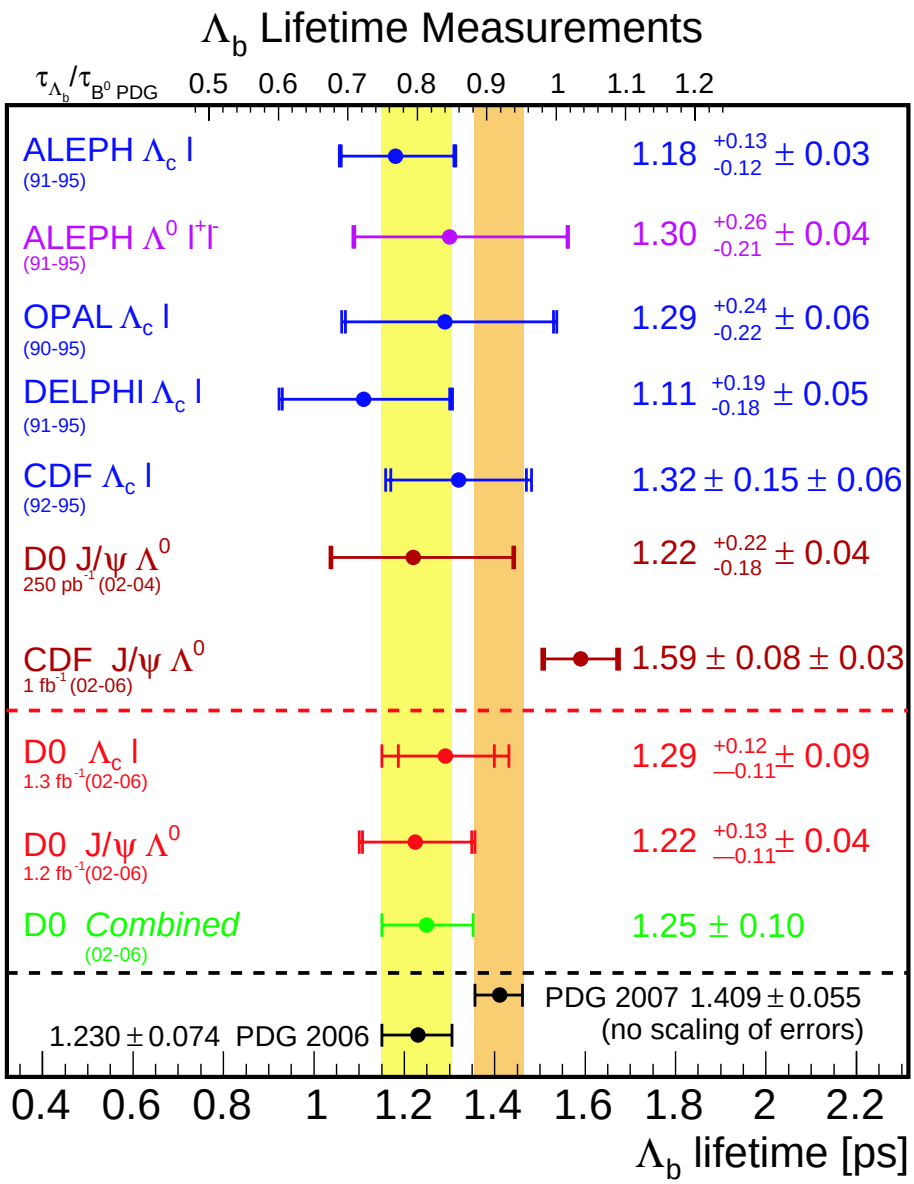

Figure 8.1: Current Λ_b^0 lifetime measurements, indicating the ranges of uncertainty of the PDG 2006 and PDG 2007 world average values. The 2006 average is calculated using the first six results, whereas the 2007 average also includes the CDF Run II measurement, but not the DØ measurements. When a discrepant analysis is included in an average, the errors are usually scaled up using a PDG procedure, but this has not been performed in this case, as indicated by the phrase 'no scaling of errors'.

to the beam pipe, known as Layer 0. This will give more precise measurements of tracks close to the primary vertex, and hence will improve the resolutions of secondary vertices and reduce the uncertainties of proper decay length measurements. Monte Carlo studies of hadronic B_s^0 decays have been performed to estimate improvements in proper time resolution with Layer 0 [86]. The resolution for these decays was improved by approximately 30%, so significant gains should also be possible for this analysis. Also, an increase in the event rate to tape has been proposed, in which 50Hz additional bandwidth will be available for b-physics events [87]. At high luminosities the triggers for b-physics are prescaled, so the acceptance rate for these events is limited. If this proposal is implemented, the number of b events written to tape would be substantially increased, and hence much larger improvements could be expected.

The further statistics and additional advances over the next few years should allow this and the other DØ measurement, which are already among the most precise, to be updated to give large improvements in the precision. Hence over the next few years, DØ measurements are likely to be very important for reduction of the experimental uncertainty on the Λ_b^0 lifetime, together with those from CDF. The era of the LHC will bring many additional precise measurements of b-hadron lifetimes, so the coming few years look promising for the experimental side of this subject.

8.1 Summary

In summary, this thesis describes a measurement of the lifetime of the Λ_b^0 baryon, which was performed using a new method developed in this analysis. The backgrounds were reduced using a likelihood ratio selection, combining several discriminating variables, but the backgrounds in the final sample were still high. The new technique is based on a binned χ^2 fit to the lifetime distribution, and allows

reliable results to be obtained in the presence of high background. The lifetime measurement itself is one of the most precise, and is consistent with the previous world average value.

Bibliography

[1] Super-Kamiokande Collaboration, Y. Fukuda et al., *Evidence for oscillation of atmospheric neutrinos*, (1998), arXiv:hep-ex/9807003v2.

[2] Particle Data Group, W.M. Yao et al., *Review of Particle Physics*, J. Phys. G 33 (2006) 1.

[3] J. Christenson et al., *Evidence for the* 2π *Decay of the* K_2^0 *Meson*, Phys. Rev. Lett. 13 (1964) 138.

[4] M. Kobayashi and T. Maskawa, *CP-Violation in the Renormalizable Theory of the Weak Interaction*, Prog. Theor. Phys. 49 (1973) 652.

[5] L. Wolfenstein, *Parametrization of the Kobayashi-Maskawa Matrix*, Phys. Rev. Lett. 51 (1983) 1945.

[6] B. Guberina et al., *D-meson lifetimes and decays*, Phys. Lett. B 89 (1979) 111.

[7] N. Bilic, B. Guberina and J. Trampetic, *Pauli interference effect in* D^+ *lifetime*, Nucl. Phys. B 248 (1984) 261.

[8] M. Neubert, *B Decays and the Heavy-Quark Expansion*, Adv.Ser.Direct.High Energy Phys. 15 (1998) 239, arXiv:hep-ph/9702375.

[9] Heavy Flavor Averaging Group, E. Barberio et al., *Averages of b-hadron Properties at the End of 2005*, (2006), arXiv:hep-ex/0603003.

[10] I.I. Bigi, *Lifetimes of Heavy-Flavour Hadrons – Whence and Whither?*, Nuovo. Cim. 109A (1996) 713, arXiv:hep-ph/9507364.

[11] F. Gabbiani, A.I. Onishchenko and A.A. Petrov, Λ_b *lifetime puzzle in heavy-quark expansion*, Phys. Rev. D 68 (2003) 114006, arXiv:hep-ph/0303235.

[12] F. Gabbiani, A.I. Onishchenko and A.A. Petrov, *Spectator effects and lifetimes of heavy hadrons*, Phys. Rev. D 70 (2004) 094031, arXiv:hep-ph/0407004v2.

[13] C. Tarantino, *Beauty Hadron Lifetimes and B-Meson CP-Violation Parameters from Lattice QCD*, Eur. Phys. J. C 33 (2004) S895, arXiv:hep-ph/0310241v2.

[14] S. Catani et al., *QCD*, 2000, arXiv:hep-ph/0005025.

[15] K. Anikeev et al., *B Physics at the Tevatron: Run II and Beyond*, 2002, arXiv:hep-ph/0201071.

[16] R.D. Field, *The Sources of b-Quarks at the Tevatron and their Correlations*, Phys. Rev. D 65 (2002) 094006, arXiv:hep-ph/0201112.

[17] DØ Collaboration, S. Abachi et al., *Inclusive μ and b-Quark Production Cross Sections in $p\bar{p}$ Collisions at $\sqrt{s} = 1.8$ TeV*, Phys. Rev. Lett. 74 (1995) 3548.

[18] CDF Collaboration, F. Abe et al., *Measurement of bottom quark production in 1.8 TeV $p\bar{p}$ collisions using muons from b-quark decays*, Phys. Rev. Lett. 71 (1993) 2396.

[19] CDF Collaboration, F. Abe et al., *Measurement of the B Meson Differential Cross Section $d\sigma/dp_T$ in $p\bar{p}$ Collisions at $\sqrt{s} = 1.8$ TeV*, Phys. Rev. Lett. 75 (1995) 1451.

[20] Heavy Flavor Averaging Group, E. Barberio et al., *Averages of b-hadron Properties at the End of 2006*, (2007), arXiv:0704.3575v1 [hep-ex].

[21] DØ Collaboration, V.M. Abazov et al., *Measurement of the Λ_b^0 lifetime in the decay $\Lambda_b^0 \to J/\psi\Lambda^0$ with the DØ Detector*, Phys. Rev. Lett. 94 (2005) 102001, arXiv:hep-ex/0410054.

[22] CDF Collaboration, A. Abulencia et al., *Measurement of the Λ_b^0 Lifetime in $\Lambda_b^0 \to J/\psi\Lambda^0$ in $p\bar{p}$ Collisions at $\sqrt{s}$ =1.96 TeV*, 2006, arXiv:hep-ex/0609021.

[23] DØ Collaboration, V.M. Abazov et al., *Measurement of the Ratio of B^+ and B^0 Meson Lifetimes*, Phys. Rev. Lett. 94 (2005) 182001, arXiv:hep-ex/0410052.

[24] ALEPH Collaboration, R. Barate et al., *Measurement of the b baryon lifetime and branching fractions in Z decays*, Eur. Phys. J. C 2 (1997) 197.

[25] DELPHI Collaboration, P. Abreu et al., *Measurement of the Lifetime of b-baryons*, Eur. Phys. J. C 10 (1999) 185.

[26] OPAL Collaboration, K. Ackerstaff et al., *Measurements of the B_s^0 and Λ_b Lifetimes*, Phys. Lett. B 426 (1998) 161, arXiv:hep-ex/9802002.

[27] CDF Collaboration, F. Abe et al., *Measurement of the Λ_b^0 lifetime using $\Lambda_b^0 \to \Lambda_c^+ l^- \overline{\nu}$*, Phys. Rev. Lett. 77 (1996) 1439.

[28] S. Burdin, *SMT dE/dx Study*, Talk given at the DØ B physics meeting, 8 May 2003.

[29] DØ Collaboration, S. Abachi et al., *Observation of the Top Quark*, Phys. Rev. Lett. 74 (1995) 2632.

[30] Fermilab Accelerator Division, *Run II Handbook*, http://www-bd.fnal.gov/runII/.

[31] http://d0server1.fnal.gov/Projects/Operations/D0RunII_DataTaking_files/image006.png.

[32] T. Yasuda, *DØ Run Report*, Talk given at December 2006 DØ Collaboration meeting.

[33] DØ Collaboration, V.M. Abazov et al., *The Upgraded DØ Detector*, Nucl. Instrum. Methods Phys. Res. A 565 (2006) 463, arXiv:physics/0507191.

[34] R. Yarema et al., *A Beginners Guide to the SVXII*, FERMILAB-TM-1892, 1994.

[35] DØ Collaboration, S. Abachi et al., *The DØ Upgrade: The Detector and Its Physics*, FERMILAB-PUB-96/357-E, 1996.

[36] J. Warchol, *CFT Status*, Talk given at CFT/CTT/preshower meeting at September 2005 DØ Collaboration meeting.

[37] DØ Collaboration, S. Abachi et al., *The DØ detector*, Nucl. Instrum. Methods Phys. Res. A 338 (1994) 185.

[38] K.M. Chan et al., *Electron and Photon Energy Resolution in the Central Calorimeter for Run 2*, DØ Note 3535, 1999.

[39] K.M. Chan et al., *Electron and Photon Energy Resolution in the End Calorimeters for Run 2*, DØ Note 3536, 2000.

[40] M. Bhattacharjee et al., *Jet Energy Resolutions*, DØ Note 2887, 1996.

[41] http://www-d0.fnal.gov/computing/algorithms/howto/howtoreco.html.

[42] T. Diehl et al., *Tracking Algorithm Recommendation Committee (TARC) Report II*, http://d0server1.fnal.gov/www/Computing/Web/Meeting/Reviews/TARC/TARC2Recom.pdf, 2003.

[43] G. Borissov, *Status of DØ Track Reconstruction*, Talk given at Talk given at DØ General Meeting, 14 February 2003.

[44] G. Borissov, *Ordering a Chaos or... Technical Details of AA Tracking*, Talk given at All DØ Meeting, 28 February 2003.

[45] G. Borisov, *Lifetime Tag of events $Z^0 \rightarrow b\bar{b}$ with the DELPHI detector. AABTAG program*, DELPHI Note 94-125 PROG 208, URL:http://pubxx.web.cern.ch/pubxx/tasks/btagging/www/, 1994.

[46] DELPHI Collaboration, J. Abdallah et al., *b-tagging in DELPHI at LEP*, Eur. Phys. J. C 32 (2004) 185, arXiv:hep-ex/0311003.

[47] A. Khanov, *HTF: histogramming method for finding tracks. The algorithm description*, DØ Note 3778, 2000.

[48] H. Greenlee, *The DØ Kalman Track Fit*, DØ Note 4303, 2004.

[49] H. Greenlee, *The DØ Interacting Propagator*, DØ Note 4293, 2003.

[50] A. Garcìa-Bellido et al., *Primary Vertex Certification in P14*, DØ Note 4320, 2004.

[51] M. Narain and F. Stichelbaut, *Vertex Reconstruction using the Impact Parameters Technique*, DØ Note 3560, 1998.

[52] O. Peters, *Muon Segment Reconstruction - Linked List Algorithm*, DØ Note 3901, 2001.

[53] F. Déliot, *The Fit Algorithm in muo_trackreco*, http://www-d0.fnal.gov/∼deliot/fitalg.ps, 2000.

[54] L. Chevalier et al., *Track Parameter Error Matrix Propagation in Matter and Magnetic Field, Error Matrices Combination*, http://www-clued0.fnal.gov/∼tuchming/myprop.ps, 2001.

[55] G. Hesketh, *Central Track Extrapolation Through the DØ Detector*, DØ Note 4079, 2003.

[56] C. Clement et al., *MuonID Certification for p14*, DØ Note 4350, 2004.

[57] http://www.thep.lu.se/∼torbjorn/Pythia.html.

[58] http://www.slac.stanford.edu/∼lange/EvtGen.

[59] http://www-clued0.fnal.gov/d0_mess.

[60] I. Bertram, *Exclusive B Hadron MC Samples*, DØ Note 4816, 2005.

[61] http://www-d0.fnal.gov/computing/MonteCarlo/simulation/d0gstar.html.

[62] http://wwwasd.web.cern.ch/wwwasd/geant.

[63] http://www-d0.fnal.gov/computing/MonteCarlo/simulation/d0sim.html.

[64] http://www-d0.fnal.gov/Run2Physics/ckm/d0_private/bgv/aa/bana.htm.

[65] G. Borissov, *New Inclusive Muon Skim*, Talk given at DØ B physics group meeting, 21 April 2005.

[66] http://www-d0.fnal.gov/Run2Physics/ckm/d0_private/btriggers/no_ip_bias/unbiased.html.

[67] S. Catani et al., *New clustering algorithm for multijet cross sections in e^+e^- annihilation*, Phys. Lett. B 269 (1991) 432.

[68] DØ Collaboration, *Reconstruction of Semileptonic Lambda-b Decays*, http://www-d0.fnal.gov/Run2Physics/WWW/results/prelim/B/B14/B14.pdf, 2004.

[69] G. Borisov, *Combined b-tagging*, Nucl. Instrum. Methods Phys. Res. A 417 (1998) 384.

[70] DØ Collaboration, *B_s Mixing studies with $B_s^0 \to D_s^- \mu^+ X$ ($D_s^- \to K^{*0} K^-$) Decay using Unbinned Fit*, http://www-d0.fnal.gov/Run2Physics/WWW/results/prelim/B/B43/B43.pdf, 2006.

[71] DELPHI Collaboration, J. Abdallah et al., *Measurement of the Λ_b^0 Decay Form Factor*, Phys. Lett. B 585 (2004) 63, arXiv:hep-ex/0403040.

[72] C. Ay et al., *$c\bar{c}$ Contribution to $B_s \to D_s(\phi\pi)\mu\nu_\mu$ Decay*, DØ Note 4639, 2006.

[73] DELPHI Collaboration, P. Abreu et al., *Production of strange B-baryons decaying into $\Xi^\mp$ - $l^\mp$ pairs at LEP*, Z. Phys. C 68 (1995) 541.

[74] ALEPH Collaboration, D. Buskulic et al., *Strange b baryon production and lifetime in Z decays*, Phys. Lett. B 384 (1996) 449.

[75] DELPHI Collaboration, J. Abdallah et al., *Production of Ξ_c^0 and Ξ_b in Z decays and lifetime measurement of Ξ_b*, Eur. Phys. J. C 44 (2005) 299, arXiv:hep-ex/0510023.

[76] W. Kwong and J.L. Rosner, *Masses of new particles containing b quarks*, Phys. Rev. D 44 (1991) 212.

[77] CLEO Collaboration, G. Bonvicini et al., *Study of Semileptonic Decays of B Mesons to Charmed Baryons*, Phys. Rev. D. 56 (1998) 6604.

[78] DØ Collaboration, *A Search for B_s Oscillations Using $B_s^0 \to D_s \mu X$ ($D_s \to K_S^0 K$) Decays*, http://www-d0.fnal.gov/Run2Physics/WWW/results/prelim/B/B46/B46.pdf, 2006.

[79] D. Krop, *Resolution Scale Factors Using K_S*, Talk given at the DØ B_s Mixing and Lifetimes meeting, 18 May 2006.

[80] F. James, *MINUIT: Minimization package*, CERN Program Library Long Writeup D506, Version 94.1.

[81] DØ Collaboration, V. Abazov et al., *Direct Limits on the B_s^0 Oscillation Frequency*, Phys. Rev. Lett. 97 (2006) 021802, arXiv:hep-ex/0603029.

[82] DØ Collaboration, V. Abazov et al., *Measurement of the Λ_b^0 lifetime using semileptonic decays*, (2007), arXiv:0706.2358v1 [hep-ex].

[83] DØ Collaboration, *Measurement of the Lambda-b Lifetime Using Semileptonic Decay*, http://www-d0.fnal.gov/Run2Physics/WWW/results/prelim/B/B47/B47.pdf, 2006.

[84] http://www.dpf2006.org.

[85] DØ Collaboration, V. Abazov et al., *Measurement of the Λ_b^0 lifetime in the exclusive decay $\Lambda_b \to J/\psi\Lambda$*, (2007), arXiv:0704.3909v1 [hep-ex].

[86] A. Kryemadhi and R. Van Kooten, *Estimated Improvement in Proper Decay Time Resolution with the Addition of Layer 0 Silicon*, DØ Note 4418, 2004.

[87] B. Abbot, V. Jain and R. van Kooten, *Estimated Gains in B Physics with Increased L3 Trigger Bandwidth*, DØ Note 4318, 2003.